# Liquid-Crystal Ordering of Photo-Switchable Molecules on a Surface

vorgelegt von
Diplom-Physiker

**Raffaele Tavarone**

geboren in Benevento, Italien

von der Fakultät II - Mathematik und Naturwissenschaften
der Technischen Universität Berlin
zur Erlangung des akademischen Grades
Doktor der Naturwissenschaften (Dr. rer. nat.)

genehmigte

Dissertation

Promotionsausschuss:

| | |
|---|---|
| Vorsitzender: | Prof. Dr. Martin Schoen |
| Erster Gutachter: | Prof. Dr. Holger Stark |
| Zweiter Gutachter: | Dr. habil. Thomas Gruhn |

Tag der wissenschaftlichen Aussprache: 27. 05. 2016

Berlin 2016

D83

# Abstract

Photo-switchable molecules are chemical compounds that undergo configurational changes upon photon absorption. In particular, azobenzene-based photo switches possess two isomeric stable states: an elongated rod-like *trans* state and a bent-shaped *cis* isomer. In this work we consider model molecules whose shape resembles that of azobenzene-based molecules and investigate their liquid-crystal assembly in two dimensions, mainly using computer simulations.

The first part of our study, motivated by the recent interest in the self-assembly of complex structures in two-dimensional systems, consists in examining the influence of different molecular geometries on the stability of several spontaneously ordered phases. We perform extensive Monte Carlo simulations of a two-dimensional bent hard-needle model in both its chiral zig-zag and its achiral bow-shape configurations and present their phase diagrams. We find evidence for a variety of stable phases: isotropic, quasi-nematic, smectic-C, anti-ferromorphic smectic-A, and modulated-nematic. This last phase consists of layers formed by supramolecular arches. They create a modulation of the molecular polarity whose period is sensitively controlled by molecular geometry. We identify transition densities using correlation functions together with appropriately defined order parameters and compare them with predictions from Onsager theory. The contribution of the molecular excluded area to Onsager theory and simple liquid crystal phase morphology is discussed. We demonstrate the isotropic–quasi-nematic transition to be consistent with a Kosterlitz-Thouless disclination unbinding scenario.

The second part of our study is motivated by the growing interest in monolayers of photo-switchable molecules. They can be used as glassy systems with light-controllable dynamics. Recent experiments have demonstrated that, in a dense monolayer of photo-switchable dye Methyl-Red molecules, the relaxation of an initial birefringence follows a power-law decay, typical for glass-like dynamics. The slow relaxation can efficiently be controlled and accelerated by illuminating the monolayer with circularly polarized light, which induces *trans*-*cis* isomerization cycles. To elucidate the microscopic mechanism, we develop a two-dimensional molecular model in which the *trans* and *cis* isomers are represented by straight and bent needles, respectively. As in the experimental system, the needles are allowed to rotate and to form overlaps but they cannot translate. The out-of-equilibrium rotational dynamics of the needles is generated using kinetic Monte Carlo simulations. We demonstrate that, in a regime of high density and low temperature, the power-law relaxation can be traced to the formation of spatio-temporal correlations in the rotational dynamics. These correlations correspond to the presence of transient domains of fast- and slowly-rotating molecules, *i.e.*, dynamic heterogeneity. We also show that the nearly isotropic *cis* isomers can prevent dynamic heterogeneities from forming in the monolayer and that the relaxation then becomes exponential.

# Zusammenfassung

Photoschaltbare Moleküle sind chemikalische Stoffe, die konfigurative Änderungen unter Photonenabsorbtion durchlaufen. Insbesondere Azobenzol-basierte Photoschalter nehmen zwei isomerische stabile Zustände an: ein länglicher, stäbchenförmiger *trans*-Zustand und ein gekrümmter *cis*-Isomer. In dieser Arbeit untersuchen wir Modellmoleküle, deren Form der Azobenzol-basierten Molekülen ähnelt und untersuchen ihre Flüssigkristallanordnungen in zwei Dimensionen, wobei wir hauptsächlich von Computersimulationen Gebrauch machen.

Der erste Teil unserer Studie, motiviert durch jüngst aufkommendes Interesse an Selbstorganisation von komplexen Strukturen in zweidimensionalen Systemen, besteht in der Untersuchung des Einflusses von unterschiedlichen, molekularen Geometrien auf die Stabilität spontan organisierter Zustände. Wir führen umfangreiche Monte-Carlo-Simulationen eines zweidimensionalen Modells gekrümmter, harter Nadeln sowohl in einer chiralen Zickzack-, als auch in einer achiralen bogenförmigen Konfiguration durch und präsentieren Phasendiagramme. Wir finden verschiedene stabile Zustände: isotrope, quasi-nematische, smektisch-C, anti-ferromorphe smektisch-A und modulierte, nematische Zustände. Letzterer besteht aus Schichten aus supramolekularen Bögen. Sie kreieren eine neue molekulare Polarität, deren Periodizität sensibel durch die molekulare Geometrie bestimmt wird. Wir identifizieren Übergangswahrscheinlichkeitsdichten mithilfe von Korrelationsfunktionen zusammen mit geeignet definierten Ordnungsparametern und vergleichen sie mit Voraussagen aus der Onsager-Theorie. Der Einfluss von molekularer "excluded area" auf die Onsager-Theorie und die Morphologie von Flüssigkristallzuständen wird diskutiert. We zeigen, dass der isotrop-quasi-nematische Phasenübergang mit einem Kosterlitz-Thouless Ablösungsszenario konsistent ist.

Der zweite Teile unserer Studie ist durch das ansteigende Interesse an Monoschichten von photoschaltbaren Molekülen motiviert. Sie können als Glassysteme mit lichtkontollierbarer Dynamik verwendet werden. Neuerliche Experimente haben aufgezeigt, dass eine initiale Doppelbrechung in einer dichten Monoschicht von photoschaltbaren methylroten Molekülen einem Potenzgesetz folgend abklingt, so wie man es aus glasähnlichen Systemen kennt. Die langsame Relaxation kann effizient durch Bestrahlen mit zirkularpolarisiertem Licht der Monoschicht gesteuert werden, was zu *trans-cis* Isomerisierungszyklen führt. Um den mikroskopischen Mechanismus zu beleuchten, entwickeln wir ein zweidimensionales, molekulares Modell, in dem die *trans* and *cis* Isomere von geraden und gekrümmten Nadeln repräsentiert werden. Wie in den Experimenten können die Nadeln rotieren und überlappen aber sich nicht verschieben. Die Nichtgleichgewichtsrotationsdynamik der Nadeln wird mit kinetischen Mont-Carlo-Simulationen generiert. Wir zeigen, dass in einem Bereich mit hoher Dichte und geringer Temperatur die Potenzgesetz-Relaxation auf Ort-Zeit-Korrelationen der Rotationsdynamik zurückgeführt werden kann. Diese Korrelationen basieren auf transienten Bereichen von schnell und langsam rotierenden Molekülen, das heißt auf dynamischer Heterogenität. Wir zeigen auch, dass die fast isotropen *cis* Isomere dynamische Heterogenitäten in der Monoschicht verhindern können und in diesem Fall die Relaxation exponentiell verläuft.

# Contents

# Chapter 1

# Introduction

The possibility to control organic and inorganic materials at the molecular, nanoscale level is crucial for a large variety of advanced applications and for a deeper understanding of matter [1–8]. In particular, interest in two-dimensional and quasi-two-dimensional structures in thin films has grown tremendously in recent years [9–11]. Molecular order can be fine tuned in thin films, which makes them suitable for myriad of technological applications [12], ranging from electronics [13] and optics [14] to biology [15].

Control over molecular ordering is achieved, on the one hand, by understanding how the characteristics of a single molecule influence the spontaneous self-assembly of large aggregate, and, on the other hand, by studying how the molecules responds to external stimuli, which can be employed to control the formation of peculiar structures. In the first case, investigating how molecular geometry determines the characteristics of aggregates is certainly crucial. A common starting point for studying this relation are hard-core models, which capture the static and dynamical properties of a wide range of phenomena, from the hard-sphere-like freezing of atomic liquids [16] to quasicrystal formation [17]. In the second case, among possible tools for molecular control, light is one of the most promising. Some of the appealing applications include: illuminating the metallic tip of a scanning force microscopy to precisely control the position of single molecules [2], using nanowires to build miniaturized photonic devices [4], and inscribing nano-sized geometrical patterns on a surface by photolithography [18].

Photochromic molecular switches, molecules that undergo configurational changes between two (or even more) isomeric states when irradiated by light [19], offer yet another appealing way to control material properties with light. Photo-switchable molecules are attracting huge interest because, when incorporated into a monolayer, illumination with light of proper wavelength results in a drastic change of the monolayer macroscopic properties. These systems belong to the class of *functional monolayers*. To give a few examples, one can control the surface wettability [20], induce deterministic nanotexturing [21], encode information [22], and tune the electrical conductivity of the monolayer [23].

In this Thesis we investigate the formation and the control of liquid-crystal order in two dimensions – both by self-assembly and by illumination with light – using model molecules whose shape resembles that of the azobenzene, an important photo-switchable compound. Indeed, the self-organized formation of liquid-crystal phases on two-dimensional surfaces is key to various nanotechnological applications [24–26], but it is also possible to employ photo-switchable molecules to reorient a nematic liquid crystal or directly control both the formation and relaxation of orientational order in a monolayer [1, 27–31].

In applications involving liquid-crystal materials, azobenzene is the most commonly used photo-switch [32]. It possesses two stable states, a *trans* and a *cis* isomer, whose

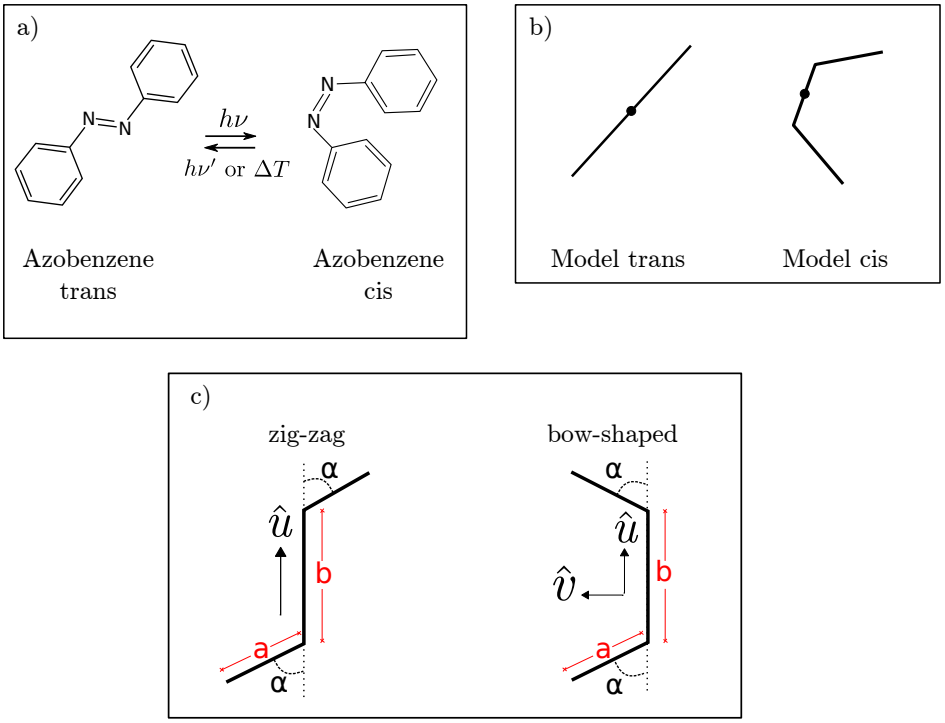


FIGURE 1.1: (a) Structures of *trans* and *cis* isomers of azobenzene. (b) The two isomers are modeled by an infinitely thin needle for the *trans* configuration and a bent version for the *cis* molecule. (c) Bent-needle model molecule in chiral zig-zag (left) and achiral bow-shaped (right) configurations.

structure is shown in Fig. 1.1(a). In the *trans* form, azobenzene is elongated and rod-like while the *cis* isomer has a bent shape. Inspired by the conformational switch of azobenzene-based molecules upon isomerization, we build a simple model for these compounds. The model allows us to study the consequences of a basic morphological change of the molecules on their equilibrium and out-of-equilibrium assembly in two dimensions. Our study mainly consists of two parts. In the first part, we consider how different molecular shapes influence the equilibrium self-assembly properties of the system. In a second part, inspired by recent experimental results of Fang *et al.* [1], we study how the isomerization process influences the out-of-equilibrium dynamics of a self-assembled monolayer.

The first part of our study is motivated by recent interest in controlling the self-assembly of two-dimensional structures. Indeed, nowadays it is possible to obtain thin aggregates with quasicrystalline [33–36], hexagonal [37], crystalline [38], and liquid-crystalline [39–41] order. Because hard-core models are known to reproduce the rich two-dimensional liquid-crystal ordering of objects with high aspect ratios such as rods [42–44], rectangles [45, 46], spherocylinders [47, 48], and ellipsoids [49, 50], we consider the two-dimensional phase behavior of a bent hard-needle model in both its chiral zig-zag and achiral bow-shaped configurations [Fig. 1.1(c)]. These two versions display significantly different mesophases, for which we map out complete phase diagrams. Zig-zag molecules are known to assemble in either a nematic or a smectic-C phase depending on the packing density $\rho$ [51, 52], and bow-shaped molecules have been found to display tetradic and nematic order [53]. Yet these studies did not clarify

the role of topological defects and of thermal fluctuations on the long-range stability of the mesophases, which are of fundamental physical interest [54–56]. The relatively coarse sampling of configuration space in previous studies left open the possibility that qualitative features of the molecular ordering have been missed. Indeed, we find that, in addition to forming quasi-nematic and smectic phases, bow-shaped molecules assume a stable modulated-nematic phase, comparable to what was previously predicted [57] and observed [58, 59] in three-dimensional systems. Our improved results are not only made possible by the use of specialized Monte Carlo simulations of large systems, but also by the definition of appropriate order parameters and correlation functions. Our analysis thence extends investigations of two-dimensional systems of hard needles [44, 60, 61], hard spherocylinders [42, 48], and spherocylinders with a polar head [62]. These improved numerical results on two-dimensional liquid crystal formation are also compared to predictions from Onsager theory [63].

In the second part of this study we consider a self-assembled monolayer of light-switchable molecules tethered to a surface. We perform kinetic Monte Carlo simulations for a molecular model, where we approximate the two isomeric states, *trans* and *cis*, by a straight and a bent needle, respectively [Fig. 1.1(b)]. The simplicity of the model allows us to study the long-time collective dynamics of a statistical ensemble consisting of 10,000 molecules [64], much more than atomistic molecular dynamics simulations can handle. As mentioned before, our work is motivated by a recent experimental study of Fang *et al.* [1] on the glasslike orientational dynamics of a self-assembled monolayer of photo-switching molecules. After aligning the molecules with light, the authors observed the decay of orientational order (or birefringence) under either thermal erasure or erasure with circularly polarized (CP) light. In both cases they find that the relaxation of birefringence follows a power law, which is typical for glasslike dynamics. Within our relatively simple model we can reproduce this feature in a system containing straight needles alone (*trans* molecules), if the density is sufficiently high and temperature is low. We demonstrate that the needles, when randomizing their orientations, develop dynamic heterogeneities in space and time [65, 66], which ultimately cause the power-law decay. The presence of *cis* molecules, which have a rather isotropic shape, can prevent the formation of such spatio-temporal variations in the local structure and the birefringence relaxation then becomes exponential. In the following, we clarify under which conditions our model reproduces the experimental observation of a power-law decay by tuning isomerization probabilities.

This Thesis is organized as follows. In Chapter 2 we introduce the liquid-crystal order, with particular focus on the liquid-crystal phases observed in the bent hard-needle model. In Chapter 3 we detail the photo-chemical properties of photo-switchable molecules and review some of their most appealing applications. Additionally, we describe the experiments presented in Ref. [1], which motivate part of our theoretical study. In Chapter 4 we introduce the numerical methods relevant for our work. In Chapter 5 we present the complete phase diagram of the bent hard-needle model. In Chapter 6 we detail our model for the self-assembled monolayer of light-switchable molecules of Ref. [1] and we discuss the related dynamics, as generated by kinetic Monte Carlo simulations. In Chapter 7 we conclude our investigation and we give an outlook of the possible future directions of our research.

Part of this work has been published in Refs. [A] and [B].

A. Tavarone, R., Charbonneau, P. & Stark, H. Phase ordering of zig-zag and bow-shaped hard needles in two dimensions. *J. Chem. Phys.* **143,** 114505 (2015).

B. Tavarone, R., Charbonneau, P. & Stark, H. Kinetic Monte Carlo simulations for birefringence relaxation of photo-switchable molecules on a surface. *J. Chem. Phys.* **144,** 104703 (2016).

# Chapter 2

# Liquid-Crystalline Order

In this Chapter we discuss the liquid-crystalline state of matter, with particular focus on the liquid-crystal phases identified in the bent hard-needle model [Fig. 1.1(c)]. In Sec. 2.1 we introduce liquid crystals and some terminology and we give a short overview of this enormous, very intriguing, and constantly growing research field. Two fundamental liquid-crystalline phases (nematic and smectic) are discussed more deeply in Sections 2.2, 2.3 and 2.4. In Section 2.5 we discuss a nematic phase with energetically stable deformations, the modulated-nematic phase, which is currently attracting interest and that is relevant for the following discussion. Because we are interested in the phases formed by bent needles on a two-dimensional surface, we also clarify how the system low dimensionality influences the long-range stability of these phases. In Sec. 2.6 we discuss the Onsager theory and its application to the phase behavior of hard-core molecular liquids. Finally, in Sec. 2.7 we summarize and detail our definition of the order parameters and associated correlation functions used to study the phase ordering of the bent-needle model.

## 2.1 Introduction to liquid crystals

Liquid crystals (LC) are materials characterized by a degree of molecular ordering, which is intermediate between the lack of structure of a liquid and the perfect ordering of a crystal [67–69]. A phase with such a partial ordering is called a mesophase, and molecules able to arrange in a mesophase are called mesogens. In a mesophase, some macroscopic properties of the material, as light propagation or viscosity, typically are anisotropic.

The investigation of liquid crystals dates back to 1888, when the Austrian botanic Friedrich Reinitzer discovered the first example of a material which belongs to the class of what are now called cholesteric liquid crystals [70]. Since then, a large variety of different mesophases have been identified. Here, we give a overview of the fundamental classifications of these materials and refer the interest reader to more detailed texts.

Classically, liquid crystals are divided into thermotropic [68, 71], lyotropic [68] and polymeric [72]. In thermotropic LCs the state of the material is fully determined by the temperature of the system, while lyotropic LCs consist of a combination of aqueous solutions and amphiphilic substances whose concentration also determines the state of the system. Above a certain concentration, amphiphile molecules form micelles. Further increase of the concentration eventually leads to formation of micellar aggregates with liquid-crystalline properties. In polymeric liquid crystals, polymers act as mesogens.

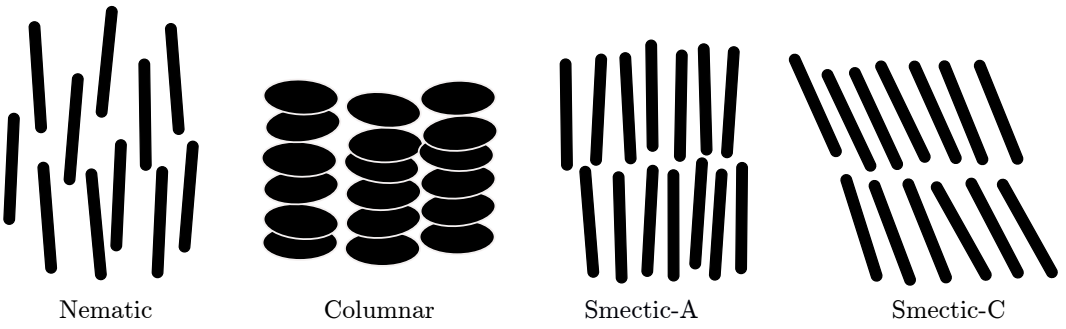


FIGURE 2.1: Schematic illustration of some fundamental mesophases formed by calamitic and discotic mesogens.

The macroscopic anisotropy of thermotropic LC is a consequence of the anisotropy of the constituent mesogens. Classically, such mesogens are classified according to their shape: rod-like molecules are called calamitic and plate-like molecules are called discotic [73]. Figure 2.1 schematically illustrates four fundamental liquid-crystal phases: calamitic mesogens arrange in nematic and smectic phases while discotic mesogens arrange in nematic and columnar phases. These phases typically occur in the sequence isotropic $\rightarrow$ nematic $\rightarrow$ smectic or isotropic $\rightarrow$ nematic $\rightarrow$ columnar with decreasing temperature.

The discotic columnar phase consists of molecules stacked in columns. The positions of the molecules along a column are liquid-like, but the columns themselves form a two-dimensional lattice of various symmetries. In the nematic phase molecules are aligned along one spatial direction (the nematic director) but their positions are randomly distributed. Nematic liquid crystals are discussed in more detail in Secs. 2.2 and 2.3. In addition to orientational order, the smectic phase possesses positional order along one spatial direction, because molecules are arranged in layers. More details on the smectic phase are given in Section 2.4. For now, we note that the smectic phase is further subdivided into smectic A, B, C, I, F, L [40, 74]. In the smectic A phase molecules are oriented along the layer normal while in the smectic C phase the orientation of the molecules is tilted with respect to the layer normal by a fixed angle. In both cases the positions of the molecules within each layer are liquid-like. By further lowering temperature, one can eventually access the hexatic smectic phases B, I, L and F in which molecular positions possess a sixfold rotational symmetry within each layer (hexatic order).

Chiral molecules (chemical groups that cannot be superimposed to their mirror images) are a special class of mesogens [75, 76]. These compounds can form special macroscopic structures, since the chirality of the mesogens induces chirality in the related mesophase. For example, a chiral nematic phase (called cholesteric for historical reasons) is a nematic phase in which the nematic director slowly rotates around one axis, thus forming an helix. Frustrated chiral phases are more complicated structures that are usually found in a narrow range of temperature. Some examples are the blue phases [77] or the twist-grain boundary phase [78, 79].

Another important class of liquid crystal formers are bent-core or banana-shaped molecules [80, 81]. The mesogenic properties of these molecules have been recognized relatively recently, starting from the pioneering work of Matsunaga and Matsuzaki [82] and Cladis and Brand [83] in 1993. It was, however, after the publication of the work by Takezoe and collaborators in 1996 [84] that the interest in the field exploded, since

banana-shaped molecules where recognized as the first achiral molecules able to arrange in ferroelectric and antiferroelectric structures.

Liquid crystals based on bent-core molecules have astonishing properties: they can form at least 7 different mesophases [80], characterized by highly non-linear optic effects [85]. Even more recently, in 2001, Dozov proposed that the achiral shape of a bent-core mesogen can induce a spontaneous local bending of the nematic director that can result in splay-bend oscillations or conical twist-bend helix [57]. The existence of the latter phase has been later demonstrated experimentally by Noel Clark and coworkers in 2013 [86]. We discuss more deeply the stable deformations of the nematic director field in Section 2.5.

Liquid-crystal materials can also be photoresponsive: anisotropic order can be induced or modified by illumination of the sample with light [27, 87, 88]. This property is achieved by incorporating in the LC material light-absorbing molecules, which are able to switch between different stable configurations upon irradiation. The light-absorbing molecules can be either dispersed in a host liquid-crystal matrix or they can be directly used as mesogens. In both cases, the modification induced by light at the microscopic level are reflected in a sensitive change in the macroscopic properties of the material. Photoresponsive liquid crystal are not simply thermotropic since illumination does not necessarily induce significant heating. Because of the importance that photoresponsive LC have for this work, we discuss the subject more extensively in Chap. 3.

Before concluding this short overview, we note that one of the most promising research direction in the liquid-crystal field is nowadays represented by the possibility to obtain non-equilibrium mesophases using active matter [89]. The individual components of an active system dissipate energy and move in a collective fashion. When these individual components are elongated objects they can form liquid-crystalline states with surprising out-of-equilibrium dynamical and rheological properties [90, 91].

Finally, we refer the interested reader to Ref. [68] and Ref. [72] for a discussion on lyotropic and polymeric liquid crystal, respectively.

## 2.2 Nematic order

In a nematic phase mesogens tend to be aligned along one common axis, identified by a unit vector $\mathbf{n}$ called the director. This phase is characterized by the following properties [67]:

1) The correlation between the mesogens positions is only short-ranged, resembling that of a liquid.

2) Two states characterized by $\mathbf{n}$ and $-\mathbf{n}$ are by all means indistinguishable.

3) A nematic liquid crystal has full cylindrical symmetry around $\mathbf{n}$.

From the molecular point of view, a nematic phase can be described by an orientational distribution function peaked around an arbitrary direction (all the directions of $\mathbf{n}$ are equivalent). Let us consider a rod as a simple mesogen able to form a nematic phase. The orientation of the rod is defined by a vector $\mathbf{u}$. In three dimensions $\mathbf{u}$ can be expressed in terms of the polar angles $(\theta, \phi)$ as

$$u_x = \sin\theta\cos\phi\,,\; u_y = \sin\theta\sin\phi\,,\; u_z = \cos\theta\,. \tag{2.1}$$

The orientation of the system is therefore characterized by a distribution function $f(\theta, \phi)$, where $f(\theta, \phi)d\Omega$ gives the probability to find a rod in the solid angle $d\Omega = \sin\theta\, d\theta\, d\phi$

around $(\theta, \phi)$. If we assume that the nematic director is oriented along $z$, because of property 3, $f(\theta, \phi)$ is independent of $\phi$ (cylindrical symmetry). We can now look for a quantity which characterizes the degree of alignment in the system. Because there is no polar order in the system, the quantity

$$\langle \cos\theta \rangle = \int f(\theta) \cos\theta \, d\theta \,, \tag{2.2}$$

vanishes ($\langle \cos\theta \rangle = 0$) and one has to look at higher-order quantities. One possibility is to use

$$S = \frac{1}{2}\langle 3\cos^2\theta - 1 \rangle = \frac{1}{2}\int f(\theta)[3\cos^2\theta - 1]\, d\theta \,, \tag{2.3}$$

which gives $S = 1$ if $f(\theta)$ is peaked around $\theta = 0$ or $\theta = \pi$, and $S = 0$ if $f(\theta)$ is uniform ($\langle \cos^2\theta \rangle = 1/3$). Therefore, $S$ is a good measure of the degree of alignment of a nematic liquid crystal and it is called the Maier-Saupe order parameter.

In other words, because of the symmetry properties of the nematic phase, it is not possible to define a vector order parameter, and a nematic LC needs to be described by tensorial quantities. Indeed, if we consider a system of $N$ molecules, in which the orientation of a single molecules is described by a unit vector $\mathbf{u}^{(i)}$, a natural generalization of Eq. (2.3) is

$$Q_{\alpha\beta} = \frac{1}{2N}\langle \sum_{i=1}^{N} \left( 3\, u_\alpha^{(i)} u_\beta^{(i)} - \delta_{\alpha\beta} \right) \rangle \,, \tag{2.4}$$

where $\delta$ is the Kronecker symbol and $\alpha, \beta = x, y, z$. The tensor $\mathbf{Q}$ is called the tensor order parameter, it is symmetric and of zero trace. To demonstrate the properties of $\mathbf{Q}$, it is convenient to express $\mathbf{u}^{(i)}$ in spherical coordinates as in Eq. (2.1). In this way

$$Q_{\alpha\beta} = \frac{1}{2}\int_0^{2\pi} d\phi \int_0^{\pi} \sin\theta \, d\theta \, f(\theta, \phi) \left( 3\, u_\alpha u_\beta - \delta_{\alpha\beta} \right) . \tag{2.5}$$

In the isotropic phase the distribution function is independent of the molecular orientation. The normalization condition

$$\int_0^{2\pi} d\phi \int_0^{\pi} \sin\theta d\theta \, f(\theta, \phi) = 1 \,, \tag{2.6}$$

gives $f_{\text{iso}} = 1/4\pi$. Using $f_{\text{iso}}$ together with Eqs. (2.1) in Eq. (2.5) gives, for example,

$$Q_{xx} = \frac{1}{2} f_{\text{iso}} \int_0^{2\pi} d\phi \int_0^{\pi} \sin\theta d\theta \, (3\cos^2\phi \sin^2\theta - 1) = 0 \,. \tag{2.7}$$

Similar calculations for the other components show that, in the isotropic phase, $\mathbf{Q} = 0$.

In a perfectly aligned uniaxial nematic phase, assuming that molecules are oriented along the $z$ axis, it is sufficient to evaluate $Q_{zz} = (3u_z u_z - 1)/2 = 1$ and the other components are immediatly obtained considering that $\mathbf{Q}$ is symmetric and of zero trace:

$$\mathbf{Q} = \begin{pmatrix} -1/2 & 0 & 0 \\ 0 & -1/2 & 0 \\ 0 & 0 & 1 \end{pmatrix} . \tag{2.8}$$

The tensor order parameter is a good quantity to characterize nematic order. In many situations however, it is convenient to use some simple quantity, like $S$ in Eq. (2.3), to quantify the degree of alignment more directly. This is usually done by writing the tensor order parameter in a coordinate system where it is diagonal. Because the tensor order parameter is a $3 \times 3$ symmetric matrix, the diagonalization gives three real eigenvalues. The eigenvector corresponding to the eigenvalue with the largest absolute value indicates the direction along which molecules are more strongly aligned, and it is therefore the natural candidate for the nematic director $\mathbf{n}$. The largest eigenvalue quantifies the degree of alignment along the correspondent direction and it is therefore identified with $S$. For an uniaxial nematic phase the tensor order parameter can thus be written as

$$Q_{\alpha\beta} = \frac{S}{2}(3n_\alpha n_\beta - \delta_{\alpha\beta})\,. \tag{2.9}$$

Having identified a proper order parameter for the nematic phase, we can now discuss some of the approaches used to study the transition between an isotropic phase (uniform distribution of molecular alignment) and a nematic phase with a well-defined average orientation. This is the isotropic–nematic transition and it is one of the most extensively studied phase transition in the LC literature. Therefore, in the following we just summarize the basic features of the main approaches to this problem, with a special attention to those having relevance in the following Chapters of this thesis.

### 2.2.1 Onsager theory: heuristic approach

The simplest microscopic picture of a nematic phase is given by the Onsager theory. In his seminal work [92], Onsager assumed that the nematic mesogens are rods of length $L$ and diameter $D$. The rods feel an hard-core repulsion, *i.e.*, they cannot interpenetrate each other. In theory, a nematic liquid crystal is thus treated as an extension of a fluid of hard spheres [93], with the only exception that the molecules have now an highly anisotropic shape. The shape anisotropy is responsible for the formation of a nematic phase at high density. The theory, based on an expansion of the free energy in powers of the orientational density, is detailed in Sec. 2.6. In this section we provide an heuristic argument, which demonstrates the isotropic-nematic transition in a system of elongated hard molecules.

A central concept in the Onsager theory is the excluded volume. Given two rods with orientation defined, respectively, by $\mathbf{u}^{(1)}$ and $\mathbf{u}^{(2)}$, the excluded volume, $V_{\rm excl}(\mathbf{u}^{(1)}, \mathbf{u}^{(2)})$, is the portion of space not accessible to rod 2 because it will result in an overlap with rod 1 (see Fig. 2.2). For very long rods ($L \gg D$) one shows that

$$V_{\rm excl}(\mathbf{u}^{(1)}, \mathbf{u}^{(2)}) \sim 2L^2 D \sin\gamma\,, \tag{2.10}$$

where $\gamma$ is the angle between $\mathbf{u}^{(1)}$ and $\mathbf{u}^{(2)}$.

At constant temperature and density, the internal energy of hard-core systems is fixed. Hence, according to the second law of thermodynamics, if the system orders it can only do so by increasing its entropy. This counter-intuitive picture (an ordered system with higher entropy than a disordered one) is indeed the correct explanation for the isotropic-nematic transition in the Onsager theory: at sufficiently high density, the loss in orientational entropy is compensated by an increase in translational entropy.

This statement can be made quantitative by using the Boltzmann entropy of an isolated system of $N$ molecules in a volume $V$ in order to evaluate the difference in

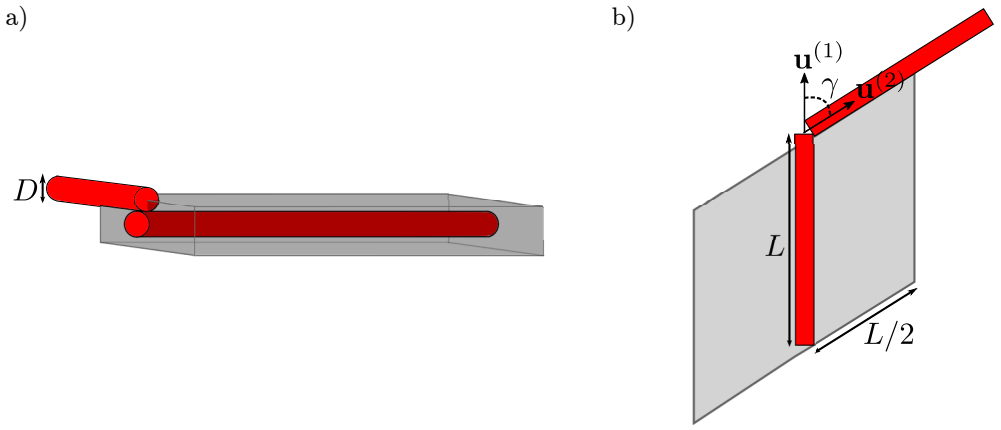


FIGURE 2.2: The light-grey region represents the excluded area for two rods with orientation defined by $\mathbf{u}^{(1)}$ and $\mathbf{u}^{(2)}$. The angle between the two orientations is $\gamma$. In (a) we give a side view of the excluded area while in (b) the view is from the top.

the entropy in the isotropic and the nematic phase. The translational entropy can be estimated by considering the amount of free volume available. Using Eq. (2.10) and assuming that the excluded volume in the nematic phase is approximately zero,

$$\Delta S_{\text{translation}} = S_{\text{nematic}} - S_{\text{isotropic}} = k_{\text{B}} \ln\left(\frac{V}{V - NV_{\text{exl}}}\right) \approx k_{\text{B}} \rho L^2 D \,, \tag{2.11}$$

where $\rho = N/V$ is the number density. The orientational entropy is proportional to the number of accessible orientational states $\Omega$,

$$\Delta S_{\text{orientation}} = S_{\text{nematic}} - S_{\text{isotropic}} = k_{\text{B}} \ln\left(\frac{\Omega_{\text{nematic}}}{\Omega_{\text{isotropic}}}\right) \propto -k_{\text{B}} \,, \tag{2.12}$$

where the proportionality is up to a positive constant because $\Omega_{\text{nematic}} < \Omega_{\text{isotropic}}$. At the isotropic-nematic transition the two contribution are balanced

$$\Delta S_{\text{translation}} + \Delta S_{\text{orientation}} = 0 \,, \tag{2.13}$$

which gives a good estimate for the transition density $\rho_{\text{I-N}} \propto 1/L^2 D$, *i.e.*, longer rods form a nematic phase at lower density. The result can also be expressed in terms of rod volume concentration $\Phi$:

$$\Phi_{\text{I-N}} = \frac{V_{\text{rods}}}{V_{\text{I-N}}} \propto \frac{NLD^2}{NL^2D} = \frac{D}{L} \,. \tag{2.14}$$

A more precise calculation shows that, at the transition point, the nematic and the isotropic phase coexists, with $\Phi_{\text{N}} = 4.5D/L$ for the nematic phase and $\Phi_{\text{I}} = 3.3D/L$ in the isotropic phase. In the nematic phase the order parameter is $S \approx 0.8$ [67]. Onsager theory predicts therefore a first order transition between a disordered and an highly ordered phase separated by a sudden jump in density. Also, due to the hard-core interaction potential the transition point is independent of temperature.

In order to overcome these limitations, a mean-field theory has been proposed in 1958 by Maier and Saupe [94]. In their theory two mesogens with orientations respectively defined by the unit vectors $\mathbf{u}$ and $\mathbf{u}'$ interact via a pair potential which favors molecular

alignment, $V(\mathbf{u},\mathbf{u}') \propto P_2(\mathbf{u}\cdot\mathbf{u}')$ where $P_2$ is the second Legendre polynomial. The Maier-Saupe theory predicts a first-order isotropic–nematic phase transition with decreasing temperature [67].

### 2.2.2 Frank-Oseen-Zocher elastic theory

Once a proper order parameter has been defined, as we did in Eq. (2.4), Landau theory allows us to express the free energy density of the system as an analytic function of it. In the Landau-de Gennes approach, the free energy density of a nematic liquid crystal is expanded in power series of the tensor order parameter $\mathbf{Q}$ defined in Eq. (2.4). The expansion must contain all the possible combinations of $\mathbf{Q}$ that are invariant under rigid rotation of the axes. Up to the fourth order (summation over repeated indices is implied) the free energy density reads

$$\mathcal{F} = \mathcal{F}_i + \frac{1}{2}AQ_{\alpha\beta}Q_{\alpha\beta} - \frac{1}{3}BQ_{\alpha\beta}Q_{\beta\gamma}Q_{\gamma\alpha} + \frac{1}{4}CQ_{\alpha\beta}Q_{\alpha\beta}Q_{\gamma\delta}Q_{\gamma\delta}\,, \tag{2.15}$$

where $\mathcal{F}_i$ is the free energy density of the isotropic phase and $A$, $B$ and $C$ are temperature-dependent coefficients. The third-order term in Eq. (2.15) is absent in the Landau free energy of magnetic systems due to their vectorial symmetry, but it is present in Eq. (2.15) due to the equivalence between $\mathbf{n}$ and $-\mathbf{n}$. It is because of this term that the isotropic–nematic phase transition is first order [67].

A free energy density of the type of Eq. (2.15) implies that the tensor order parameter is spatially uniform. In reality, a nematic liquid crystal shows spatial variation of the orientational order. Hence, the next natural step in the development of a continuous theory consists in introducing an explicit spatial dependence of the tensor order parameter.

Because we want the theory to be continuous, we shall assume that the molecular orientation varies slowly relative to the molecular length. Under this assumption, a spatially dependent tensor order parameter can be properly defined by making the nematic director dependent on its spatial coordinates, *i.e.*, $\mathbf{n} \to \mathbf{n}(\mathbf{r})$ [see Eq. (2.9)]. With this definition we can now write the free energy density, $\mathcal{F}_\mathrm{d}$, associated with the distortion of the nematic director. $\mathcal{F}_\mathrm{d}$ has to be a function of all the combinations of the spatial derivatives of $\mathbf{n}(\mathbf{r})$ that are compatible with the symmetry of the nematic phase. The usual approach is to retain only first and second order terms in the derivatives of the local nematic director, $\nabla_\alpha n_\beta(\mathbf{r})$, and to impose uniaxial symmetry [95, 96].

The evaluation of all these terms is a rather tedious operation, and we refer the reader to Ref. [95] for a complete discussion. After some algebra the distortion free energy density of an uniaxial, centrosymmetric (non-cholesteric) nematic liquid crystal in the bulk is conveniently written as

$$\mathcal{F}_\mathrm{d} = \frac{1}{2}K_1(\nabla\cdot\mathbf{n})^2 + \frac{1}{2}K_2(\mathbf{n}\cdot(\nabla\times\mathbf{n}))^2 + \frac{1}{2}K_3(\mathbf{n}\times(\nabla\times\mathbf{n}))^2 \tag{2.16}$$

where $K_1$, $K_2$ and $K_3$ are three positive constant with the dimension of energy/length.

Equation (2.16) is the Frank-Oseen-Zocher (FOZ) elastic free energy density for a nematic liquid crystal in the bulk [96–98]. It tells us that the ground state of a nematic material is the spatially uniform orientation, and each distortion costs elastic energy. The terms in the FOZ free energy density have a well defined physical interpretation: they evaluate, respectively, splay, twist and bend deformations. These elastic deformations are

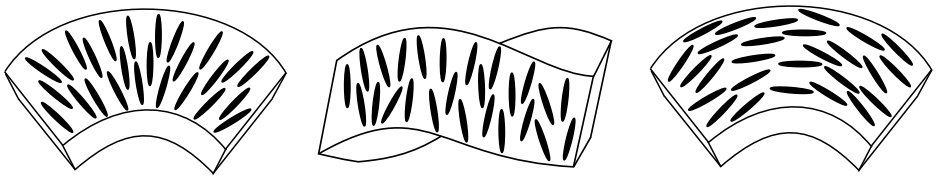


FIGURE 2.3: Schematic illustration of the splay, twist and bend elastic deformation of a nematic liquid crystal. Each term in Equation (2.16) is associated with one of these deformations.

illustrated in Fig. 2.3. Calamitic liquid crystals usually have $K_3 \geq K_1 > K_2$ (bending costs much more energy than twisting) while discotic liquid crystals have $K_2 \geq K_1 > K_3$ [99].

A summary of the theoretical approaches to the calculation of the elastic constants of uniaxial nematic LC can be found in Ref. [100]. They can also be determined in computer experiments using the orientational fluctuation of the tensor order parameter as a function of a wave vector [101–103].

Due to the complexity of Eq. (2.16), it is very common to treat the FOZ free energy using the so called one-constant approximation, which consists in setting $K_1 = K_2 = K_3 = K$. In this way all the effects of the anisotropic elasticity are neglected, but it is easier to understand some qualitative features of the distorted nematic phase since Eq. (2.16) reduces to

$$\mathcal{F}_d = \frac{K}{2}[(\nabla \cdot \mathbf{n})^2 + (\nabla \times \mathbf{n})^2]\,, \tag{2.17}$$

which is much easier to treat both numerically and analytically. We use the one-constant approximation in Sec. 2.3.1 to discuss the stability of nematic order in two-dimensional systems.

### 2.2.3 Optical birefringence

Because of their complex anisotropic structures, liquid crystals possess astonishing optical properties [104]. Among those, birefringence is a fundamental aspects of the liquid-crystalline structures. Additionally, the birefringence of a nematic monolayer is a central concept in Chapters 3 and 6. In this section we define the birefringence and shortly discuss its connection to the microscopic structure of nematic liquid crystals. We warn the reader that only in this section the symbol $n_i$ denotes refractive indexes and not the spatial components of the nematic director.

The electric permittivity, $\boldsymbol{\epsilon}$, of an anisotropic medium is a second-rank tensor [105]. Since $\boldsymbol{\epsilon}$ is symmetric, it is possible to identify a coordinate system, in which all the off-diagonal element of $\boldsymbol{\epsilon}$ vanish. This coordinate system defines the principal axes of the anisotropic medium. The permeability of non-ferroelectric material at optical frequencies is close to unity. Hence, the permittivities along the principal axes correspond to a set of refractive indexes,

$$n_i = \left(\frac{\epsilon_i}{\epsilon_0}\right)^{1/2}, \tag{2.18}$$

where $\epsilon_0$ is the vacuum permittivity. Consider a linearly polarized wave propagating along one of the principal axes of the material with the polarization direction having components along the two remaining axes. The two components will travel at different

velocities, *e.g.*, $c_0/n_1$ and $c_0/n_2$. When recombined at the exit of the material, they will thus experience a phase shift $\Delta\phi \propto (n_2 - n_1)$. The resulting wave will be elliptically polarized and the material act as a wave retarder.

If two of the principal refractive indexes are equal, the material is called uniaxial, while if the $n_i$ are all different the material is called biaxial. For an uniaxial material, the ordinary and extraordinary refractive indexes are defined, respectively, by $n_o = n_1 = n_2$ and $n_e = n_3$. The difference $\Delta n = n_e - n_o$ is called *birefringence*. Uniaxial materials also possess a special axis called the optic axis [105]. A ray propagating along the optic axis shows no sign of birefringence. In uniaxial nematic liquid crystals the nematic director coincides with the optic axis.

In isotropic systems, the connection between the macroscopic and microscopic properties of a material is described by the Lorentz-Lorentz equation, which gives the refractive index $n$ as a function of the molecular polarizability $\alpha$,

$$\frac{n^2 - 1}{n^2 + 2} = \frac{N}{3\epsilon_0}\alpha\,, \tag{2.19}$$

where $N$ is the number of molecules per unit volume.

For anisotropic molecules, the polarizability $\boldsymbol{\alpha}$ is a tensor. Let us assume that, in the reference frame defined by the main molecular axes, the tensor is diagonal, *i.e.*,

$$\boldsymbol{\alpha} = \begin{pmatrix} \alpha_o & 0 & 0 \\ 0 & \alpha_o & 0 \\ 0 & 0 & \alpha_e \end{pmatrix}\,, \tag{2.20}$$

where we also assumed that $\boldsymbol{\alpha}$ has cylindrical symmetry around one molecular axis. The Lorentz-Lorentz relation of Eq. (2.19) is thus generalized as

$$\frac{n_i^2 - 1}{n^2 + 2} = \frac{N\langle\alpha_{ii}\rangle}{3\epsilon_0}\,, \tag{2.21}$$

where $\langle\alpha_{ii}\rangle$ is the mean molecular polarizability along the direction of a principal axis and $n = (n_e + 2n_o)/3$ [104].

It is important to note that the average values of $\boldsymbol{\alpha}$, expressed in a reference frame coincident with the principal axes, depend on the degree of nematic order in the system [104]. Also, due to the equivalence of the nematic director and the optic axis one has $n_o = n_\perp$ and $n_e = n_\parallel$, where the subscript "$\parallel$" ("$\perp$") denotes components parallel (perpendicular) to the nematic director. It can thus be shown (see for instance Ref. [106]) that Eq. (2.21) leads to

$$S\frac{\Delta\alpha}{\alpha} = \frac{n_\parallel^2 - n_\perp^2}{n_\perp^2 n_\parallel^2 + n_\perp^2 - 2} = \frac{(n_\parallel - n_\perp)(n_\parallel + n_\perp)}{n_\perp^2 n_\parallel^2 + n_\perp^2 - 2}\,, \tag{2.22}$$

where $\Delta\alpha = \alpha_e - \alpha_o$ is the polarizability anisotropy and $\alpha = (\alpha_e + 2\alpha_o)/3$ is the mean molecular polarizability.

When the birefringence $\Delta n = n_\parallel - n_\perp$ is small, Eq. (2.22) can be written as

$$S\frac{\Delta\alpha}{\alpha} = \frac{2n_\parallel\Delta n}{(n_\parallel^2 - 1)(n_\parallel^2 + 2)}\,. \tag{2.23}$$

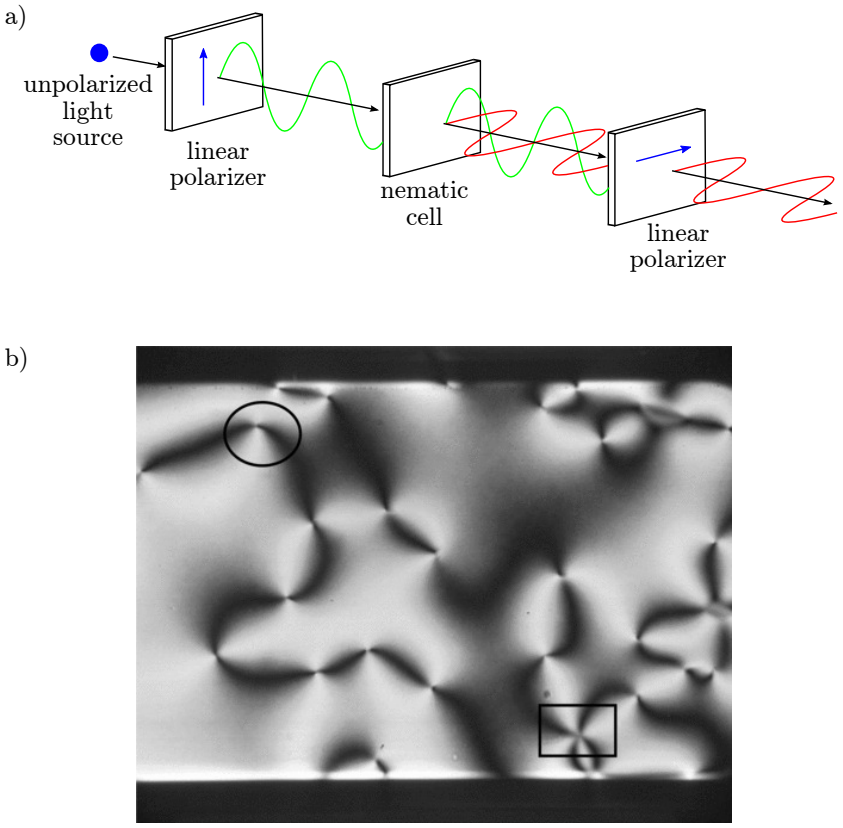


FIGURE 2.4: (a) Schematic illustration of a nematic film placed between crossed polarizers. The polarization direction of the two polarizers is indicated by the blue arrows, which are perpendicular. Unpolarized light is emitted from a source (blue circle) and linearly polarized by the first polarizer. Due to the birefringence of nematic materials, the polarization of light acquires an additional component in a perpendicular direction. Hence, a light signal can be recorded after the second polarizer, which eventually results in a Schlieren texture. (b) Typical example of a Schlieren texture, from Ref. [107]. The circle surrounds a disclination while the square surrounds an hedgehog.

By defining $\Delta n_{\max}$ as the maximum value of the birefringence for a perfectly aligned sample with $S = 1$, Eq. (2.23) gives

$$S = \frac{\Delta n}{\Delta n_{\max}}\,, \tag{2.24}$$

which demonstrates that the birefringence of a fully uniaxial system is proportional to the nematic order parameter. In the next Section we give an example of how the local structure of the director in a nematic film can be inferred from its optical properties.

### 2.2.4 Topological defects

A purely continuous picture as in the FOZ theory cannot describe some fundamental properties of nematic LC. The limitations of a continuous approach become clear when a thin nematic film is placed between crossed polarizers as in Fig. 2.4(a). The term "nematic" (from the greek $\nu\tilde{\eta}\mu\alpha$, "thread") comes from the peculiar texture that a nematic liquid crystal shows in this condition, because some dark filaments (also called

*brushes*) are visible in the sample [69] (see Fig. 2.4(b)). These brushes corresponds to the places in the sample where the nematic director is either parallel or perpendicular to the entering light, which therefore acquires no additional polarization component (the birefringence vanishes when light is linearly polarized along one of the principal axes). Indeed, when rotating the crossed polarizer keeping the nematic film fixed, the brushes also rotate. These brushes can also meet in a single point. The resulting texture is called *Schlieren* texture [108] (see Fig. 2.4(b)). The points where the brushes meet are singularities of the director field, *i.e.* places where the nematic director is not defined, and are called *defects*. Because it is not possible to make a defect disappear with a continuous deformation of the order parameter at finite, arbitrary distance from the core, defects are more properly called *topological defects*.

From the *Schlieren* texture one can already senses that defects can be of different types. For example, typically there are points where either two (circle in Fig. 2.4(b)) or four (square in Fig. 2.4(b)) brushes meet. Also, when rotating the crossed polarizers clockwise, the brushes surrounding one defect can rotate either clockwise or counter-clockwise. The rigorous tool for the classification of defects is provided by homotopy theory, a theoretical framework which allows to group objects depending on their topological properties [109–113]. A formal understanding of topology requires the knowledge of specialized mathematical tools. Our aim here, rather than proceeding rigorously, is to provide the reader with a basic understanding of the physics behind topological defects in liquid crystals. Several reviews provide a much more extensive treatment of the topic [109, 113–116].

A crude, yet efficient, classification of the defects in nematic LC can be directly built from a Schlieren texture [108]. Let us associate to each defect a number, $w$, which counts the number of brushes that meet at the defect core. The absolute value of $w$ is defined as $|w| = \text{number of brushes}/4$. Let us also assign a positive sign to $w$ if the brushes surrounding a defect rotate according to the crossed polarizer and a negative sign vice versa. The number $w$ is called the *winding number* of the defect.

One can relate the winding number to the properties of the director field surrounding a defect. First of all, we should say that because of the inversion symmetry ($\mathbf{n} = -\mathbf{n}$) the nematic director field is a line field rather than a vector field. Therefore the conformation of the field around a defect can be represented by the black lines in Fig. 2.5, where we depicted defects with winding number $w = \pm 1/2, \pm 1$. Consider a circle centered at the defect core with a radius sufficiently large that the field along the circle contour is continuous. Because $\mathbf{n}(\mathbf{r})$ is continuous along the circle, the angular variation, $\Delta\theta$, of the nematic director with respect to a fixed orientation must be a multiple of $\pi$. The proportionality factor between $\Delta\theta$ and $2\pi$ (when crossing the circle counter-clockwise and counting counter-clockwise angle increments as positive) is exactly the winding number of the defect, hence $\Delta\theta = 2w\pi$. Defects with $w = \pm 1/2$ are are called *disclination* and defects with $w = \pm 1$ are called *hedgehog*. Disclinations cannot exist in a vector field, therefore their presence in nematic LCs is a consequence of the symmetry $\mathbf{n} = -\mathbf{n}$.

The topological stability of a defect is a different concept from its physical stability. It depends from the spatial dimension $d$, the dimensionality $n$ of the order parameter and that of the defect core $d_s$. A defect is unstable if $n > d - d_s$. For example, in a system of three dimensional vectors ($n = 3$) on a plane ($d = 2$), a point defect ($d_s = 0$) is unstable. If the vectors surrounding a vortex as in Fig. 2.5(a) are allowed to rotate outside of the figure plane, the topological defect can be continuously deformed into a uniform state,

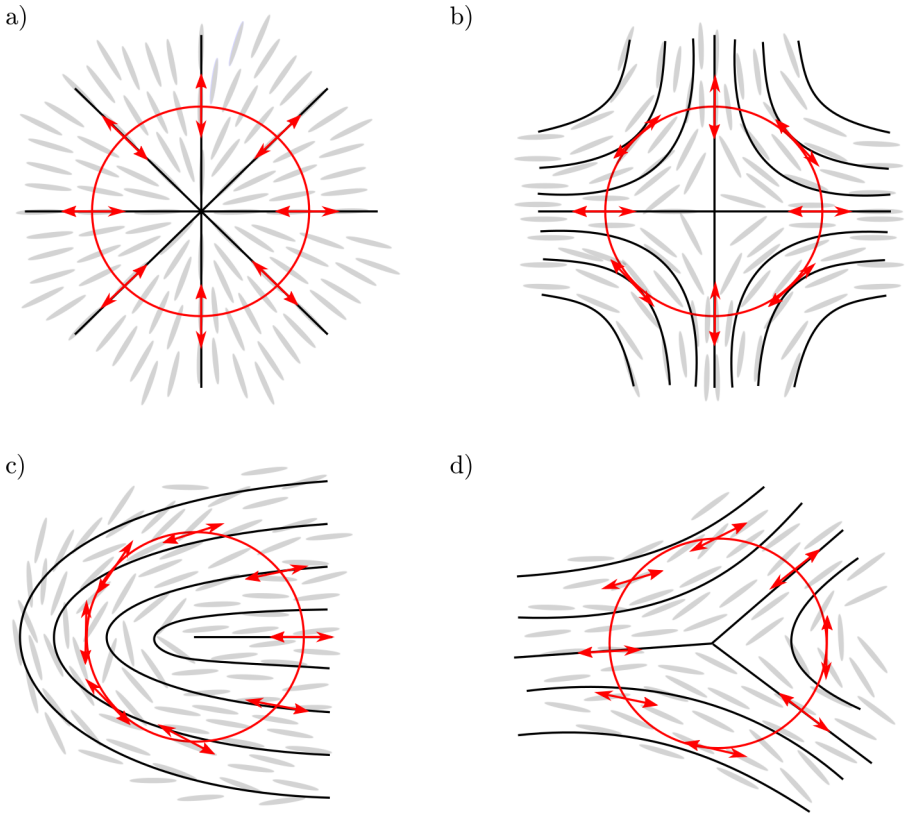


FIGURE 2.5: Topological defects in a nematic liquid crystal with winding numbers (a) $w = +1$, (b) $w = -1$, (c) $w = +1/2$ and (d) $w = -1/2$. The black lines represent the nematic director filed as obtained from the schematic molecular configurations shown in light gray. The red circles represent possible contours surrounding the defect cores along which the rotation of the nematic director (red double arrows) can be evaluated.

a mechanism called *escape to the third dimensions*. On the contrary, a point defect of a two-dimensional order parameter in two dimensions is stable because $n = d - d_s$.

If the circular path surrounding one defect is extended in such a way that it encloses two defects of opposite winding number, the net variation of $\Delta\theta$ along the circular contour is zero. This simple argument reflects the fact that at distances larger than the separation between two defects with opposite winding number, the surrounding field can be continuously distorted into an uniform configuration. Therefore, when coming close, two opposite defects can annihilate each other, which also means that pairs of opposite defects can be created relatively easily. This circumstance is particularly important in two-dimensional systems with the symmetry properties of the $xy$-model, which we discuss in more details in Sec. 2.3.

To conclude, we remark that topological defects are a general consequence of spontaneous symmetry breaking [117] and therefore they are important in a large variety of phenomena. They play an essential role in the phase transitions of two-dimensional models [118, 119], in the Abrikosov vortices of super-conductive materials [120], in the twist-grain boundary phase of liquid-crystal systems [121], and in super-fluid helium [122, 123]. Additionally, defects allow to control the assembly of colloidal particles dispersed in nematic suspensions [41, 99], are useful to understand the structure of biological materials [124], and they even allow to test cosmological models using condensed matter systems [125–127].

## 2.3 Nematic order in two dimensions

In the previous Section we noticed that, due to the non-polar symmetry of the nematic phase, the Landau-de Gennes theory predicts a first-order isotropic-to-nematic transition. Some experimental observations indicate that the transition is only weakly first order [67], which suggest that the third-order coefficient in Eq. (2.15) could be anomalously small.

The situation in two dimensions is more complicated. On the one hand, the Mermin and Wagner theorem states that the spontaneous symmetry breaking of a continuous order parameter is always suppressed by fluctuations in dimensions $d \leq 2$ for systems with sufficiently short-ranged interactions [128, 129]. The theorem readily applies to the standard two-dimensional $xy$-model [130] and, more recently, Bruno rigorously extended the conclusions of the theorem to $xy$-systems with long range interaction [131]. On the other hand, the two-dimensional analogous of the Onsager theory for nematic LC (in which the interaction range is of the order of the molecular length) predicts a transition between a disordered isotropic phase and an orientationally ordered nematic phase [132]. This transition is found to be continuous when solved either by a scaled-particle method [133] or by bifurcation analysis [134], but no definitive conclusion can be made on the stability of the ordered phase.

The long-range stability of a nematic liquid crystal in two dimensions cannot be ruled out *a priori* because, as demonstrated by Straley in 1971 [132], the Mermin and Wagner theorem does not necessarily hold if the interaction between particles is not separable into orientation- and position-dependent terms, which is the case for the hard-core interaction of non-spherical objects. Thus, the possibility for a specific two-dimensional liquid-crystal system to belong to the universality class of the $xy$-model is model dependent and has to be directly investigated in each specific case.

In the $xy$-model, the existence of long-range order is forbidden by the Mermin and Wagner theorem [128, 129]. In 1973, however, Kosterlitz and Thouless (KT) first realized that a transition is still possible between, on the one hand, a disordered phase wherein the correlation function of the orientational order parameter decays exponentially and thereby only exhibits short-range order, and, on the other hand, a phase with quasi-long-range order wherein the correlation function decays as a power law in distance $r$ [118]. In this transition, the topological defects introduced previously play a fundamental role. Because the KT transition is important in the following Chapters of this Thesis, we review its main results in the following.

### 2.3.1 Quasi-long-range orientational order

We start our review of the KT transition by demonstrating that the correlation function of a properly defined order parameter can decay as a power-law in the distance $r$ under certain conditions. Here, we focus on a two-dimensional system with the symmetry properties of a nematic liquid crystal. A nematic phase with quasi-long-range order is called a quasi-nematic phase.

Algebraic order is expected if the free energy associated with the distortion of a director field is of the form

$$F_d = \frac{K}{2} \int [\nabla \theta(\mathbf{r})]^2 \, \mathrm{d}\mathbf{r} \,, \tag{2.25}$$

where $\theta$ is the angle between the local nematic director $\mathbf{n}(\mathbf{r})$ and a fixed axis, and $K$ is the Frank elastic constant. Eq. (2.25) is the two-dimensional analogous of the Frank-Oseen-Zocher elastic energy introduced in Sec. 2.2.2, under the one-constant approximation. In a more general theory, Eq. (2.25) should include two different elastic constants, one for splay and one for bend deformations, but on sufficiently large length scales they renormalize to the same value [135]. A free energy of the type of Eq. (2.25) is also equivalent to a two-dimensional *xy*-model in the *spin-wave* approximation [130] and it is the simplest free energy analytic in $\nabla\theta$ and with an uniform state as a minimum.

We demonstrate now that the free energy of Eq. (2.25) leads to a power-law decay of the correlation function of the nematic order parameter. The two-dimensional analogous of the nematic order parameter defined in Eq. (2.3) is

$$S = \langle \cos(2\theta) \rangle \,. \tag{2.26}$$

where $\langle \dots \rangle$ denotes average over thermal fluctuations. For a system described by Eq. (2.25), true long-range order is forbidden by the Mermin-Wagner theorem [128], therefore $S = 0$ in the thermodynamic limit, $N \to \infty$. In order to characterize orientational order in the quasi-nematic phase, we resort to the orientational correlation function

$$G(r) = \langle \cos[2(\theta(\mathbf{r}) - \theta(0))] \rangle \,, \tag{2.27}$$

which monitors the spatial decay of orientational correlations.

To proceed with the evaluation of Eq. (2.27), we Fourier transform $\theta(\mathbf{r})$ as

$$\theta(\mathbf{r}) = \sum_{\mathbf{k}} \theta_{\mathbf{k}} e^{i\,\mathbf{k}\cdot\mathbf{r}} \,, \tag{2.28}$$

and Eq. (2.25) becomes

$$\mathcal{F}_d = \frac{1}{2} K \Omega \sum_{\mathbf{k}} k^2 |\theta_{\mathbf{k}}|^2 \,. \tag{2.29}$$

where $\Omega$ is the area of the system. The correlation function in Eq. (2.27) can now be evaluated using the Boltzmann distribution with the free energy from Eq. (2.29), *i.e.*,

$$G(r) = \mathrm{Re}\left( \frac{1}{\mathcal{Z}} \int D\,\theta \exp\Big[ - \sum_{\mathbf{k}} \Big( \frac{1}{2} \beta K \Omega k^2 |\theta_{\mathbf{q}}|^2 - 2i\theta_{\mathbf{k}} (e^{i\mathbf{k}\cdot\mathbf{r}} - 1) \Big) \Big] \right) , \tag{2.30}$$

where $\beta = 1/k_{\mathrm{B}}T$ and

$$\mathcal{Z} = \int D\,\theta \exp\Big[ - \sum_{\mathbf{k}} \frac{1}{2} \beta K \Omega k^2 |\theta_{\mathbf{k}}|^2 \Big] \,, \tag{2.31}$$

is the partition function of the system and the integral is performed over all the possible configurations of $\theta(\mathbf{r})$.

It is convenient to separate $\theta_{\mathbf{k}}$ in its real and imaginary parts as

$$\theta_{\mathbf{k}} = A_{\mathbf{k}} + i B_{\mathbf{k}} \,, \tag{2.32}$$

where, since $\theta(\mathbf{r})$ is real, $A_{\mathbf{k}}$ is even and $B_{\mathbf{k}}$ is odd in $\mathbf{k}$. Substituting Eq. (2.32) into Eq. (2.30) the argument of the exponential function in Eq. (2.30) becomes

$$\sum_{\mathbf{k}} \Big( \frac{1}{2}\beta K\Omega k^2 |\theta_{\mathbf{k}}|^2 - 2i\theta_{\mathbf{k}}(e^{i\mathbf{k}\cdot\mathbf{r}} - 1) \Big) =$$
$$\sum_{\mathbf{k}} \Big( \frac{1}{2}\beta K\Omega k^2 (A_{\mathbf{k}}^2 + B_{\mathbf{k}}^2) - 2iA_{\mathbf{k}} \cos(\mathbf{k}\cdot\mathbf{r}) + 2iA_{\mathbf{k}} + 2iB_{\mathbf{k}} \sin(\mathbf{k}\cdot\mathbf{r}) \Big) \tag{2.33}$$

where we left out all the odd terms in $\mathbf{k}$, which cancel because of the summation over $\mathbf{k}$ and $-\mathbf{k}$. Completing the squares, Eq. (2.33) can be written as

$$\sum_{\mathbf{k}} \cdots = \sum_{\mathbf{k}} \frac{1}{2}\beta K\Omega k^2 \left[ \Big( A_{\mathbf{k}} - 2i\frac{\cos(\mathbf{k}\cdot\mathbf{r}) - 1}{\beta K k^2} \Big)^2 + \Big( B_{\mathbf{k}} + 2i\frac{\sin(\mathbf{k}\cdot\mathbf{r})}{\beta K k^2} \Big)^2 \right] +$$
$$+ \sum_{\mathbf{k}} \frac{4}{\beta K\Omega k^2} (1 - \cos(\mathbf{k}\cdot\mathbf{r})) \,. \tag{2.34}$$

The contribution to $G(x)$ coming from the first term on the right hand side of Eq. (2.34) cancels with the partition function in the denominator of Eq. (2.30) (it corresponds to the same gaussian integral as in $\mathcal{Z}$, but shifted) and therefore we are left with

$$G(r) = e^{-h(r)} \tag{2.35}$$

where

$$h(r) = \frac{4}{\beta K\Omega} \sum_{\mathbf{k}} \frac{1 - \cos(\mathbf{k}\cdot\mathbf{r})}{k^2} \,. \tag{2.36}$$

Eq. (2.36) can be evaluated using the substitution

$$\sum_{\mathbf{k}} \to \frac{\Omega}{(2\pi)^2} \int d\mathbf{k} \,, \tag{2.37}$$

which gives

$$h(r) = \frac{2}{\beta K\pi} \int_0^{\Lambda} \frac{dk}{k} \frac{1}{2\pi} \int_0^{2\pi} d\phi [1 - \cos(k|x| \cos\phi)] = \frac{2}{\beta K\pi} \int_0^{\Lambda} \frac{1 - J_0(k|r|)}{k} dk \,, \tag{2.38}$$

where $\phi$ is the angle between $\mathbf{k}$ and $\mathbf{r}$, $\Lambda$ is an ultraviolet cutoff and $J_0(k|r|)$ is a Bessel function. For large $|r|$, Eq. (2.38) behaves as [130]

$$h(r) = \frac{2}{\beta K\pi} \ln(c|r|) \,, \tag{2.39}$$

with $c$ some constant. The asymptotic behavior of the correlation function is therefore

$$G(r) \propto |r|^{-\eta} \tag{2.40}$$

with

$$\eta = \frac{2k_{\mathrm{B}}T}{\pi K} \,. \tag{2.41}$$

Usually, a power-law decay of the correlation function is expected when the temperature of a system is close to the critical temperature of a continuous phase transition. In the quasi-nematic phase, the correlation function decays algebraically over the whole range of

temperatures, where Eq. (2.25) holds, with an exponent that increases with temperature and decreases with increasing elastic constant.

Clearly, Eq. (2.25) is valid as long as the spatial variations of $\theta(\mathbf{r})$ are continuous, *i.e.*, as long as the presence of topological defects can be neglected. Indeed, the quasi-nematic phase is destroyed when the temperature is high enough for topological defects to proliferate, which makes the orientational correlation function decay exponentially. The transition between a phase with proliferating defects (short-range order) and a phase with quasi-long-range order is the KT transition. In the following we discuss an heuristic argument to estimate the conditions under which the free energy in Eq. (2.25) provides a correct description of the system.

### 2.3.2 Disclination unbinding

As anticipated in the previous section, the KT transition is between a disordered phase with exponentially decaying orientational correlation function and a phase, in which the correlation function decays algebraically. A quasi-nematic phase with algebraic order is expected as long as the elastic free energy of Eq. (2.25) provides a correct description of the system, that is as long as topological defects do not proliferate.

To estimate the range of validity of a continuous picture, we start with the evaluation of the energy cost associated with the creation of a topological defect. As discussed in Sec. 2.2.4, the total angular variation along a contour surrounding the defect must be a multiple of $\pi$, *i.e.*,

$$\oint \nabla\theta(\mathbf{r}) \cdot d\mathbf{l} = 2\pi w \,, \tag{2.42}$$

where $w$ is again the winding number of the defect. From Eq. (2.42) it follows that $|\nabla\theta| = w/r$, which can be used in Eq. (2.25) to evaluate the elastic energy of a topological defect

$$E_{\rm td} = \pi K w^2 \int_a^R \frac{dr}{r} = \pi K w^2 \ln(\frac{R}{a}) \,, \tag{2.43}$$

where $R$ is the linear size of the system and $a$ is a small cut-off which corresponds to the size of the defect core. Eq. (2.43) tells us that the energy required to create a defect diverges logarithmically with the system size.

Since a defect can be anywhere in the sample, its entropy can be estimated by counting how many defects with core of size $a$ can be placed in a two-dimensional sample of linear extension $R$, *i.e.*

$$S_{\rm td} = k_{\rm B} \ln(\frac{R^2}{a^2}) \,, \tag{2.44}$$

which also diverges logarithmically with the system size. From Eqs. (2.43) and (2.44), the free energy of a sample with a topological defect becomes:

$$F = E_{\rm td} - TS_{td} = (\pi K w^2 - 2k_{\rm B}T) \ln(R/a) \,. \tag{2.45}$$

According to Kosterlitz and Thouless, a transition results from the competition between the elastic energy needed to create topological defects and the entropy gained when these defects unbind and are thus free to move [130]. In a nematic liquid crystal, defects with the lowest energy have $w = \pm 1/2$ (*disclination*). Therefore, disclination

unbinding takes place at the critical value of the Frank elastic constant [42],

$$\frac{\pi K_c}{8 k_{\mathrm{B}} T} = 1 \,. \tag{2.46}$$

If $K < K_c$, isolated disclinations are found, which leads to an overall isotropic state characterized by an exponential decay of the orientational correlation function. If $K > K_c$, disclinations can still be found, but they are bound in pairs [118] and the orientational correlation function is thus expected to decay algebraically. The critical value, $K_c$, is the result of a balance between the disclination energy and entropy, and in two dimensions both have the same logarithmic dependence on system size. Hence, $K_c$ is a scale-free quantity that locates the transition between short-range and quasi-long-range nematic order in the thermodynamic limit [42].

The KT transition is an important phenomenon found in a large variety of situations: in superconductive two-dimensional array of Josephson junctions [136, 137], in superfluid helium films [138], in two-dimensional arrays of Bose-Einstein condensate [139], in harmonically trapped atomic gases [140], and where a two-dimensional solid melts through the intermediate hexatic phase [56, 141].

In their seminal work, Frenkel and Eppenga where the first to demonstrate that a two-dimensional fluid of hard-needles undergoes an isotropic–quasi-nematic transition via disclination unbinding [60]. More recently, an isotropic–quasi-nematic transition compatible with the KT scenario has been identified in numerical simulations of various two-dimensional liquid-crystal systems [42, 47, 61, 62, 142]. We demonstrate in Sec. 5.3 that the isotropic–quasi-nematic transition in the bent hard-needle model [introduced in Fig. 1.1(c)] is consistent with the KT picture. Examples of the isotropic and quasi-nematic phases of the bent-needle model in the zig-zag and bow-shaped configuration are shown in Fig. 2.6.

Before concluding this section, we note that the isotropic–quasi-nematic transition is continuous for two-dimensional systems described by the elastic free energy in Eq. (2.25) [111]. However, recent investigation showed that the transition can be made first-order by a formally simple generalization of the interaction energy [143–145]. This result further highlights the rich phenomenology of two-dimensional systems.

## 2.4 Smectic order

### 2.4.1 Smectic order in three dimensions

In the smectic mesophase molecules are organized in layers. Therefore they possess, in addition to orientational order, translational order along the layer normal. Positional order is only short-ranged within each layer. Usually, smectic phases occur at lower temperature than nematic. In smectic systems thermal fluctuations prevent the formation of long-range translational order already in three dimensions. This follows when investigating the local displacement $v(\mathbf{r})$ of the layer from its equilibrium position (see Fig. 2.7).

The elastic free energy of a smectic system is obtained by symmetry considerations (see Ref. [130] and Ref. [67]). Assuming that the layers are perpendicular to the $z$-axis,

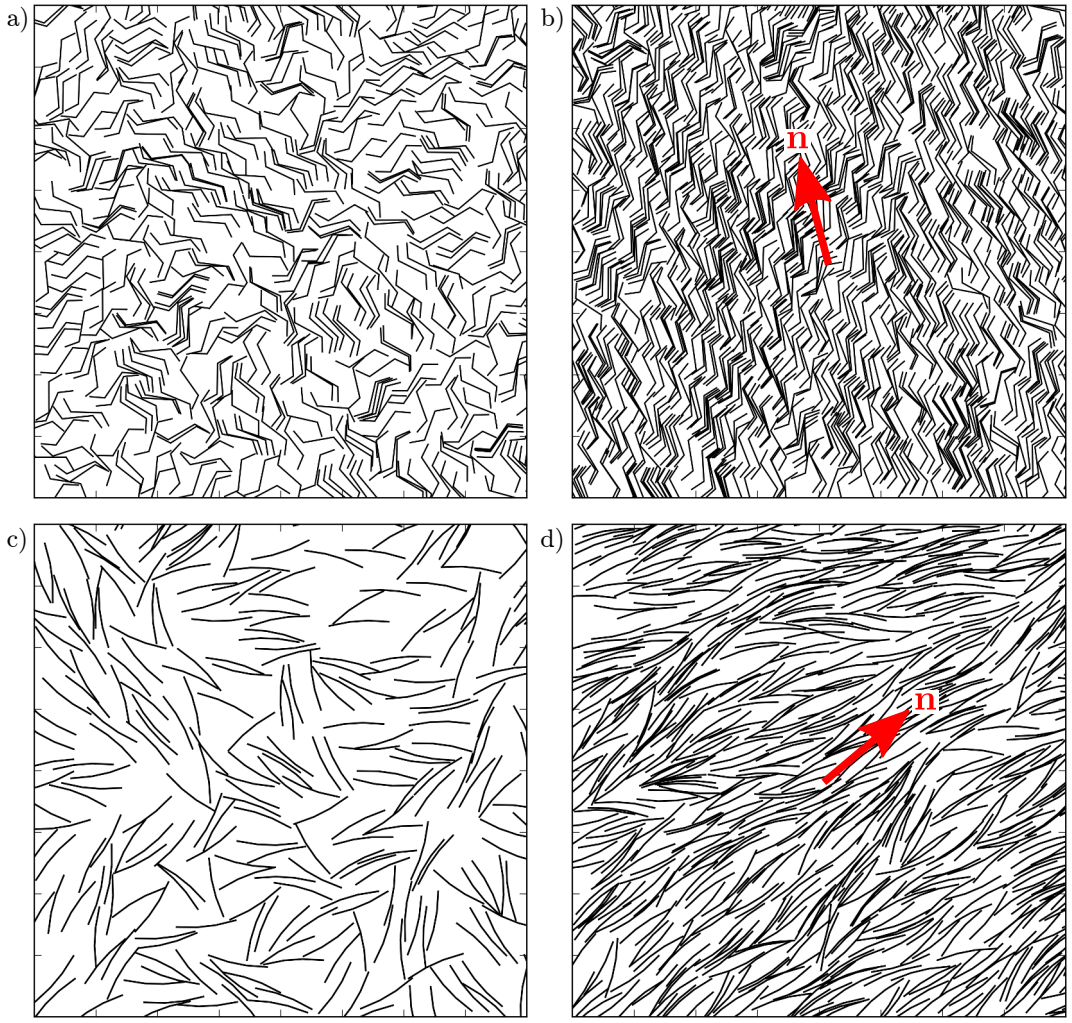


FIGURE 2.6: Molecular configurations obtained from Monte Carlo simulation for both zig-zag and bow-shaped molecules at different values of the density $\rho$. To ease the identification of the mesophase, only a portion of the simulation box is shown, with fixed later size 5 times larger than the total molecular length. (a) Isotropic phase of zig-zag molecules with $a = 0.25$, $\alpha = \pi/3$ and $\rho = 7$. (b) Quasi-nematic phase of zig-zag molecules with $a = 0.25$, $\alpha = \pi/3$ and $\rho = 14$. (c) Isotropic phase of bow-shaped molecules with $a = 0.35$, $\alpha = \pi/25$ and $\rho = 4$. (d) Quasi-nematic phase of bow-shaped molecules with $a = 0.35$, $\alpha = \pi/25$ and $\rho = 10$. The red arrows in (c) and (d) give the nematic director.

it reads

$$F_{\text{sm}} = \frac{1}{2}\int d\mathbf{r}\left[B_1\Big(\frac{\partial v(\mathbf{r})}{\partial z}\Big)^2 + B_2\Big(\frac{\partial^2 v(\mathbf{r})}{\partial x^2} + \frac{\partial^2 v(\mathbf{r})}{\partial y^2}\Big)^2\right], \tag{2.47}$$

where $B_1$ is the elastic constant associated to stretching and compressing the layers and $B_2$ is the elastic constant associated with splay distortions. The Fourier transform of Eq. (2.47) is

$$F_{\text{sm}} = \frac{1}{2(2\pi)^3}\int d^3q\left[B_1 q_z^2 + B_2 q_\perp^4\right]|v(\mathbf{q})|^2, \tag{2.48}$$

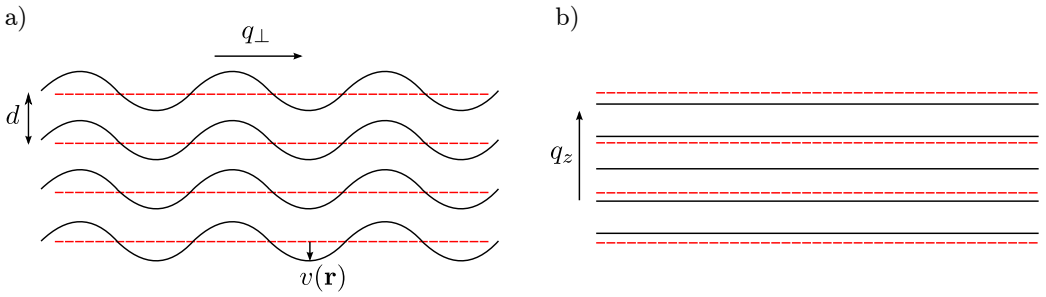


FIGURE 2.7: Elastic deformations in a smectic liquid crystal. The dashed red lines indicate the equilibrium positions of the layers. (a) Splay deformation that keep the inter-layer distance $d$ fixed. The local displacement of the layers from their equilibrium position is given by $v(\mathbf{r})$. (b) Deformation associated with stretching and compressing the layers.

where $q_z$ and $q_\perp$ are defined in Fig. 2.7. Using the equipartition theorem one finds that

$$\langle v^2(\mathbf{r})\rangle \propto \ln(\frac{R}{d})\,, \tag{2.49}$$

where $R$ is the system size and $d$ the equilibrium layer spacing. The mean square fluctuations of the layer displacement logarithmically diverge with the system size, an effect called Landau-Peierls instability. Thus, in analogy to the two-dimensional case of the $xy$-model described in Sec. 2.3.1, the correlation function $\langle v(0)v(\mathbf{r})\rangle$ decays algebraically in three dimensions. The quasi-long-range order in the layers periodicity manifests itself in the power-law singularities of the Bragg peak when performing X-ray analysis [40].

As for the nematic phase, a continuum approach has to be combined with the description of singularities in the displacement field. Topological defects of a periodic structure are called *dislocations* and they can be of two types: screw and edge dislocations. One can think of a screw dislocation as a spiral staircase: the dislocation line is the axis of the spiral along which each layer changes height by half of the layer spacing in half circuit of the core. An edge dislocation can be thought of as resulting from the insertion of additional layers from one side of the defect core. The unbinding of dislocation loops is responsible for the nematic–smectic-A transition [146, 147] and the smectic-A–cholesteric transition in lyotropic systems [148]. Also, screw-dislocation are an essential component of the twist-grain-boundary phase [78, 121].

### 2.4.2 Smectic order in two dimensions

Bound pairs of dislocations play a fundamental role in the melting of two-dimensional solids, which possess only quasi-long-range translational order but true-long-range order in the orientation of nearest-neighbor bonds [119, 141]. Starting from a two-dimensional solid, the unbinding of dislocation pairs produces a fluid with short-range translational order but algebraic decay of bond-angle correlation (the *hexatic* phase). A second transition is necessary to reach the liquid state. Using Monte Carlo simulation, it has recently been demonstrated that the solid-hexatic transition is continuous while the hexatic-liquid transition is of first order [56].

Two-dimensional layered systems are expected to show an analogous two-steps transition. The scenario is discussed in detail in Ref. [149]. In this section, we give a short

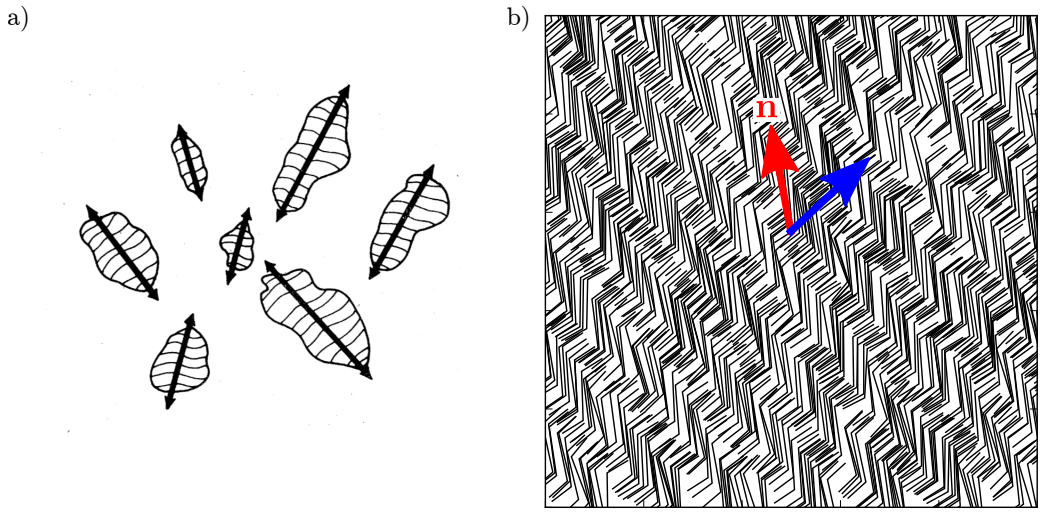


FIGURE 2.8: (a) Schematic picture of the nematic-like structure expected in two-dimensional layered system, from Ref. [149]. The system is divided into smectic islands whose size is controlled by the average separation between dislocations. (b) A snapshot of a portion of the Monte Carlo simulation box illustrates the smectic-C phase formed by zig-zag molecules with $a = 0.25$, $\alpha = \pi/3$ at density $\rho = 30$ in two dimensions. The red arrow indicates the nematic director while the blue arrow is normal to the layers.

summary of the main conclusions of this study. Since layered systems are characterized by a one-dimensional density wave, the translational order parameter $\Phi(\mathbf{r})$ is usually defined as the amplitude of the first harmonic of this wave. In two-dimensional smectics, due to phonon fluctuations, the correlation of the translational order parameter decays exponentially with the distance $r$, *i.e.* $\langle \Phi(\mathbf{r})\Phi(\mathbf{0})\rangle \sim \exp(-r)$, at any finite temperature. These fluctuations are not as effective in decorrelating the layers orientations, which should maintain long-range order [149].

The scenario changes drastically upon considering the effect of a finite density of dislocations. The mean separation between two thermally induced dislocations is

$$\xi_{\rm d} \approx a \exp(\frac{E_{\rm d}}{2k_{\rm B}T}) \,, \tag{2.50}$$

where $a$ is the size of the defect core and $E_{\rm d}$ is the energy of the dislocation. The length scale over which the layer orientations are correlated is fixed by $\xi_{\rm d}$. One thus expects to find the system divided into "islands" of linear size $\sim \xi_{\rm d}$, as illustrated in Fig. 2.8(a). Within each island, translational order is decorrelated by phonon fluctuations, but the layer orientations are strongly correlated. For distances much larger than $\xi_{\rm d}$ the properties of a two-dimensional layered system are instead those of a quasi-nematic phase, with the correlations between the layer orientations following a power-law decay.

The snapshot of a Monte Carlo simulation shown in Fig. 2.8(b) gives an example of the smectic-C phase formed by zig-zag molecules at high packing density. As the area in the snapshot is approximately 40% of the total simulation area, one can already senses that the smectic phase is well stabilized in our numerical simulations. Indeed, we anticipate that we were unable to test the expected scenario, depicted in Fig. 2.8(a), due to the limitation imposed by the finite size of the system. Details on the smectic phase formed by zig-zag molecules are given in Sec. 5.4.

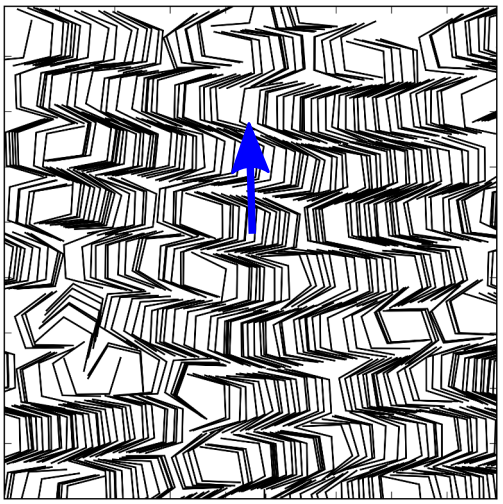

FIGURE 2.9: The anti-ferromorphic smectic-A phase of bow-shaped molecules with $a = 0.35$, $\alpha = 2\pi/5$ at density $\rho = 30$ from a snapshot of a portion of the Monte Carlo simulation box. The blue arrow indicates the direction normal to the layers. It can be seen that molecules have opposite orientation in adjacent layers.

### 2.4.3 Polar smectic phases

Another relevant topic for our molecular model is the existence of polar smectic phases, which possess ferro- or antiferro-electric properties. The first polar smectic phases were chiral phases of the smectic-C type formed by chiral mesogens, which carry an an electric dipole moment [150]. It was soon realized that such phases can also be obtained by dispersing few chiral molecules in a non-chiral smectic-C liquid-crystal host [151]. In these mesophases, the chirality results from the tilt with respect to the layer normal and the polarity from the intra-layer ordering.

The possibility to obtain a chiral phase by employing achiral mesogens has been a subject of debate for long time, until it was found in 1997 that achiral, bent-core mesogens were indeed able to spontaneously assemble in chiral smectic phases [152]. At approximately the same time, in 1996, an achiral (not twisted) and polar smectic phase, also formed by bent-core molecules, was discovered [84]. Since then, interest in bent-core or *banana-shaped* molecules has grown enormously. Such mesogens are able to form a large variety of mesophases (denoted with the letter $B$) [80, 81] and they even provided the first experimental evidence for a thermotropic biaxial nematic phase [153].

Polar smectic phases can exhibit ferro- or antiferro-electric properties depending on the relative orientation of polarization in adjacent layers. In these systems, due to the high packing density within each layer, the molecular dipoles are aligned in a direction perpendicular to the layer normal. If the dipoles have the same orientation in each layer, the material possesses ferro-electric properties, as in Ref. [84]. This configuration is thus called ferromorphic. In Ref. [154] instead, the orientation of the dipoles alternates from layer to layer, which results in anti-ferroelectric properties. This configuration is called anti-ferromorphic.

The possibility to obtain such structures in three dimensions by only considering molecular steric interactions has been studied in Refs. [155] and [156] using Monte Carlo simulation. The hard-core spherocylinder dimers considered in Ref. [156] only showed evidence for an anti-ferromorphic smectic-A phase. Quantitative free-energy calculations

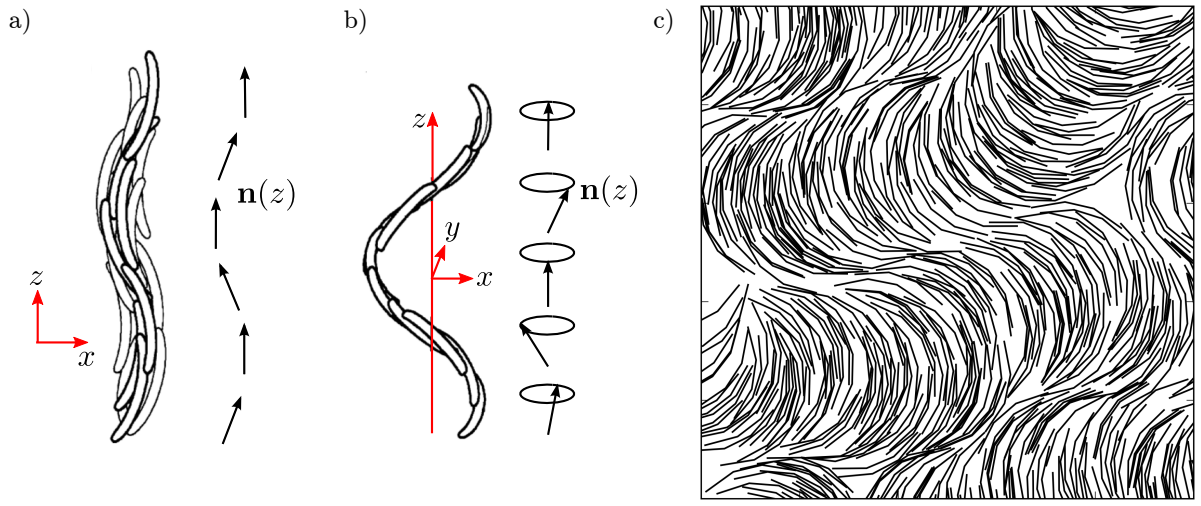


FIGURE 2.10: The spontaneous, stable deformation of the nematic director in banana-shaped molecular systems are schematically illustrated in (a) and (b) (adapted from [57]). In (a) the nematic director forms spontaneous splay-bend deformation while in (b) the deformation gives rise to a conical twist-bend helix. (c) A snapshot of the simulation box from a Monte Carlo simulation of bow-shaped molecules with $a = 0.35$, $\alpha = \pi/8$ at density $\rho = 20$ illustrating the two-dimensional modulated nematic phase. To ease the identification of the mesophase, only a portion of the simulation box is shown.

demonstrated that the anti-ferromorphic arrangement is energetically favoured over the ferromorphic [156].

Bow-shaped molecules [see Fig. 1.1(c)] also arrange in an anti-ferromorphic smectic-A phase if the angle between the central and the external segments is sufficiently high and if very closely packed. This can be clearly seen in the molecular configuration obtained from the Monte Carlo simulation shown in Fig. 2.9. We discuss the possible reasons behind this rather unusual ordering in Sec. 5.4.

## 2.5 Distorted nematic phases

The striking features of bent-core or banana-shaped compounds are not limited to the wide variety of smectic phases that they can form. Meyer was the first, in 1969, to suggest that flexoelectricity (the ability to generate a spontaneous polarization in response to a distortion of the nematic director) should be favored by a mesogen shaped like a banana [157]. The predicted effect was experimentally confirmed only very recently [158].

Three decades after the prediction by Meyer, Dozov suggested that bent-core mesogens could give rise to a whole new class of nematic phases [57]. In Ref. [57], the possible occurrence of a nematic phase with stable splay-bend or twist-bend deformations is discussed as resulting from pathological elasticity, *i.e.*, from negative-valued elastic constants. Starting from a Frank-Oseen-Zocher elastic free-energy as in Eq. (2.16), spontaneous bend deformations of the nematic director can be obtained by using a negative $K_3$. Indeed, nothing prevents the Frank elastic constant to be negative besides the requirement of a uniform ground state. To stabilize the resulting phase and to limit the free energy, fourth-order elastic terms in $\nabla_\alpha n_\beta$ need to be taken into account.

Assuming for simplicity that the nematic director $\mathbf{n}$ is uniform in the $xy$-plane and that it only depends on $z$, there are only three fourth-order terms compatible with the nematic symmetry. The free energy then reads [57]

$$\mathcal{F} = \mathcal{F}_{\rm d} + \frac{1}{4}\left[C_1\Big(\frac{d^2 n_\alpha n_\beta}{dz^2}\Big)^2 + 2C_2\Big(\frac{d^2 n_z n_\beta}{dz^2}\Big)^2 + C_3\Big(\frac{d^2 n_z^2}{dz^2}\Big)^2\right], \tag{2.51}$$

where $n_z$ is the $z$-component of $\mathbf{n}$, $\mathcal{F}_{\rm d}$ is as in Eq. (2.16), the $C_i > 0$ are additional elastic constants, and summation over repeated indexes is assumed. Equation (2.51) admits two stable solutions, illustrated in Figs. 2.10(a) and 2.10(b): a modulated nematic phase with splay-bend deformations and a conical twist-bend helix phase.

In 2002, the twist-bend nematic phase has been observed in three-dimensional molecular computer simulation using banana-shaped molecules interacting through a Gay-Berne potential [59]. Experimentally, the helical twist-bend nematic phase predicted by Dozov was first discovered in 2013 by Noel Clark and collaborators [86]. Using achiral dimer molecules (cyanobiphenyl-$(CH_2)_7$-cyanobiphenyl) they realized a stable modulated nematic phase with a pitch of few molecular lengths. The phase is not smectic since it shows no modulations in the molecular density. Further investigations demonstrated that in this phase the bend elastic constant $K_3$ is, as expected, anomalously small [58].

In Sec. 5.5 we demonstrate that bow-shaped molecules in two dimensions arrange in a modulated nematic phase with splay-bend deformation. This phase consists of layers made up of arches formed by several molecules. Our results represent the first evidence for a modulated-nematic phase in two dimensions, and additionally demonstrate for the first time that such a phase can be stabilized by only considering steric interactions. A snapshot showing the bow-shaped molecules in the modulated-nematic phase is shown in Fig. 2.10(c).

## 2.6 Onsager theory

In Sec. 2.2.1 we introduced the Onsager theory [92] for a system of hard rods. We showed that, at sufficiently high density, nematic order is favored since the decrease of orientational entropy is compensated by the increase in translational entropy. A generalization of the theory allows for the determination of the phase behavior of fluids composed of anisotropic molecules of more complex shapes [46, 63]. Indeed, in Sec. 5.6 we use Onsager theory as an alternative method for calculating the phase diagrams of the bent-needle model. Part of the work presented in Secs. 2.6.2 and 2.6.3 has been published in Ref. [A].

### 2.6.1 Virial expansion

We start by shortly discussing the simple case of a monoatomic gas of $N$ identical particles of mass $m$ in a volume $V$ at temperature $T$, which is very useful to illustrate the main assumption behind the Onsager approach. We are interested in obtaining the free energy, $F$, which in the canonical ensemble is given by

$$\beta F = -\ln Z\,, \tag{2.52}$$

where $Z$ is the partition function

$$Z = \frac{1}{N!}\frac{1}{h^{3N}}\int d^3q_1 \cdots d^3q_N\, d^3p_1 \ldots d^3p_N\; e^{-\beta\mathcal{H}(p_1,\ldots,p_N,q_1,\ldots,q_N)}\,. \tag{2.53}$$

Here $h$ is the Planck constant, the $q_i$ are the particle positions, the $p_i$ the conjugate momenta, $\beta = 1/k_{\mathrm{B}}T$, and $\mathcal{H}$ is the Hamiltonian. In classical systems

$$\mathcal{H}(p_1,\ldots,p_N,q_1,\ldots,q_N) = \sum_{i=1}^{N}\frac{p_i^2}{2m} + U(q_1,\ldots,q_N)\,, \tag{2.54}$$

therefore the partition function splits up into a product of an integral over the momenta and an integral over the coordinates. Because for an ideal gas of non-interacting particles ($U = 0$) one has

$$Z_{\mathrm{ig}} = \frac{1}{N!}\frac{1}{h^{3N}}\Big(\frac{V}{\lambda_{th}^3}\Big)^N\,, \tag{2.55}$$

where $\lambda_{th} = h/\sqrt{2\pi m k_{\mathrm{B}}T}$ is the thermal de Broglie wavelength, it is convenient to rewrite Eq. (2.53) as

$$Z = Z_{\mathrm{ig}}\mathcal{Q}_N\,, \tag{2.56}$$

where

$$\mathcal{Q}_N = \frac{1}{V^N}\int d^3q_1 \ldots d^3q_N\; e^{-\beta U(q_1,\ldots,q_N)}\,, \tag{2.57}$$

is the contribution of the interaction potential to the partition function. In this way the free energy $F$ in Eq. (2.52) can be expressed as the sum of the free energy of an ideal gas, $\beta F_{\mathrm{ig}} = -\ln Z_{\mathrm{ig}}$, and a term, which takes into account the molecular interactions, *i.e.*,

$$\beta F = \beta F_{\mathrm{ig}} - \ln \mathcal{Q}_N\,. \tag{2.58}$$

To evaluate $\mathcal{Q}_N$, it is useful to rewrite Eq. (2.57) as

$$\mathcal{Q}_N = \frac{1}{V^N}\int d^3q_1 \ldots d^3q_N\; \Big(e^{-\beta U(q_1,\ldots,q_N)} - 1\Big) + 1\,, \tag{2.59}$$

and to consider that the interaction between particles becomes relevant only when particles are very close to each other, *i.e.*, when they nearly collide. If the gas is sufficiently dilute, we can assume that only isolated binary interactions take place and, since there are $N(N-1)/2$ ways of choosing a pair of particles in our system, we can write

$$\begin{aligned}
&\frac{1}{V^N}\int d^3q_1 \ldots d^3q_N\; \Big(e^{-\beta U(q_1,\ldots,q_N)} - 1\Big) \\
&= \frac{1}{V^N}\frac{N(N-1)}{2}\int d^3q_1 \ldots d^3q_N\; \Big(e^{-\beta U_{12}} - 1\Big) \\
&= \frac{1}{V^N}\frac{N(N-1)}{2}V^{N-2}\int d^3q_1 d^3q_2\; \Big(e^{-\beta U_{12}} - 1\Big) \\
&\approx \frac{1}{2}\frac{N^2}{V}\int d^3q\; \Big(e^{-\beta U_{12}} - 1\Big)\,,
\end{aligned} \tag{2.60}$$

where $U_{12}$ is the interaction potential between two particles, we used $N(N-1) \approx N^2$ and, in the last step, we evaluated the integral over the coordinates $\mathbf{q}$ of the center of

gravity of the two particles (assuming that $U_{12}$ only depends on their mutual distance). By defining

$$B_2 = \frac{1}{2}\int d^3q \left(e^{-\beta U_{12}} - 1\right), \tag{2.61}$$

and using $\ln(1+x) \approx x$ for $x \ll 1$ we can finally write

$$\ln \mathcal{Q}_N = \ln\left(\frac{1}{V^N}\int d^3q_1 \ldots d^3q_N \; e^{-\beta U(q_1,\ldots,q_N)}\right) \approx \frac{N^2}{V} B_2 \tag{2.62}$$

which, substituted in Eq. (2.58), gives the lowest order correction to the free energy of an ideal gas.

Higher-order terms can be obtained by progressively considering interactions between three, four, etc. particles. They correspond respectively to additional coefficients $B_3$, $B_4$, etc [159], which are called *virial coefficients* and depend on the specific interaction potential.

### 2.6.2 Application to non-spherical hard-core particles

In Ref. [63], the Onsager theory was used to determine the phase behavior of zig-zag molecules. In the following, we summarize and extend the results of this Onsager theory.

The conclusions of the previous Section can be easily applied to the hard-core, orientation-dependent interaction of bent needles. The differential volume $d^3q$ in Eq. (2.53) has to be replaced by a differential volume over the spatial positions, $\mathbf{r}$, of the particles and a differential volume over their orientation, defined by some unit vector $\boldsymbol{\omega}$. Indeed, the integration over the positions gives the volume $V$, while the integral over the angles only gives a constant that can always be normalized to unity [159].

Since the pair potential for hard-core particles is

$$\begin{aligned} &U_{12}(\mathbf{r}_1, \mathbf{r}_2, \boldsymbol{\omega}_1, \boldsymbol{\omega}_2) = \infty \quad \text{if particles overlap} \\ &U_{12}(\mathbf{r}_1, \mathbf{r}_2, \boldsymbol{\omega}_1, \boldsymbol{\omega}_2) = 0 \quad \text{otherwise}, \end{aligned} \tag{2.63}$$

it is convenient to introduce the Mayer function of the pair potential

$$f_{\mathrm{M}} = e^{-\beta U_{12}} - 1, \tag{2.64}$$

which is zero except when particles overlap, where $f_M = -1$. Up to a second-order virial expansion, the Onsager free energy functional is thus

$$\begin{aligned} \beta F = &\int d\boldsymbol{r} \int d\boldsymbol{\omega} \rho(\boldsymbol{r}, \boldsymbol{\omega}) \big\{ \ln \rho(\boldsymbol{r}, \boldsymbol{\omega}) - 1 \big\} \\ -\frac{1}{2}&\int d\boldsymbol{r}_1 \int d\boldsymbol{\omega}_1 \rho(\boldsymbol{r}_1, \boldsymbol{\omega}_1) \int d\boldsymbol{r}_2 \int d\boldsymbol{\omega}_2 \rho(\boldsymbol{r}_2, \boldsymbol{\omega}_2) f_M(\boldsymbol{r}_{12}, \boldsymbol{\omega}_1, \boldsymbol{\omega}_2), \end{aligned} \tag{2.65}$$

where $\rho(\boldsymbol{r}, \boldsymbol{\omega})$ is the local number density at position $\mathbf{r}$ and orientation $\boldsymbol{\omega}$, normalized such that

$$N = \int d\boldsymbol{r} \int d\boldsymbol{\omega} \rho(\boldsymbol{r}, \boldsymbol{\omega}). \tag{2.66}$$

Our stategy now is to simplify Eq. (2.65) in order to minimize the free energy and to obtain transition densities between different mesophases.

In the isotropic and nematic phases, positional order does not exist and one has $\rho(\vec{r},\vec{\omega}) = \rho f(\vec{\omega})$ that substituted in Eq. (2.66) gives

$$\int d\boldsymbol{\omega} f(\boldsymbol{\omega}) = 1\,, \tag{2.67}$$

where we used $\rho = N/V$. The domain of definition of $f(\boldsymbol{\omega})$ depends on the symmetry properties of the molecules. Since our molecules are constrained to a two-dimensional surface, zig-zag molecules are symmetric with respect to rotation by $\pi$ while bow-shaped molecules are symmetric with respect to rotation by $2\pi$. Therefore, Eq. (2.67) becomes

$$\int_0^{m\pi} d\theta f(\theta) = 1\,, \tag{2.68}$$

where we introduced an index $m = 1$ for zig-zag molecules and $m = 2$ for bow-shaped molecules.

Integration of Eq. (2.65) over $\boldsymbol{r}$ gives

$$\begin{aligned}\frac{\beta F}{A} =& \rho \ln \rho - \rho + \rho \int_0^{m\pi} d\theta f(\theta) \ln(m\pi f(\theta)) \\ &+ \frac{1}{2}\rho^2 \int_0^{m\pi} d\theta_1 \int_0^{m\pi} d\theta_2 f(\theta_1) f(\theta_2) A_{\text{exl}}(\Delta\theta)\,,\end{aligned} \tag{2.69}$$

where $A$ is the area of the system (we are now explicitly in two dimensions), $A_{\text{exl}}(\Delta\theta)$ is the excluded area in terms of the angle $\Delta\theta$ between two molecular orientations. We also added a term $\ln(m\pi)$for later convenience, which does not change the phase behavior.

Before proceeding to the minimization, it is convenient to Fourier transform the orientational distribution function and the excluded area. They are both even functions, thus

$$f(\theta) = \sum_{i=0}^{n} f_i \cos(2i\theta/m) \quad \text{and} \quad A_{\text{exl}}(\Delta\theta) = \sum_{i=0}^{n} A_i \cos(2i\Delta\theta/m)\,, \tag{2.70}$$

where $f_0 = 1/m\pi$ is fixed by Eq. (2.68). The free energy in Eq. (2.65) is evaluated by substituting $A_{exl}(\Delta\theta)$ and $f(\theta)$ with the respective Fourier transforms and by using the orthogonal properties of trigonometric functions

$$\int_0^{\Lambda} d\theta \cos(n\frac{2\pi}{\Lambda}\theta)\cos(n'\frac{2\pi}{\Lambda}\theta) = \begin{cases} \Lambda & n = n' = 0 \\ \frac{\Lambda}{2} & n = n' \neq 0 \\ 0 & n \neq n' \end{cases} \tag{2.71}$$

and

$$\int_0^{\Lambda} d\theta \cos(n\frac{2\pi}{\Lambda}\theta)\sin(n'\frac{2\pi}{\Lambda}\theta) = 0\,, \tag{2.72}$$

together with the cosine addition formula for $\cos(\Delta\theta) = \cos(\theta_1 - \theta_2)$.

After some algebra we obtain

$$\frac{\beta F}{A} = \rho \ln \rho - \rho + \rho \sum_{i=0}^{n} f_i \int_0^{m\pi} d\theta \cos(2i\theta/m) \ln \Big[1 + m\pi \sum_{j=1}^{n} f_j \cos(2j\theta/m)\Big] + \frac{1}{2}\rho^2 A_0 + \rho^2 \Big(\frac{m\pi}{2}\Big)^2 \sum_{i=0}^{n} f_i^2 A_i \,. \tag{2.73}$$

Minimization with respect to the Fourier amplitude $f_i$ of $f(\theta)$ gives

$$\int_0^{m\pi} d\theta \cos(2i\theta/m) \ln \Big[1 + m\pi \sum_{j=1}^{n} f_j \cos(2j\theta/m)\Big] + \rho \Big(\frac{m\pi}{2}\Big)^2 f_i A_i = 0 \,, \tag{2.74}$$

and using $\ln(1+x) \approx x$, we obtain

$$m\pi \sum_{j=1}^{n} f_j \int_0^{m\pi} d\theta \cos(2i\theta/m) \cos(2j\theta/m) + \rho \Big(\frac{m\pi}{2}\Big)^2 f_i A_i = 0 \,. \tag{2.75}$$

By using again the orthogonal properties of trigonometric functions, Eq. (2.75) gives the values of the densities which minimize the Onsager free energy, *i.e.*

$$\rho_B^{(i)} = -\frac{2}{A_i} \,. \tag{2.76}$$

We interpret the $\rho_B^{(i)}$ as a series of possible bifurcation densities. In particular, we choose the lowest positive value of $\rho_B^{(i)}$ as the isotropic-nematic transition density $\rho_{\mathrm{IN}}$, which is realized at $i = 1$ for zig-zag molecules and at $i = 2$ for bow-shaped molecules. The resulting transition lines are plotted as red dashed lines in the phase diagrams of Fig. 5.9 in Chapter 5. We determine the Fourier coefficients $A_i$ numerically by means of the Monte Carlo integration technique described in the following section.

To determine the nematic–smectic transition density $\rho_{\mathrm{NS}}$, we choose a periodic modulation of the density along the $z$ axis, $\rho(\vec{r}) = \rho(z) = \rho(z+d)$, and assume perfect alignment of the molecules as in Ref. [63], because the nematic order in the smectic phase is typically very high. The evaluation of the free energy functional now involves an excluded distance $d_{\mathrm{excl}}(z,\theta)$, where $\theta$ is the orientation angle of the central molecular segment with respect to the smectic layer normal. The excluded distance is related to the excluded area by $A_{\mathrm{excl}} = \int dz\, d_{\mathrm{excl}}(z,\theta)$. Taking into account only the first Fourier mode of the density modulation in the free energy and minimizing with respect to the Fourier amplitude, we obtain an equation for the nematic–smectic transition density $\rho_{\mathrm{NS}}$,

$$1 + \rho_{\mathrm{NS}} \int \cos(2\pi z/d) d_{\mathrm{excl}}(z,\theta)\, dz = 0 \,, \tag{2.77}$$

where $d$ is the smectic period. The tilt angle $\theta$ and the period $d$ are also determined by minimizing the free energy functional. For details of the calculation, we refer the reader to the work of Varga *et al.* [63]. Note that we were only able to calculate a nematic–smectic transition line for zig-zag molecules. It is plotted in the phase diagram of Fig. 5.9(a) as blue dotted line.

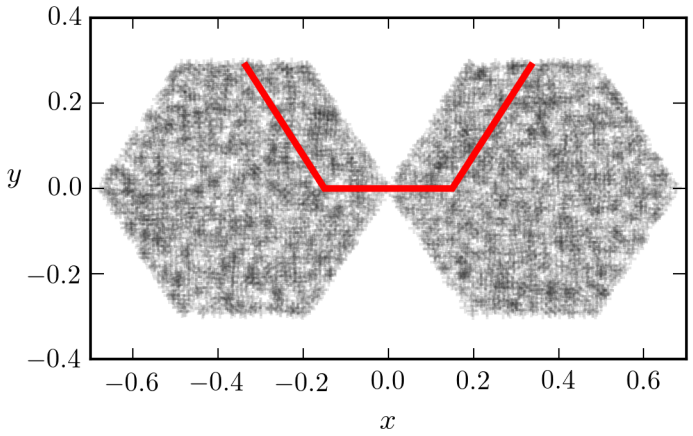


FIGURE 2.11: Illustration of the calculation of the excluded area for bow-shaped molecules with $\alpha = 57.3°$, $a = 0.35$ and the same orientation. The excluded area is obtained by repeatedly inserting the second molecule inside the box and checking for overlaps. The shaded region is obtained by placing a dot at the position of the center of mass of a randomly inserted particle if it overlaps with the fixed particle.

### 2.6.3 Numerical evaluation of the excluded area

The determination of the bifurcation densities in Eq. (2.76) requires the determination of the Fourier amplitudes of the excluded area $A_{\text{excl}}(\Delta\theta)$, which we obtain numerically.

As anticipated in Sec. 2.2.1, given two molecules with a fixed relative orientation $\Delta\theta$, then the excluded area $A_{\text{excl}}(\Delta\theta)$ is defined as the portion of the plane surrounding a molecule that is not accessible to the other. If the center of the second molecule is inside the area excluded by the first, then the molecules overlap. Figure 2.11 shows an example of the shape of the excluded area for two bow-shaped molecules with the same orientation ($\Delta\theta = 0$). As clearly shown by Eq. (2.65) for hard-core potentials, the excluded area is proportional to the second virial coefficient in an expansion of the free energy in powers of density. Hence, $A_{\text{excl}}$ provides a microscopic description of the balance between positional and orientational entropy.

We evaluate the excluded area by Monte Carlo integration. One molecule is fixed at the center of a box of area $A_{\text{box}}$. The size of the box is chosen such that it is impossible for a molecule outside the box to overlap with the fixed molecule. Another molecule with fixed relative orientation $\Delta\theta$ is then inserted at random in the box. The process is repeated $N_{\text{trial}}$ times, keeping track of the number of overlaps $N_{\text{overlap}}$ that occur during the whole process. In the end, the excluded area is $A_{\text{excl}}(\Delta\theta) = A_{\text{box}}(N_{\text{overlap}}/N_{\text{trial}})$. The Fourier amplitudes, $A_i$, who appear in Eq. (2.76) are then obtained via

$$A_i = \frac{2}{m\pi} \int_0^{m\pi} A_{\text{excl}}(x) \cos\left(\frac{2ix}{m}\right) dx \,, \tag{2.78}$$

where, again, we used $m = 1$ for zig-zag molecules and $m = 2$ for bow-shaped molecules.

## 2.7 Order parameters

In the previous Sections we showed that zig-zag molecules arrange in isotropic [Fig. 2.6(a)], quasi-nematic [Fig. 2.6(b)], and smectic-C [Fig. 2.8(b)] phases, while bow-shaped molecules arrange in isotropic [Fig. 2.6(c)], quasi-nematic [Fig. 2.6(d)], modulated-nematic [Fig. 2.10(c)], and anti-ferromorphic smectic-A [Fig. 2.9] phases. In this section we summarize and detail the definition of the order parameters and the related correlation functions used to map out the phase diagram of the bent-needle model.

We define the two-dimensional nematic order parameter $S$ by first introducing the two-dimensional tensor order parameter $\boldsymbol{Q}$:

$$Q_{\alpha\beta} = \langle N^{-1} \sum_{i=1}^{N} (2u_\alpha^i u_\beta^i - \delta_{\alpha\beta}) \rangle \,, \tag{2.79}$$

where $u_\alpha^i$ is the $\alpha$-th Cartesian coordinate of the unit vector pointing along the central segment of the $i$-th of $N$ molecules [see Fig. 1.1(c)] and $\langle \ldots \rangle$ denotes the ensemble average. The positive eigenvalue and corresponding eigenvector of $\mathbf{Q}$ give $S$ and the nematic director $\boldsymbol{n}$, respectively. As discussed in Sec. 2.3, in two dimensions only quasi-long-range orientational, i.e., quasi-nematic, order can exist, and hence we resort to the orientational correlation function to characterize orientational order in the quasi-nematic phase,

$$g_2(r) = \langle \cos[2(\theta(0) - \theta(r))] \rangle \,, \tag{2.80}$$

where $\theta$ is the angle between the central molecular segment along $\hat{\boldsymbol{u}}$ and a fixed axis, and $r$ is the distance between the centers of two molecules. The function $g_2(r)$ thus monitors the spatial decay of orientational correlations. Note that because we work under periodic boundary conditions, correlation functions are radially truncated at half the edge length of the simulation box.

A smectic liquid crystal can be thought of as a stack of parallel molecular layers of thickness $d$. It is therefore possible to identify a density wave along the normal to the layers. The smectic order parameter $\Lambda_{\mathrm{sm}}$ is then the amplitude of this density wave. To determine $\Lambda_{\mathrm{sm}}$, we calculate the Fourier transform of the normalized density [160],

$$\Lambda(\hat{\boldsymbol{k}}, d) = \left\langle \frac{1}{N} \left| \sum_{j=1}^{N} e^{i\boldsymbol{k}\cdot\boldsymbol{r}_j} \right| \right\rangle , \tag{2.81}$$

where $\boldsymbol{r}_j$ is the position of the $j$-th particle, and $\boldsymbol{k} = (2\pi/d)\hat{\boldsymbol{k}}$ is the wave vector with wavelength $d$ and unit vector $\hat{\boldsymbol{k}}$. To determine the actual distance $d$ between smectic layers and the layer orientation $\hat{\boldsymbol{k}}$, we calculate $\Lambda(\hat{\boldsymbol{k}}, d)$ for different values of $d$ and directions $\hat{\boldsymbol{k}}$, and take its maximum $\Lambda_{\mathrm{sm}}$ as the smectic order parameter[51]. Figure 2.12(a) illustrates this optimization procedure.

Bow-shaped molecules are able to display polar order, which we quantify by introducing the global polar order parameter

$$P_{\mathrm{g}} = \left| \frac{1}{N} \sum_{i=1}^{N} \hat{\boldsymbol{v}}^i \right| , \tag{2.82}$$

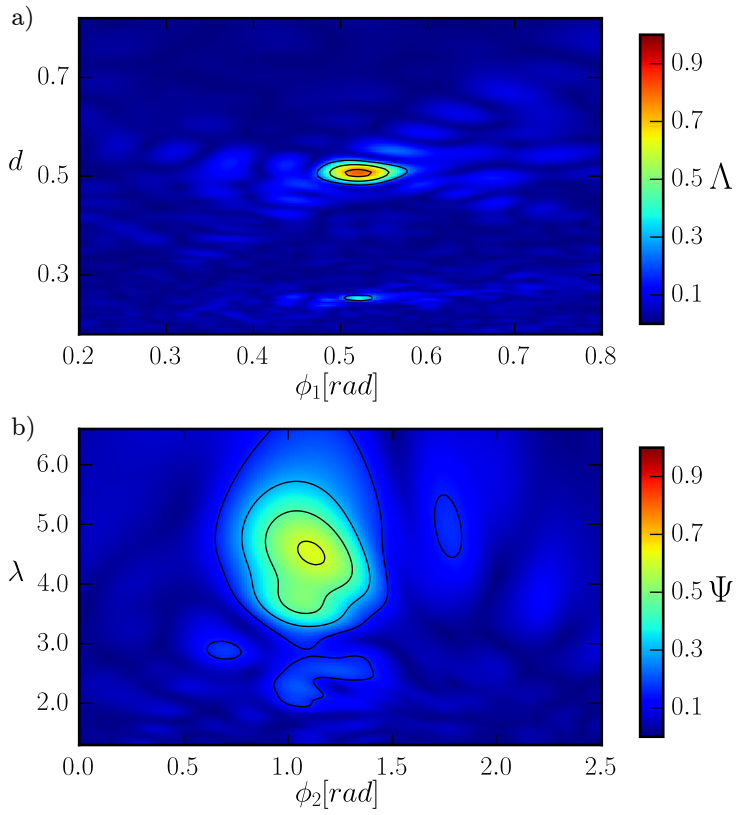


FIGURE 2.12: Illustration of the maximization procedure for determining the smectic (a) and modulated-nematic (b) order parameter. (a) Fourier transform of the density, $\Lambda(\hat{\boldsymbol{k}}, d)$, plotted versus orientation angle $\phi_1$ and wavelength $d$ of the wave vector $\boldsymbol{k} = (2\pi/d)\hat{\boldsymbol{k}}$ with $\hat{\boldsymbol{k}} = [\cos\phi_1, \sin\phi_1]$. The data refer to zig-zag molecules with $a = 0.25$, $\alpha = \pi/2$, and $\rho = 30$. The maximization gives $\Lambda_{\mathrm{sm}} = 0.83$. (b) Fourier transform of the polar order parameter, $\Psi(\hat{\boldsymbol{h}}, \lambda)$, plotted versus orientation angle $\phi_2$ and wavelength $\lambda$ of the wave vector $\boldsymbol{h} = (2\pi/\lambda)\hat{\boldsymbol{h}}$ with $\hat{\boldsymbol{h}} = [\cos\phi_2, \sin\phi_2]$. The data refer to bow-shaped molecules with $a = 0.35$, $\alpha = \pi/13$, $\rho = 24$. The maximization gives $\Psi_{\mathrm{m}} = 0.62$. In both cases the procedure gives rise to a clear maximum, which is used for further analysis. Note that only a portion of the domain explored during the optimization procedure is displayed here.

where $\hat{\boldsymbol{v}}^i$ is a unit vector perpendicular to the molecular axis $\hat{\boldsymbol{u}}^i$ (see Fig. 1.1(c)). Since $P_{\mathrm{g}}$ cannot distinguish between isotropic and anti-polar order – in both cases $P_{\mathrm{g}} = 0$ –, other order parameters are needed to characterize an anti-polar state. In the modulated-nematic phase [introduced in Sec. 2.5 and in Fig. 2.10(c) and discussed in detail in Sec. 5.5], molecules form arches, where the orientation of the molecules' central segments – and thus also the polar vector $\hat{\boldsymbol{v}}$ (see Fig. 1.1(c)) – are periodically modulated along one particular spatial direction. To quantifiy this spatial modulation, we introduce its amplitude as an order parameter $\Psi_{\mathrm{m}}$, which we determine in full analogy to the definition of the smectic order parameter $\Lambda_{\mathrm{sm}}$. We define the spatially dependent polarity, $P_1(\boldsymbol{r}) = \sum_{j=1}^{N} e^{i\theta_j}\delta(\boldsymbol{r} - \boldsymbol{r}_j)$, and introduce the absolute value of its Fourier transform

$$\Psi(\hat{\boldsymbol{h}}, \lambda) = \left\langle \frac{1}{N} \left| \sum_{j=1}^{N} e^{i\theta_j} e^{i\boldsymbol{h}\cdot\boldsymbol{r}_j} \right| \right\rangle , \tag{2.83}$$

where $\boldsymbol{h} = (2\pi/\lambda)\hat{\boldsymbol{h}}$ is the wave vector with wavelength $\lambda$ and unit vector $\hat{\boldsymbol{h}}$. Note that because $\theta + \pi/2$ quantifies the orientation of $\hat{\boldsymbol{v}}$, $\Psi$ describes periodic variations in $\hat{\boldsymbol{v}}$. We evaluate $\Psi(\hat{\boldsymbol{h}}, \lambda)$ for different values of $\lambda$ and directions $\hat{\boldsymbol{h}}$ and take the maximum $\Psi_{\mathrm{m}}$ as the order parameter for the modulated-nematic phase. The optimization procedure is illustrated in Fig. 2.12(b).

In order to have additional information on the structural properties of the modulated-nematic phase, we monitor polar correlations along the optimal direction $\hat{\boldsymbol{h}}_{\mathrm{m}}$ using the polar correlation function

$$g_1^{||}(r) = \left\langle \frac{1}{N} \sum_{i=1}^{N} \sum_{j \neq i} \hat{\boldsymbol{v}}^i \cdot \hat{\boldsymbol{v}}^j \delta\Big(r_{ij}^{||} - r\Big) \right\rangle . \tag{2.84}$$

Here, $r_{ij}^{||} = |\boldsymbol{r}_i - \boldsymbol{r}_j| \cdot \hat{\boldsymbol{h}}_{\mathrm{m}}$ is the projection of the vector joining the centers of the $i$-th and $j$-th molecules onto the direction of $\hat{\boldsymbol{h}}_{\mathrm{m}}$. Order parameters and correlation functions defined in this Section are used to map out the complete phase diagram of zig-zag and bow-shaped molecules. The results are presented in Chap. 5.

# Chapter 3

# Photo-Switchable Molecules and Applications

In this Chapter we discuss photo-switchable molecules and we give an overview over their most recent technological applications, with particular focus on a series of experiments performed by Fang *et al.* in 2013. In Sec. 3.1 we introduce the photo-switching molecules and we give an overview of their most appealing technological applications. In Sec. 3.2 we discuss the chemical properties of azobenzene, one of the most important photo-switchable compounds. In Sec. 3.3 the effect of light on the orientation of liquid crystals that contain light-absorbing molecules is reviewed. Finally, in Sec. 3.4 we explain a series of experiments performed by Fang *et al.* [1]. A detailed description of these experiments is important since they strongly inspired the molecular model discussed in Chap. 6.

## 3.1 Introduction to photo-switchable molecules

Photo-switchable molecules are chemical compounds that received much attention in the last years. These molecules can switch between two (or even more) stable states when irradiated by light. When photo-switchable molecules are incorporated into a surrounding media, the conformational changes induced by light at the molecular level can result in a drastic change in the macroscopic properties of the material.

There are different types of photo-switchable compounds. Examples are spiropyrans, azobenzenes, dithienylethenes, and alkenes [161]. Illumination of a photo-switchable molecule with light of a proper wavelength can result in dramatic changes of the molecular properties. In case of light-induced *trans-cis* isomerization, photon absorption leads to a spatial rearrangement of the molecule that eventually affects the surrounding structure. Since the switching mechanism is highly efficient, precisely controllable, and completely reversible, its central role in many advanced applications is not surprising. The research activity in this field is nowadays very vital [32, 162].

Photo-switchable molecules can be used to build simple molecular machines [163], to control the electron transfer in molecular electronic switches [164] or to control the stability of liquid-crystal systems [87]. When incorporated into micelles, light-switches can be used to disaggregate the micellar structure upon illumination [165]. This mechanism has been used to design light-controlled drug-delivery systems [166].

Further interesting applications concern the control of both the structures and the functions of biological systems [167]. There are many fascinating examples: incorporation of light-controlled molecules on the backbone of a protein allows for the precise control

of the folding-unfolding process [168], conjugation of a protein ligand with a photo-active molecule changes the ligand-protein binding properties [169], integration of light-switching molecules in lipid membranes alters the membrane permeability [170], etc.

Another promising direction for exploring how light can be used to control material properties are light-switchable sufactants [171–174]. They accumulate at fluid interfaces. By switching locally between the two isomeric states, the surface tension changes, and its gradient drives Marangoni flow. This moves emulsion droplets along a surface or in bulk with interesting non-linear dynamics [175, 176].

Other technological applications are functionalized surfaces, monolayers covered by photo-switchable molecules. Illumination modifies the monolayer wettability [177], controls the motion of a flat molecular rotary motor [178], the rate of electron transfer between the monolayer surface and its environment [23] or the conductance in a molecular-scale electronic device [179]. It is also possible to inscribe nano-sized patterns on the monolayer by photo-lithography because of a mechanism called surface relief gratings [180, 181].

Very importantly for our purpose, photo-switchable molecules can be embedded in a liquid-crystal host matrix [182] or they can act as mesogens themselves [27, 183]. In both cases, light absorption controls both the phase stability and the alignment of the liquid crystal. Illumination can trigger an isothermal transition between different liquid-crystal phases [87] or reorient the director in the nematic phase [184].

In Chap. 6 we present a molecular model for the relaxation dynamics of orientational order in a monolayer of photo-switchable molecules. Our model is strongly inspired by a series of experiments performed by Fang *et al.* [1]. These experiments demonstrate how, in a self-assembled monolayer of azobenzene-based molecules, orientational order can be precisely controlled by illumination with light. In Sec. 3.2 we summarize the chemical properties of azobenzene and how they couple to light. It will become clear that many fundamental properties of azobenzene can be substantially different depending on the experimental conditions.

## 3.2 Photochemical properties of azobenzene

In the context of liquid crystals, the most widely used photo-switchable molecule certainly is azobenzene [32]. Azobenzene is a molecule composed of two phenyl rings separated by an azo group. It can be found in two configurations, the *trans* and the *cis* isomers, schematically illustrated in Fig. 3.1(a).

The *trans* isomer is nearly planar and rod-like with a nearly absent dipole moment. In the *cis* isomer the two phenyl rings are twisted and out of plane. In the *trans* configuration, the distance between the two ends of the molecule is $\approx$ 0.99nm, while in the *cis* state it reduces to $\approx$ 0.5nm [186]. Consequently, the *cis* isomer acquires a dipole moment of nearly 3 Debye. The free-volume of the *cis* isomer is also larger than that of the *trans* configuration [187].

The transition between the two isomers happens either by thermal excitation or by photon absorption with high efficiency. The quantum yield of the isomerization is close to unity. The *trans* configuration is the lower-energy state of the molecule. Therefore, when azobenzenes are left in the dark (or in typical ambient conditions) nearly all of them are found in the *trans* state.

A fundamental characteristic of the azobenzene is the strong electronic absorption of its $\pi$-bonds system. In the azobenzene molecule, *cis* and *trans* isomers have distinct

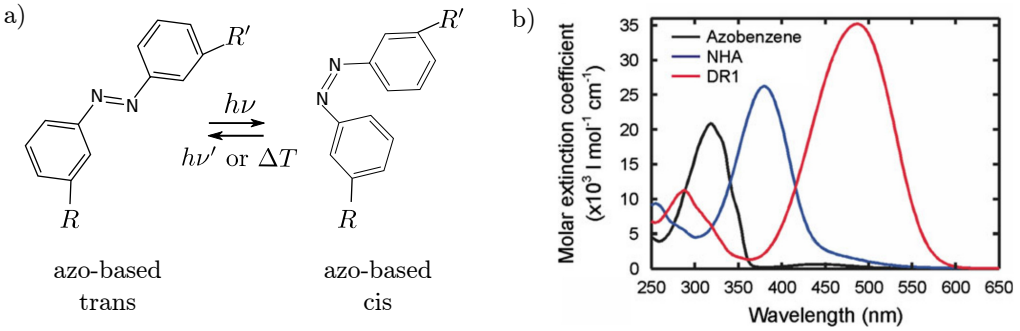


FIGURE 3.1: a) Example of an azobenzene-based photo-switchable molecule in the *trans* (left) and *cis* (right) configuration. The azobenzene molecule (two benzene rings connected by the azo bond) is responsible for the light-switching properties, but other chemical groups can be attached in the positions denoted by $R$ and $R'$. (b) Absorption spectra of *trans* azobenzene in dilute tetrahydrofuran solution. The three curves refer to azobenzenes with different ring-substitution patterns: azobenzene (black), amino-azobenzene (blue) and pseudo-stilbene (red). From [185].

absorption spectra, only weakly overlapping. The absorption spectra can, however, be tuned to lie in a large range of the electromagnetic spectrum by adding proper chemical groups to the phenyl rings (ring substitution patterns, indicated with the letters R and R' in Fig. 3.1(a)) [185]. In Fig. 3.1(b) the absorption spectra of a *trans* azobenzene with different ring substitution patters are shown. Depending on the location of the absorption peak, the azo-based molecules are divided into three fundamental categories: azobenzene, amino-azobenzene and pseudo-stilbene. The absorption spectrum of the *cis* isomers is affected by the substitution patterns as well. Especially in the case of pseudo-stilbene, where the absorption peak is strongly shifted towards the red, the overlap of the *trans* and *cis* absorption spectra can be very significant. Thus, it is possible to excite both the *cis*-to-*trans* and the *trans*-to-*cis* transitions by using light of the same wavelength, and the molecule cycle between *trans* and *cis* configurations.

The ring substitution patterns also strongly influence the average life time of the isomers. In different experimental conditions, the thermal conversion time from *cis* to *trans* can range from milliseconds to hours or even days [185]. Consequently, under illumination a sample containing azobenzene-based molecules is characterized by a relative concentration of the two isomers that is depends on a large variety of factors: light intensity and wavelength, the quantum yield of the isomerization, temperature, the characteristic times of both the light-induced and the spontaneous thermal isomerization as well as the molecular environment.

The isomerization of azobenzene is a complicated process and, indeed, the precise pathway followed by the molecule during the conformational change is still discussed [188]. Wang *et al.* [189] described the isomerization in terms of subsequent transitions between molecular electronic levels, as schematically illustrated in Fig. 3.2. Upon photon absorption, a molecule in the singlet *trans* state $S_0$ is exited to the *trans* state $S_1$, from which it decays to the triplet state $T_1$. From here the molecule can back-isomerize to $S_0$ or reach the exited triplet state of the *cis* isomer $T_1'$. In the latter case, the *trans*-to-*cis* isomerization ($T_1' \rightarrow S_0'$) is completed with much higher probability than the back $T_1' \rightarrow S_0$ transition [189]. A similar, reverse path is followed during *cis*-to-*trans* isomerization. The

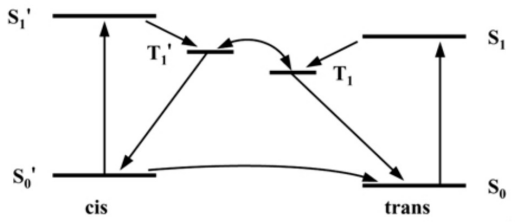


FIGURE 3.2: Diagram of the energetic levels of a pseudo-stilbene molecule. From [190].

energy difference between the *trans* ground state and the *cis* ground state ($S_0$ and $S_0'$ in Fig. 3.2, respectively) is approximately 50kJ/mol [187].

Atomistic molecular dynamics simulations can reconstruct the spatial configuration of the azobenzene at each step of the isomerization [188]. This process is even more complicated in the presence of a solvent, mainly because the transition can be hindered by the surrounding molecules [191]. Either in vacuum or in the presence of a crowded environment, isomerization is an extremely fast process which happens on the time scale of picoseconds [185, 191]. As explained in Sec. 6.1, this remarkably small time scale allows us to model the isomerization of azobenzene as a drastically simplified process: an instantaneous transition in a system which only comprises the *trans* and the *cis* ground states $S_0$ and $S_0'$.

## 3.3 Light-induced orientational order

The phenomenology of the interaction between light and nematic liquid crystals is very rich [192]. The basic effect results from the coupling between the dipole moment of the mesogens and the electric field of the electromagnetic wave, which generates an optical torque. If the intensity of the electromagnetic wave exceeds a threshold value, the torque overcomes elastic and viscous forces and the nematic director rotates and eventually aligns with the electric field. The effect is analogous to the Freedericksz transition [193] induced by a static electric field in nematic liquid crystals (here the director aligns with the field above a certain field strength) and is thus called *optical Freedericksz transition* [192].

In 1990 Janossy *et al.* discovered that by dispersing a small amount of light-absorbing molecules ($\approx 1\%$) in a nematic liquid crystal, the threshold of the optical Freedericksz transition can be reduced by up to three orders of magnitute [194]. The effect was later explained by the interaction between the exited state of the light-absorbing molecules and the nematic liquid crystal host [195–198].

The situation changes if the light-absorbing molecules are also photo-switches, *i.e.*, if they undergo significant conformational changes upon photon absorption. In this case, the molecular alignment results from a process called *angular hole burning*, rather than from a torque [199]. To illustrate the phenomena, we consider the illumination of a liquid crystal entirely made of azo-based molecules by linearly polarized light. In most cases, *trans* isomers act as good mesogens while *cis* isomers do not show relevant mesogenic properties [32, 200].

The probability for a molecule to absorb a photon and isomerize depends on its transition moment, a vector whose direction defines the polarization of the *cis-trans* transition. We assume that the transition moment of the molecule is oriented along the

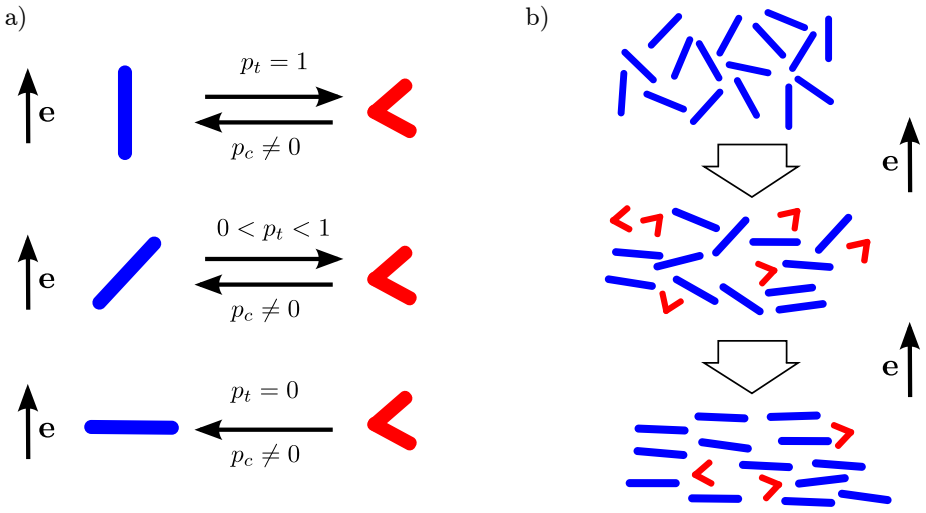


FIGURE 3.3: (a) *Trans* (blue) and *cis* (red) model azo-isomers under illumination with light linearly polarized along **e**. The isomerization probability is proportional to the cosine square of the angle between the light polarization and the transition moment of the molecule (along the main molecular axis). (b) Schematic illustration of the angular hole-burning process. Azo-molecules are in the ground state *trans* configuration at ambient conditions. Under illumination with linearly polarized light, a series of consecutive angular-dependent isomerizations lead to a steady state in which *trans* isomers are oriented perpendicularly to the light polarization.

main molecular axis, defined by the unit vector **s**. When light is polarized along the transition moment, the isomerization probability is maximized. More specifically, the probability for azobenzene to absorb a photon is proportional to the cosine square of the angle between the direction of polarization of light and **s**. Molecules are repeatedly isomerized under illumination, and after isomerization they assume random orientation [201, 202]. The distribution of molecular orientations thus reaches a steady state, wherein the transition moments of the molecules are aligned. The alignment is in the direction along which molecules are less likely to be further isomerized. In this way, the mesogenic *trans* molecules form nematic order perpendicular to the light polarization. The process is illustrated in Fig. 3.3.

In theory, angular hole burning is described by Fokker-Plank equations for the respective molecular orientation distribution functions, $f_t(\mathbf{s},t)$ and $f_c(\mathbf{s},t)$, for the *trans* and *cis* isomers at time $t$ [184]. In the most general case the dynamics reads

$$\frac{\partial f_t(\mathbf{s},t)}{\partial t} + \nabla_{\mathrm{R}}\mathbf{J}_t = -p_t(\mathbf{s})f_t(\mathbf{s},t) + \int d\mathbf{s}' p_c(\mathbf{s}')f_c(\mathbf{s}',t) + \frac{1}{\tau_c}\bar{f}_c(t) \tag{3.1a}$$

$$\frac{\partial f_c(\mathbf{s},t)}{\partial t} + \nabla_{\mathrm{R}}\mathbf{J}_c = -p_c(\mathbf{s})f_c(\mathbf{s},t) + \int d\mathbf{s}' p_t(\mathbf{s}')f_t(\mathbf{s}',t) - \frac{1}{\tau_c}\bar{f}_c(t)\,, \tag{3.1b}$$

where $\nabla_{\mathrm{R}}$ is the the angular part of the usual nabla operator, $\mathbf{J}_t$ and $\mathbf{J}_c$ are rotational currents (defined below), $p_c(\mathbf{s})$ and $p_t(\mathbf{s})$ are the angular-dependent isomerization rates (*cis*-to-*trans* and *trans*-to-*cis*, respectively) and the last terms on the right-hand side account for the *cis*-to-*trans* spontaneous thermal relaxation with characteristic time $\tau_c$. Equations (3.1) must be solved with the normalization condition

$$\int d\mathbf{s} f_\alpha(\mathbf{s},t) = \bar{f}_\alpha(t)\,, \tag{3.2}$$

where we introduced the subscript $\alpha = c, t$ and $\bar{f}_t(t)$ [$\bar{f}_c(t)$] is the fractional population of *trans* [*cis*] isomers at time $t$. Since the total number of molecules is conserved, we have $\bar{f}_c(t) + \bar{f}_t(t) = 1$ at any time.

The isomerization rates are given by

$$p_\alpha(\mathbf{s}) = I\sigma_\alpha(\mathbf{s}\cdot\mathbf{e})^2\,, \tag{3.3}$$

where $I$ is the light intensity, $\sigma_\alpha$ is a molecular parameter (it contains the cross section for photon absorption, the quantum yield of the process, and the dependence on the light wavelength) and $\mathbf{e}$ is a unit vector defining the orientation of the optical electric field. Due to the nearly isotropic shape of *cis* isomers, it is common to assume that $p_c(\mathbf{s})$ is constant, *i.e.*, that the *cis* photon absorption does not depend on the isomer orientation.

The rotational currents are the sum of a diffusion and a drift term

$$\mathbf{J}_\alpha = -D_\alpha\nabla_{\mathrm{R}} f_\alpha(\mathbf{s},t) - \frac{D_\alpha}{k_{\mathrm{B}}T}(\nabla_{\mathrm{R}}U_\alpha)f_\alpha(\mathbf{s},t)\,, \tag{3.4}$$

where the $D_\alpha$ are rotational diffusion constants (in principle different for the *trans* and *cis* isomers) and $U_\alpha$ is the potential describing intermolecular interactions and the potential energy in external fields. In previous studies, the interaction potential is assumed to be of the Maier-Saupe type and the model is studied in mean-field approximation [184, 197].

In the following section we discuss a set of experiments reported by Fang *et al.* in Ref. [1]. The rotational dynamics of the molecules is described using Eqs. (3.1). Furthermore, we discuss the limitation of a mean-field approach and how the dynamical model in Eqs. (3.1) inspired the kinetic Monte Carlo simulations described in Chapter 6.

## 3.4 Light-control of the birefringence relaxation

The recent experiments of Fang *et al.* [1], which have attracted considerable attention, motivated the kinetic Monte Carlo simulations presented in Chapter 6. In this section we summarize the experimental results.

A self-assembled monolayer (SAM) with glasslike properties is realized by covering a glass surface with dye Methyl-Red (dMR) molecules at high in-plane density and tethering them with covalent bonds at random positions [see Fig. 3.4(a)]. The molecules are free to rotate but their translational freedom is constrained to $\approx$ 1nm displacements. In the ground state dMR molecules assume a rod-like *trans* configuration with anisotropic optical properties. The light-induced *cis* configuration has a bent-core shape and is nearly isotropic. Because of the photo-switchable core, isomerization between the two configurations can efficiently be induced by illumination with light at a 514nm wavelength. The absorption spectra of the *cis* and *trans* isomers partially overlap and illumination with light of this wavelength induces both *cis*-to-*trans* and *trans*-to-*cis* transitions.

In Ref. [1] the initial orientation of the molecules in the SAM was random. Under illumination with linearly polarized light (writing process), *trans* molecules form nematic order perpendicular to the light polarization via angular hole-burning [201–203], as illustrated in Fig. 3.4(b). Thus the monolayer exhibits some birefringence $Q(t)$. Since light also induces the reverse, *cis*-to-*trans* transition, in steady state a mixture of both isomers exists at a relative concentration that depends on the light intensity, the density of the monolayer and other factors.

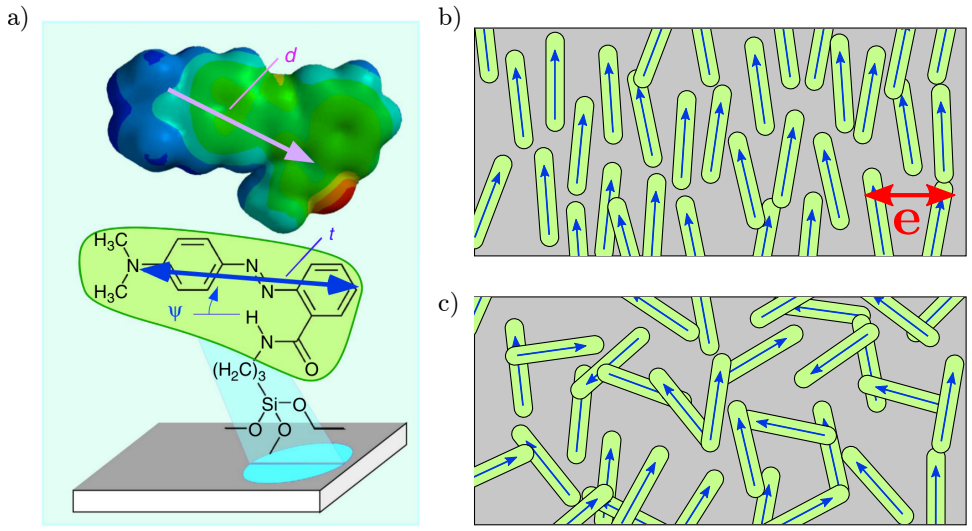


FIGURE 3.4: (a) Dye Methyl-Red molecule tethered to a glass surface via covalent bond. The transition moment **t** (blue arrow) is mainly determined by the orientation of the azo-core and is nearly parallel to the glass surface ($\Psi \approx 25°$). The dipole moment of the dMR, **d**, is given by the pink arrow. From [1]. (b) Arrangement of *trans* molecules after illumination of the monolayer with light linearly polarized along **e**. The isomers are aligned perpendicularly to the light polarization. (c) Isotropic configuration of *trans* molecules after thermal or CP erasure (details in the text). The experimental in-plane density of dMR on the monolayer is higher than in the figures [1]. In order to randomize their orientations, molecules have to pass over each other.

Reference [1] investigated the relaxation of the birefringence under two different illumination conditions following the writing process:
**1)** The SAM is left in the dark, resulting in relaxation driven by thermal fluctuations only (thermal erasure). At room temperature all molecules in the *cis* configuration relax back to the *trans* form after a characteristic time [204]. They assume random orientations and the nematic order is lost.
**2)** The SAM, immediately after the end of the writing process, is illuminated with circularly polarized (CP) light at 514nm, which makes the molecules cycle between the *trans* and *cis* configurations and speeds up the relaxation of the birefringence (CP erasure). A schematic picture of the *trans* isomers in the monolayer after thermal erasure or CP erasure is shown in Fig. 3.4(c).

A schematic of the typical experimental results is given in Fig. 3.5, where the temporal evolution of the birefringence $Q(t)$ is shown for both thermal and CP erasure processes. Fang *et al.* [1] showed that the relaxation of the birefringence is non-exponential, and is instead accurately described by a functional form of the type

$$Q(t) = [1 + (t/\tau_t)]^{-\eta} . \tag{3.5}$$

An asymptotic power-law relaxation starts at $t \approx \tau_t$ and proceeds as $Q(t) \approx (t/\tau_t)^{-\eta}$ for $t > \tau_t$.

Non-exponential relaxations are characteristic of a glassy state, *i.e.*, of systems sampling a rugged free-energy landscape [205–208]. Here, the underlying dynamics does not possess a single characteristic time scale, but rather a distribution of them. It has been suggested [1, 29] that a distribution of energetic barrier that leads to the

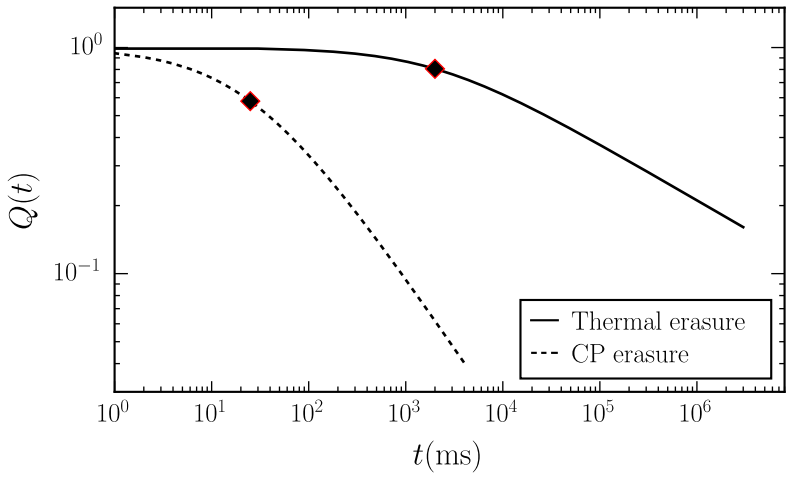


FIGURE 3.5: Schematic representation of the relaxation of the birefringence, $Q(t)$, obtained in the experiment discussed in Ref. [1]. The birefringence inscribed in the monolayer by illuminating it with linearly polarized light can be erased either by thermal fluctuations at room temperature (thermal erasure) or by illumination with circularly polarized light (CP erasure). In both cases the relaxation is well described by the long-time power law decay of Eq. (3.5). Parameters $\tau_t$ are shown as a diamond marker. Other parameters are $\eta = 0.25$ for the thermal erasure curve and $\eta = 0.63$ for the CP erasure curve.

power-law relaxation in the SAM originates from i) the high packing density and ii) the molecular rotations proceeding in discrete jumps as molecules pass each other by stretching or squeezing the covalent bonds which tether them to the surface. We discuss non-exponential relaxation processes more extensively in Sec. 3.4.2.

### 3.4.1 Rotational dynamics

The erasure processes **1)** and **2)** can be modeled by defining a rotational dynamics for the orientational distribution functions of the isomers through the formalism introduced in Sec. 3.3. As the dMR molecules in the *cis* state are nearly isotropic, we assume $p_c(\mathbf{s}) = p_c^{\text{iso}}$. Also, since the transition moment of the molecules is approximately parallel to the glass substrate, we treat the system as purely two-dimensional. The molecular orientation $\mathbf{s}$ in Eqs. (3.1) is thus fully determined by an angle $\theta$. With these conditions, Eqs. (3.1) become

$$\frac{\partial f_t(\theta,t)}{\partial t} + \nabla_{\text{R}}\mathbf{J}_t = -p_t(\theta) f_t(\theta,t) + p_c^{\text{iso}}\bar{f}_c(t) + \frac{1}{\tau_c}\bar{f}_c(t) \tag{3.6a}$$

$$\frac{\partial f_c(\theta,t)}{\partial t} + \nabla_{\text{R}}\mathbf{J}_c = -p_c^{\text{iso}} f_c(\theta,t) + \int_0^{2\pi} d\theta' p_t(\theta') f_t(\theta',t) - \frac{1}{\tau_c}\bar{f}_c(t)\,. \tag{3.6b}$$

We recall that $f_t(\theta,t)$ and $f_c(\theta,t)$ are the orientational distribution functions for *trans* and *cis* isomers, respectively. The light-induced isomerization rates, $p$, and the rotational currents, $\mathbf{J}$, have been defined in Eq. (3.3) and Eq. (3.4), respectively.

During thermal erasure the monolayer is left in the dark, therefore, there are no light-induced isomerizations: $p_c^{\text{iso}} = 0$ and $p_t(\theta) = 0$. Eqs. (3.6) hence become

$$\frac{\partial f_t(\theta,t)}{\partial t} + \nabla_{\text{R}}\mathbf{J}_t = +\frac{1}{\tau_c}\bar{f}_c(t) \tag{3.7a}$$

$$\frac{\partial f_c(\theta,t)}{\partial t} + \nabla_{\text{R}}\mathbf{J}_c = -\frac{1}{\tau_c}\bar{f}_c(t)\,. \tag{3.7b}$$

During CP erasure the isomerization of *trans* isomers is not angular dependent, hence $p_t(\theta) = p_t^{\text{iso}}$. Additionally, the characteristic times of light-induced isomerizations are several orders of magnitude smaller than that of the spontaneous *cis*-to-*trans* thermal relaxation. Therefore, the last terms on the right-hand side of Eqs. (3.6) can be neglected. With these conditions Eqs. (3.6) become

$$\frac{\partial f_t(\theta,t)}{\partial t} + \nabla_{\text{R}}\mathbf{J}_t = -p_t^{\text{iso}} f_t(\theta,t) + p_c^{\text{iso}}\bar{f}_c(t) \tag{3.8a}$$

$$\frac{\partial f_c(\theta,t)}{\partial t} + \nabla_{\text{R}}\mathbf{J}_c = -p_c^{\text{iso}} f_c(\theta,t) + p_t^{\text{iso}}\bar{f}_t(t)\,. \tag{3.8b}$$

In Ref. [1], Eqs. (3.7) and (3.8) are solved numerically in order to obtain the temporal evolution of the orientational distribution functions. Solutions are obtained under the assumption that the rotational diffusion constants of the two isomers are the same, i.e. $D_t = D_c$, and neglecting molecular interactions, *i.e.*, $U_t = U_c = 0$.

In general, the temporal relaxation of birefringence obtained with this procedure is exponential [1]. The experimental power-law decay of $Q(t)$ [as in Eq. (3.5)] can only be reproduced by combining the results of several sets of equations (at least 7) each with different values of the characterizing parameters [1]. We find this procedure quite unsatisfying, as it requires the fine tuning of a large number of free parameters whose values are, ultimately, rather arbitrary. Nevertheless, the analysis suggests a multi-domain structure of the monolayer, with different areas characterized by different relaxation dynamics, which in turn generates the distribution of characteristic times required for the power-law relaxation.

In Chapter 6 we discuss a molecular model inspired by Eqs. (3.7) and (3.8) for the relaxation of the birefringence during both thermal and CP erasure. However, we do not focus on the orientational distribution functions but instead we solve the rotational dynamics for each single molecule in the system using kinetic Monte Carlo simulations. Furthermore, we take into account the molecular conformational changes upon isomerization, the effect of the molecular environment, and the energetic cost for each molecule to overlap with its neighbors by stretching the tethers. With this approach we are able to capture the essential physics of the system and reproduce the experimental results.

### 3.4.2 Non-exponential relaxation processes

A simple relaxation process follows an exponential form $\phi(t) = \exp(-t/\tau)$ (a Maxwell-Debye relaxation) and its dynamics is thus fully characterized by a single time scale $\tau$. In many systems however, the relaxation deviates from a simple exponential and is instead

described by a stretched-exponential $\phi(t) = \exp -(t/\tau)^{\beta}$ with $0 < \beta < 1$ or an asymptotic power-law as in Eq. (3.5) [205, 207, 209].

Non-exponential relaxations were first observed in 1847 by Kohlrausch [210] and have been found in many contexts: in the relaxation of dipole moments in a viscous fluid [211], in the strain recovery of a polymeric glass [212], in the dynamics of supercooled colloidal systems [213], and in the growth of interfaces [214]. Deviations from a Maxwell-Debye relaxation are normally ascribed to heterogeneity in the system structure or dynamics [215].

The underlying idea is that a system is divided into multiple regions. Each region relaxes exponentially with its own characteristic time and the overall non-exponential relaxation results from an average over these different domains. The presence of spatial correlations in the local dynamics, which correspond to transient regions of fast- and slowly-moving molecules, is called *dynamic heterogeneity* [66], a collective feature of glasslike systems especially studied in the context of supercooled liquids [216].

Following this interpretation, Fang *et al.* proposed that the power-law relaxation of the birefringence in Ref. [1] should be considered as an activation process that takes place with a distribution of energetic barriers $f(U)$, which results in a distribution of relaxation times. The birefringence $Q(t)$ is thus defined as

$$Q(t) = \int_0^{\infty} \exp[-t/\tau(U)] f(U)\, dU\,, \tag{3.9}$$

where the relaxation times $\tau(U)$ are governed by the Arrhenius law

$$\tau(U) = \tau_t \exp(U/k_{\mathrm{B}}T)\,, \tag{3.10}$$

and $\tau_t$ is the characteristic time scale of molecular fluctuations. The energy barriers are distributed according to a generalized Gumbel distribution [217]

$$f(U) = \frac{\gamma}{U_m \Gamma(1/\gamma)} \exp\Big[ - U/U_m - \exp(-\gamma(U/U_m))\Big]\,, \tag{3.11}$$

where $U_m$ and $\gamma$ are distribution parameters and $\Gamma$ is the Euler gamma function. Substituting Eq. (3.11) into Eq. (3.9) using Eq. (3.10) gives a power-law decay of $Q(t)$ exactly as in Eq. (3.5). The calculation is detailed in Appendix A.

The Gumbel distribution is one of the only three possible limit distributions for the extremal values of a sequence of properly scaled, identically distributed and independent random variables [217]. There is no fundamental reason for the energy barriers to be distributed according to Eq. (3.11), but a generalized Gumbel distribution is often used in the studies of correlated systems as a convenient fitting function, a procedure that generated speculations about the role of extreme-value statistics in correlated systems [218, 219]. The basic argument is as follows: in highly-correlated systems, there are mesoscopic regions that are not statistically independent and, as a result, spatially averaged quantities do not necessarily satisfy the fundamental assumptions of the central limit theorem. Hence, the related probability distribution functions are not Gaussian [219].

Besides non-exponential relaxation processes, other features such as a subdiffusive regime at intermediate times or a non-Gaussian distribution of single-particle displacements are considered universal signatures of glasslike dynamics [220]. The subdiffusive regime is often related to the presence of low-mobility particles, whose

displacements are hindered by their neighbors [221, 222]. The non-Gaussian distribution of particle displacements is interpreted as a manifestation of heterogeneous dynamics [223]. Indeed, the distribution of particle displacements is expected to be Gaussian in a purely random diffusion process. For example, in a continuous time random walk, the Gaussian distribution of the displacements is essentially a consequence of the central limit theorem, since subsequent steps are assumed to be independent and identically distributed stochastic variables. Hence, deviations from a Gaussian distribution can be ascribed to non-identically distributed or eventually correlated steps. Additionally, heterogeneous dynamics has been connected to a violation of the Stokes-Einstein relation, which predicts a linear dependence of the diffusion coefficient on temperature [222, 224, 225]. In Chapter 6 we demonstrate that universal signatures of glasslike dynamics can be observed in our molecular model in a proper region of the parameters space, where the simulated birefringence relaxes non-exponentially.

The direct observation of dynamic heterogeneity requires the precise resolution of single-molecule motion, which allows to extract information about fluctuations. Furthermore, even if dynamic heterogeneity is a transient phenomena (in non-crystalline structures molecules are constantly moving and rearranging), spatial correlations in the molecular dynamics can last for several time decades, in during which the molecular motion must be tracked. Such challenging measurements have successfully been performed only recently on some colloidal glasses [226–228].

The common route to the direct identification of dynamic heterogeneity in a translationally invariant system at equilibrium is well described in Ref. [65]. It starts with the definition of the molecular mobility $c(\mathbf{r}; t, 0)$, that measures how much a particle, located at position $\mathbf{r}$ at time 0, has moved between time $t$ and time 0. For example, one can define

$$c(\mathbf{r}; t, 0) = \sum_{i=1}^{N} \exp(-|\mathbf{r}_i(t) - \mathbf{r}_i(0)|^2)\delta(\mathbf{r} - \mathbf{r}_i(0)) \,, \tag{3.12}$$

where $N$ is the number of molecules and $\mathbf{r}_i(t)$ is the position of the $i$-th molecule at time $t$. The next step is to define a correlation function, which measures the degree of spatial correlation between molecules with a similar dynamics,

$$G_4(r; t) = \langle c(\mathbf{r}; t, 0)c(\mathbf{0}; t, 0)\rangle - \langle c(\mathbf{r}; t, 0)\rangle^2 \,, \tag{3.13}$$

where $\langle \dots \rangle$ denotes ensemble average and where $r = |\mathbf{r}|$. If the molecule dynamics are spatially correlated at time $t$, the correlation function $G_4(r; t)$ is expected to decay to zero at a certain distance $r_0$, which is an estimate for the size of correlated regions. Thus, the integral of the correlation function also increases with the size of dynamical domains and can be taken as a measure of the extension of dynamic heterogeneity in the system. This integral is defined as

$$\chi_4(t) = \int d\mathbf{r} G_4(r; t) \,, \tag{3.14}$$

and is called dynamical susceptibility because it shows several qualitative analogies with the susceptibility of critical systems.

As mentioned before, the procedure just described works for a system at equilibrium and, hence, cannot be immediately applied to the relaxation of the birefringence $Q(t)$ studied in Ref. [1]. Indeed, the system is out of equilibrium in the course of the relaxation towards an equilibrium state. During this transient regime, it is not possible to perform ensemble averages as in Eq. (3.13). Nevertheless, inspired by the procedure just described,

in Sec. 6.4 we provide a direct measure of the extension of spatio-temporal correlated domains during a relaxation process. In this way we can unambiguously demonstrate the presence of dynamical heterogeneity and their connection with a non-exponential relaxation dynamics.

# Chapter 4

# Numerical Methods

In this Chapter we explain the numerical methods used to solve our molecular models. Monte Carlo simulations are at the base of the studies presented in Chapter 5, where we map out the phase behavior of the bent-needle model. Monte Carlo methods are discussed in Sec. 4.1, with particular attention to implementation of the Monte Carlo technique in the Canonical and in the Isobaric-Isothermal ensemble. In Sec. 4.2 we discuss the specialized optimization techniques used to save computational time. Kinetic Monte Carlo simulations are used to generate the rotational dynamics of the model presented in Chapter 6. Therefore we detail this special kinetic implementation in Sec. 4.3.

## 4.1 Monte Carlo simulation

When a certain molecular model is proposed, it is essential to test it against real experimental data. Because not all the properties of a system are easily accessible in real-life experiments, the main sources of informations are typically averaged quantities. It follows that, in order to test a model, one has to compare the predicted average values of certain observables with the experimental ones. In the context of statistical mechanics, the average value of an observable $O$ is defined in the canonical ensemble as

$$\langle O \rangle = \frac{\int d^N\mathbf{p} d^N\mathbf{q} e^{-\beta\mathcal{H}(\mathbf{q}_1,\ldots,\mathbf{q}_N,\mathbf{p}_1,\ldots,\mathbf{p}_N)} O(\mathbf{q}_1,\ldots,\mathbf{q}_N,\mathbf{p}_1,\ldots,\mathbf{p}_N)}{\int d^N\mathbf{p} d^N\mathbf{q} e^{-\beta\mathcal{H}(\mathbf{q}_1,\ldots,\mathbf{q}_N,\mathbf{p}_1,\ldots,\mathbf{p}_N)}}\,, \tag{4.1}$$

where the $\mathbf{q}_i$ are the particles positions, the $\mathbf{p}_i$ the conjugate momenta, $\beta = 1/k_\mathrm{B}T$, $\mathcal{H}$ is the Hamiltonian of the system and $N$ is the number of particles. As in many cases both the observable $O$ and the potential energy are independent on the conjugate momenta, the kinetic terms in Eq. (4.1) are integrated out and one is left with the configurational part

$$\langle O \rangle = \frac{\int d^N\mathbf{q} e^{-\beta U(\mathbf{q}_1,\ldots,\mathbf{q}_N)} O(\mathbf{q}_1,\ldots,\mathbf{q}_N)}{\int d^N\mathbf{q} e^{-\beta U(\mathbf{q}_1,\ldots,\mathbf{q}_N)}}\,, \tag{4.2}$$

where $U$ is the potential energy, which only depends on the particles coordinates.

On the one hand, Eq. (4.2) can be evaluated analytically only in a few simple cases, therefore is natural to look for numerical methods. On the other hand, standard numerical methods are difficult to apply given the high dimensionality of the problem. For example, one can think of evaluating Eq. (4.2) using quadrature methods over $c$ points on each coordinate axis. In this case, the total number of points would be $c^{dN}$ where $d$ is the dimensionality of the system. Using 100 particles in three dimensions means that the

integral has to be evaluated on $c^{300}$ points, a huge number already for small values of $c$ [229]. Is clear that more sophisticated techniques must be used.

The Monte Carlo method is essentially a technique to evaluate high-dimensional integrals. The main idea behind the Monte Carlo integration is that only a small subset of configurations significantly contribute to the integral in Eq. (4.2). Indeed, Eq. (4.2) can be rewritten as

$$\langle O \rangle = \int d^N \mathbf{q} D(\mathbf{q}_1, \ldots, \mathbf{q}_N) O(\mathbf{q}_1, \ldots, \mathbf{q}_N) \,, \tag{4.3}$$

where

$$D(\mathbf{q}_1, \ldots, \mathbf{q}_N) = \frac{e^{-\beta U(\mathbf{q}_1, \ldots, \mathbf{q}_N)}}{\int d^N \mathbf{q} e^{-\beta U(\mathbf{q}_1, \ldots, \mathbf{q}_N)}} \,, \tag{4.4}$$

is the probability density of finding the system in a configuration specified by $(\mathbf{q}_1, \ldots, \mathbf{q}_N)$. If we are only interested in the relative and not in the absolute probability of finding the system in a particular configuration, we can generate points in the space of configurations with a probability proportional to $D$. In this case there would be no need to evaluate the integral in the denominator of Eq. (4.4).

In practice, the Monte Carlo technique consists in starting with a certain configuration of the system, which we denote with $o$ (old), and comparing it with another trial configuration denoted with $n$ (new). The configuration $n$ will be accepted according to its relative probability with respect to the configuration $o$. The most important condition to impose in defining this sampling process is to ensure that an equilibrium configuration is not destroyed once it is reached. At equilibrium, the probability to leave state $o$ for another state $n$ must be equal to the probability of reaching state $o$ starting from $n$. If we denote with $W(o \to n)$ the probability to go from configuration $o$ to configuration $n$, this condition reads

$$D(o) W(o \to n) = D(n) W(n \to o) \,, \tag{4.5}$$

and is called condition of *detailed balance*.

There exist several forms of $W$ that satisfy Eq. (4.5) [230]. In the following we discuss the *Metropolis* scheme [231]. The probability to go from $o$ to $n$ can be expressed as

$$W(o \to n) = \alpha(o \to n) \gamma(o \to n) \,, \tag{4.6}$$

where $\alpha(o \to n)$ is the probability to generate $n$ starting from $o$ and $\gamma(o \to n)$ is the probability to accept the move from $o$ to $n$. In the Metropolis scheme [231] $\alpha(o \to n)$ is symmetric $[\alpha(o \to n) = \alpha(n \to o)]$, thence Eq. (4.5) becomes

$$\frac{\gamma(o \to n)}{\gamma(n \to o)} = \frac{D(n)}{D(o)} = \exp[-\beta(U(n) - U(o))] \,, \tag{4.7}$$

and a natural choice for $\gamma(o \to n)$ is

$$\gamma(o \to n) = \begin{cases} \dfrac{D(n)}{D(o)} & \text{if} \quad U(n) > U(o) \\ 1 & \text{if} \quad U(n) \leq U(o) \end{cases} . \tag{4.8}$$

Eq. (4.8) means that the trial move from $o$ to $n$ is accepted with probability $\exp[-\beta(U(n) - U(o))] < 1$ if the move brings the system in a configuration with higher

energy than before, or is accepted with certainty if the new configuration has lower energy than the old one.

In practice, the condition given by Eq. (4.8) is implemented in the following way: if $U(n) \leq U(o)$ the new configuration is immediately accepted. If $U(n) > U(o)$, a random number $rand \in [0, 1]$ is extracted from an uniform distribution. The trial move is accepted if $rand < \exp[-\beta(U(n) - U(o))]$ and rejected otherwise.

The average values of interest can be measured after any trial move. One of the basic route to test for the system equilibration is to start the Monte Carlo simulation from several different initial configurations and to keep track of the evolution of the relevant average quantities. When the same averaged quantities (measured in simulations initialized with different initial conditions) converge to a common value, one can assume that an equilibrium state has been reached.

Modern computer technologies typically allow for the simulation of systems with several thousands of molecules, a large number which is nevertheless far from the thermodynamic limit. Thus, to simulate the properties of a system in the bulk, it is common practice to employ periodic boundary conditions, as we do in Chapters 5 and 6. Under periodic boundary conditions, the system is considered as the primitive cell of an infinite periodic structure of identical cells. If the distance of a molecule from the cell border is smaller than the inter-molecular interaction range, the interaction with molecules at the opposite side of the cell must be taken into account. Additionally, when a translational move brings the molecule outside the cell, the molecule will reenter the cell from the opposite side.

In Secs. 4.1.1 and 4.1.2 we explain how the Metropolis scheme is implemented in two typical situations: a canonical or a isothermal-isobaric ensemble.

### 4.1.1 $NVT$ Monte Carlo simulation

In the canonical ensemble a system can only exchange heat with its surrounding. The number of particles $N$, the system volume $V$ and the temperature $T$ are therefore fixed. In order to generate a new configuration of the system from an old one, molecules have to change their positions and, eventually, their orientations. In the following we summarize the implementation of a Metropolis Monte Carlo simulation assuming that we are in two dimensions, where the orientation of a molecule is fully specified by an angle.

The starting configuration of a system is in principle arbitrary but an educated choice can reduce the time needed to reach an equilibrated state. From the starting configuration $(o)$, a molecule is selected at random and translated or rotated with equal probability. Let us denote with $(x_o, y_o)$ the spatial coordinates of a molecule in the starting configuration and let us assume that in this configuration the orientation of the molecule is given by an angle $\theta_o$. The trial move brings the molecule in a new configuration $n$. If a translational move is selected, the new coordinates are obtained via the following substitution

$$\begin{aligned} x_o &\to x_o + \Delta_{\mathrm{T}}\xi_1 \\ y_o &\to y_o + \Delta_{\mathrm{T}}\xi_2 \,, \end{aligned} \tag{4.9}$$

where $\xi_1$ and $\xi_2$ are two random numbers extracted from a uniform distribution between $-0.5$ and $0.5$ and $\Delta_{\mathrm{T}}$ is the maximum translational displacement. If a rotational move is selected, the new orientation is given by

$$\theta_o \to \theta_o + \Delta_{\mathrm{R}}\xi_3 \,, \tag{4.10}$$

where $\xi_3$ is again a random number uniformly distributed between $-0.5$ and $0.5$ and $\Delta_{\rm R}$ is the maximum rotational displacement.

The trial move is then accepted according to Eq. (4.8), *i.e.*, with probability $\gamma(o \to n) = \min[1, \exp[-\beta(U(n) - U(o))]]$, and the whole process is repeated again. A cycle of $N$ independent trial displacements is called a Monte Carlo sweep. It is common practice to evaluate the relevant average quantities at least after a complete Monte Carlo sweep.

The variables $\Delta_{\rm T}$ and $\Delta_{\rm R}$ are in principle arbitrary, but too large displacements will result in most of the new trial configurations being rejected, while too small maximum displacements cannot guarantee a full exploration of the configurational space in a reasonable time. In practice, it is convenient to fix the average acceptance rate of a displacement move to be around 50% of the total attempts, and to adjust the maximum displacement accordingly.

The new position of the molecule can be anywhere (with finite probability) inside a square of lateral size $\Delta_{\rm T}$ centered in $(x_o, y_o)$. Also, the new orientation is defined by an agle that can be anywhere (with finite probability) in the interval $(-\Delta_{\rm R}/2, \Delta_{\rm R}/2)$ around $\theta_o$. The method is therefore clearly ergodic.

### 4.1.2 $NPT$ Monte Carlo simulation

In most experimental situations the control variable is pressure rather than volume of the system. It is therefore convenient to introduce an ensemble, where the fixed thermodynamic parameters are the temperature $T$, the number of molecules $N$, and the pressure $P$. In order to keep the pressure fixed, the volume $V$ must fluctuate. Indeed, a constant pressure system is coupled to an isotropic piston, which expands or compresses in order to keep the internal pressure equal to the external applied pressure. If such a system is also allowed to exchange heat with a surrounding heat bath, then its temperature will also stay constant.

In the isothermal-isobaric ensemble, the partition function of a system is essentially a canonical partition function with an additional volume integration, where a $PV$ term has been added to the Hamiltonian. In two dimensions it reads

$$Q(N,P,T) = \frac{\beta P}{\lambda_{th}^{2N} N!} \int dV V^N e^{(-\beta PV)} \int d^N \mathbf{s}\, e^{(-\beta U(\mathbf{s}_1,\ldots,\mathbf{s}_N;L))}\,, \tag{4.11}$$

where $\lambda_{th}$ is the thermal de Broglie wavelength and we expressed the molecular position in terms of the scaled variables $\mathbf{s}_i = \mathbf{q}_i/L$ ($L = \sqrt{V}$ as the system is assumed to be in a square box) for later convenience, but the presence of $L$ as an argument of $U$ indicates that the interaction energy depends on the real distance between molecules.

In complete analogy with Eq. (4.4), the probability density to find the system in a configuration defined by $(\mathbf{s}_1, \ldots, \mathbf{s}_N)$ and with volume $V$ is

$$D(\mathbf{s}_1, \ldots, \mathbf{s}_N; V) \propto V^N e^{(-\beta PV)} e^{(-\beta U(\mathbf{s}_1,\ldots,\mathbf{s}_N;L))}\,. \tag{4.12}$$

In practice, in the isothermal-isobaric ensemble, a Monte Carlo attempt to change the system volume has to be defined in addition to the moves for the molecular displacements. To ensure that the condition of detailed balance is satisfied, an attempt to change the volume has to be made on average every $N$ trial molecular displacements. Denoting with $V_o$ ($V_n$) the volume of the old (new) configuration $o$ ($n$), the new volume is obtained via

$$V_n = V_o + \Delta_V \xi_V\,, \tag{4.13}$$

where $\Delta_V$ is the maximum volume displacement and $\xi_V$ is a random number uniformly distributed between $-0.5$ and 0.5. Subsequently, the coordinates $(x, y)$ of the center of mass of all the molecules in the system have to be scaled according to

$$\begin{aligned} x &\to x\frac{L_n}{L_o} \\ y &\to y\frac{L_n}{L_o}\,, \end{aligned} \tag{4.14}$$

where $L_n = \sqrt{V_n}$ and $L_o = \sqrt{V_o}$. The energy of the new configuration $U(n)$ is evaluated and the volume move is accepted with probability

$$\gamma(o \to n) = \min[1, \exp\{-\beta[(U(n) - U(o)) + P(V_n - V_o)] + N\ln(\frac{V_n}{V_o})\}]\,. \tag{4.15}$$

Clearly, since after a trial volume change all the inter-molecular interactions must be evaluated again, a volume change is computationally more costly then a molecular displacement.

## 4.2 Optimization techniques

In this Section we explain the numerical optimization techniques used to save computational time in our implementation of the Monte Carlo simulation. In Sec. 4.2.1 we describe a specialized implementation of the basic isotropic Verlet list [229], which takes advantage of the highly anisotropic shape of the bent-needle molecules. In Sec. 4.2.2 we detail a cluster algorithm, which is used to displace a group of several molecules in a single Monte Carlo move in order to efficiently unlock kinetically trapped configurations.

### 4.2.1 Anisotropic neighbor list

If the interactions in the simulated model are pairwise additive and if the interaction range of the molecules is smaller than the simulation box, several techniques can be used to avoid the calculation of all the $N(N-1)/2$ pair interactions after each molecular displacement.

The simplest possibility is to use a linked list. The linked list is built by using a square decomposition of the simulation box. The simulation box is divided into smaller sub-boxes of a side length equal or larger than the intermolecular interaction range $r_\mathrm{I}$. Hence, each molecule only interacts with other molecules in the same sub-box or in the other eight neighboring sub-boxes (in two dimensions).

The Verlet list is another method of reducing the number of pair interactions that must be evaluated after each Monte Carlo trial displacement. In its basic implementation, one introduces a cutoff radius $r_\mathrm{C} = r_\mathrm{S} + r_\mathrm{I}$ (larger than the interaction range), where the distance $r_\mathrm{S}$ is called skin radius [see Fig. 4.1(a)]. A list of all the molecules within a distance $r_\mathrm{C}$ is then built for each molecule. After a trial displacement of a molecule, the interaction energy has to be evaluated only within the molecules that belong to the Verlet list, but the list has to be updated if a translational displacement brings the molecule under consideration at a distance larger than $r_\mathrm{S}$ from its initial position [229]. A large value of $r_\mathrm{s}$ reduces the update frequency of the list, but increases the number of neighboring molecules within the list.

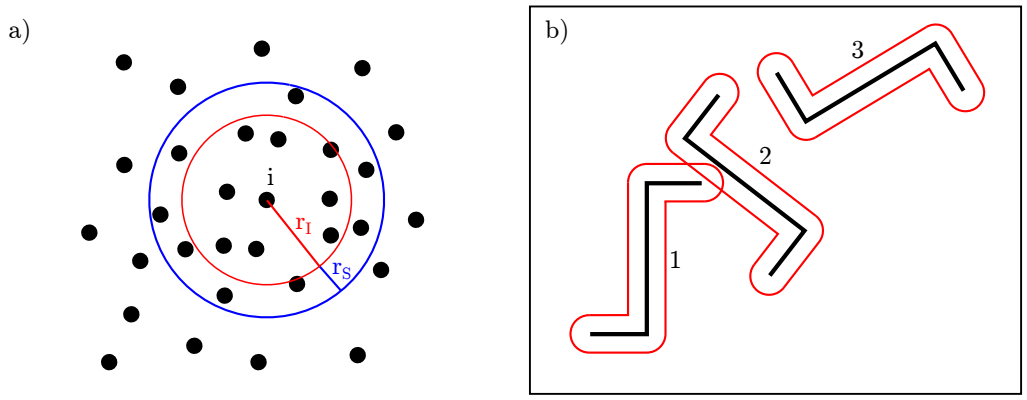


FIGURE 4.1: a) The isotropic Verlet list of particle $i$ contains all the particles that are within a range $r_I + r_s$ from it, where $r_I$ is the particle interaction range and $r_S$ is the skin radius. b) The anisotropic Verlet list for bent hard needles is built by wrapping a bent spherocylinder around each molecule. Molecule $i$ belongs to the Verlet list of molecule $j$ if their spherocylinders overlap. In the figure, molecule 2 is in the Verlet list of molecule 1 (and *vice versa*) while molecule 3 is not.

In our specialized implementation, we rely on the fact that bent needles have anisotropic shape and that they interact through a hard-core potential, which does not allow the needles to overlap. Thus, we use an anisotropic shape to build the list instead of simply checking for radial distances. Our Verlet list is built by wrapping a spherocylinder body around each molecule. This non-trivial shape is obtained by gluing together three spherocylinders, one for each molecular segment. The Verlet list is then filled with the neighboring molecules whose bent spherocylinders overlap with the one under consideration. The bent spherocylinder of a molecule remains fixed for many Monte Carlo steps, but has to be reconstructed when a rotational or a translational Monte Carlo move brings the molecule out of its bent spherocylinder. Shrinking the spherocylinder radius for the Verlet list considerably reduces the time needed to detect potential overlaps, but increases the rate at which the lists need to be updated [229]. Before starting a Monte Carlo simulation, we thus first determine the spherocylinder radius that optimizes algorithmic performance.

Because we use a combination of linked list and Verlet list, the lateral extension of the linked list cells is roughly given by the particle length plus the spherocylinder radius of the Verlet list. The Verlet list in a given sub-box can then be built by only considering molecules within that same sub-box as well as within the eight neighboring sub-boxes.

### 4.2.2 Cluster moves

In Chapter 5 we employ Monte Carlo simulations to map out the phase diagram of the bent hard-needle model, which shows a variety of transitions between liquid-crystal phases. Especially in the vicinity of the isotropic–quasi-nematic transition (see Fig. 2.6), small clusters of very close and well aligned molecules develop in the isotropic phase. Once these relatively small but highly packed clusters of particles form, molecule orientations can get kinetically locked. Equilibration, however, requires overcoming the high free-energy barriers associated with aligning these clusters, which considerably slows down equilibration. A way to alleviate this problem is to rely on the fact that Monte Carlo simulations need not be tied to a local and thus physical dynamics. Instead of moving

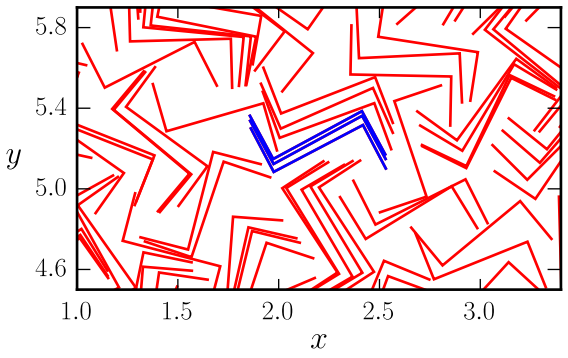


FIGURE 4.2: Example of a cluster (blue colored molecules) for zig-zag molecules with $a = 0.25$ and $\alpha = \pi/2$. The parameters of the artificial potential in Eq. (4.16) are $\epsilon = 1.0$, $\Delta r_{\max} = 0.3$ and $\Delta\theta_{\max} = 6.0°$. To ease the identification of the cluster, we only show a portion of the simulation box. The system density, in units of the molecular length, is $\rho = 14$, thus the system is in the vicinity of the isotropic–quasi-nematic transition (see the phase diagram in Fig. 5.9(a)).

particles one at a time, one can define collective moves that identify groups of correlated particles and then move them as a single object [232, 233]. However, in order to satisfy detailed balance and ensure that reverse displacements are also possible, the operation must be done in a probabilistic way.

Here, we build clusters of particles by introducing an artificial attractive potential $u_f(\epsilon_{ij})$ that links particles together [234, 235]. The potential form is arbitrary, but is most successful if it captures the nature of correlations within a cluster. Our choice is

$$u_f(\epsilon_{ij}) = -\epsilon \mathrm{H}(\Delta\theta_{\max} - \Delta\theta_{ij})\mathrm{H}(\Delta r_{\max} - \Delta r_{ij})\,, \tag{4.16}$$

where H is the Heaviside step function, and $\Delta r_{\max}$ and $\Delta\theta_{\max}$ are tunable thresholds. Typical values are $\epsilon = 1.0$, $\Delta r_{\max} = 0.3$ and $\Delta\theta_{\max} = 6.0°$. For a given configuration, the linking probability between particles $i$ and $j$ is

$$p_{ij} = \max[0, 1 - \exp(\beta u_f(\epsilon_{ij}))]\,. \tag{4.17}$$

Molecules that are close and well aligned are thus linked with high probability, whereas molecules outside the range of $\Delta r_{\max}$ and $\Delta\theta_{\max}$ are not linked at all. A cluster is built by choosing a particle $i$ at random and by attempting to build links with its neighbors. If a link between $i$ and $j$ is formed, $j$ becomes a member of the cluster formed around molecule $i$. An example of a cluster built with this procedure for zig-zag molecules in the vicinity of the isotropic–quasi-nematic transition is shown in Fig. 4.2.

Once the cluster has been formed, we perform a trial move by translating or by rotating it around its center of mass. If the trial move generates overlaps, it is immediately rejected. If not, it is accepted with probability

$$W(\text{old} \to \text{new}) = \min[1, \exp(\beta(U_{\text{new}} - U_{\text{old}}))]\,, \tag{4.18}$$

where $U_\nu = \sum_{i,j\in I_\nu} u_f(\epsilon_{ij})$ is the artificial interaction energy between the cluster and its environment in either the $\nu$ =old or new state. The interface $I_\nu$ is defined by all the particles $i$ inside and the particles $j$ outside the cluster that contribute to $U_\nu$. As for standard Monte Carlo simulations, the results are valited by checking that different

initial conditions for both constant-$NVT$ and constant-$NPT$ simulations give the same outcome.

## 4.3 Kinetic Monte Carlo simulation

In the previous Sections of this Chapter we described the Monte Carlo technique as a method for solving high-dimensional integral through a random walk in the space of configurations. In this regard, the Monte Carlo evolution of a system is completely unrelated to its physical time evolution. In this section we explain how, by employing some special precautions, a reliable dynamics can be obtained using a Monte Carlo simulation scheme. This numerical technique is called kinetic Monte Carlo simulation [64, 236].

In general, the kinetic Monte Carlo simulation is a numerical technique well suited to study phenomena, whose dynamics lies on a time scale several order of magnitude larger than the time scale of atomic vibrations, but for which microscopic details are still essential. For instance, typical molecular dynamic simulations (which incorporate detailed inter-atomic potentials) cannot span time scales larger than microseconds and cannot track the dynamics of a statistically significant ensemble of interacting molecules. In kinetic Monte Carlo simulations atomic details are course-grained, which enables the exploration of the long-time collective behavior of complex systems.

In the kinetic Monte Carlo method, each simulated process is associated with a certain rate, which defines the average frequency of occurrence of the process in a sequence of random transitions. Clearly, unphysical moves like the cluster moves described in Sec. 4.2.2 must be avoided. Also, an event should almost always be realized after any Monte Carlo move, which means that the acceptance rates of the moves must be very close to 1. As the probability of accepting a Monte Carlo move is in general inversely proportional to the related maximum displacement, very small displacements should be used, which also make the moves local.

Most importantly, a unique Monte Carlo time scale must be defined independently from the acceptance rate of the Monte Carlo moves. This unique time scale defines the time unit to which the rates of different processes can be compared. To understand how this time scale is introduced, we follow the discussion in Ref. [237].

Let us assume that we are simulating a system with $m$ degrees of freedom. In a Monte Carlo move a particle is displaced from its initial position by an amount included in the interval $[-\delta_i, \delta_i]$, where $\delta_i$ is the maximum displacement for the $i$-th degree of freedom ($i = 1, \ldots, m$). If the probability of accepting a move $A$ is independent from the maximum displacement (*i.e.* for an infinitely dilute system or if we only consider small maximum displacements), the probability density of a successful move is $p = A/2\delta_i$. The mean square displacement of the variable $x_i$ associated with the $i$-th degree of freedom is thus given by

$$\langle x_i^2 \rangle = \int_{-\delta_i}^{\delta_i} p x_i^2 \, dx_i = \frac{A(\delta_i)^2}{3} \,. \tag{4.19}$$

If the Monte Carlo moves are statistically independent, one has

$$\delta_i^2 = 2 D_i dt \,, \tag{4.20}$$

where $D_i$ is the self-diffusion constant for the $i$-th degree of freedom and $dt$ is a Monte Carlo time scale. Substituting Eq. (4.20) into Eq. (4.19) gives

$$\langle x_i^2 \rangle = \frac{2AD_i\,dt}{3}\,, \tag{4.21}$$

which establishes a direct connection between the kinetic Monte Carlo simulation and the diffusivity in Einstein's theory of Brownian motion.

In a Brownian dynamics simulation one has

$$\langle x_i^2 \rangle = 2D_i t_{\mathrm{BD}}\,, \tag{4.22}$$

where $t_{\mathrm{BD}}$ is the Brownian dynamics time unit. Substituting Eq. (4.22) into Eq. (4.21) gives

$$t_{\mathrm{BD}} = \frac{A\,dt}{3}\,. \tag{4.23}$$

Eq. (4.23) means that it is possible to simulate the same process in several kinetic Monte Carlo simulations using different values of $dt$. The resulting time dependent quantities collapse in a single master curve when $dt$ is scaled with the corresponding $A$, which demonstrates the existence of a unique Monte Carlo time scale [237] equal to the Brownian dynamics time scale.

Kinetic Monte Carlo simulations have been used in several contexts: in liquid crystals [238, 239], in glass-forming systems [240, 241], to study the nucleation rate in a suspension of hard spheres [242], the mobility of rods in a quasicrystalline potential [48], the transport dynamics of polymers [243], the formation of vesicles [244], the growth of crystals [245], and the dynamics of thin film deposition [246, 247]. In Sec. 6.2 we detail our implementation of the kinetic Monte Carlo simulation scheme for a molecular model of the experiments described in Sec. 3.4. The results of the simulation are discussed in Chapter 6.

# Chapter 5

# Phase Behavior of the Bent Hard-Needle Model

In this Chapter we study the two-dimensional phase behavior of the bent-needle model introduced in Fig. 1.1(c) using Monte Carlo simulation. The model has two configurations, a chiral zig-zag shape and an achiral bow-shaped shape, which show significant differences in their self-assembly properties. In Chapter 2 we already anticipated the mesophases identified in this model, described their qualitative features, and showed their structures through snapshots of the simulation box. Here, the complete phase diagram of the bent-needle model is obtained by using the order parameters and the correlation functions defined in Sec. 2.7. The mesophases identified in the model are summarized in Fig. 5.1. We find that zig-zag molecules assemble in a quasi-nematic and a smectic-C phase [(Fig. 5.1(a)], while bow-shaped molecules assemble in a quasi-nematic, an anti-ferromorphic smectic-A, and a modulated-nematic phase [Fig. 5.1(b)].

The Chapter is structured as follow. In Sec. 5.1 we detail the model and in Sec. 5.2 we specify the numerical simulation scheme. In Secs. 5.3 and 5.4 we identify the isotropic–quasi-nematic and the quasi-nematic–smectic transition densities, respectively. In Sec. 5.5 the modulated-nematic phase of bow-shaped needles is described in detail. Finally, in Sec. 5.6 we present the complete phase diagram of the bent hard-needle model.

This Chapter is essentially based on the material in Ref. [A].

## 5.1 Bent hard-needle model

Our bent hard-needle model consists of a central line segment of length $b$ to which two terminal line segments of equal length $a$ are attached at a fixed angle $\alpha$ [Fig. 1.1(c)]. The molecules can adopt a chiral zig-zag or an achiral bow-shape configuration, depending on whether $\alpha$ is defined on the same or on opposite sides of the central segment. Note, however, that we only consider enantiomerically pure systems in order to avoid chiral segregation [248]. Pairs of molecules interact via a hard-core exclusion potential but are infinitely thin, i.e., they can be infinitely close to one another but cannot overlap. Since the hard-core interaction potential is athermal, we set to unity the product of Boltzmann's constant and temperature, $k_{\mathrm{B}}T = 1/\beta = 1$, without loss of generality. The total length of the molecule, $L = 2a + b = 1$, is used as the unit of length, also without loss of generality. Each model is thus completely determined by two parameters: $a$ and $\alpha$. In the following we let $\alpha$ vary from 0 to $\pi/2$ (at $\alpha = 0$ both models are equivalent), but we fix $a = 0.25$ for zig-zag molecules and $a = 0.35$ for bow-shaped molecules. This choice maximizes

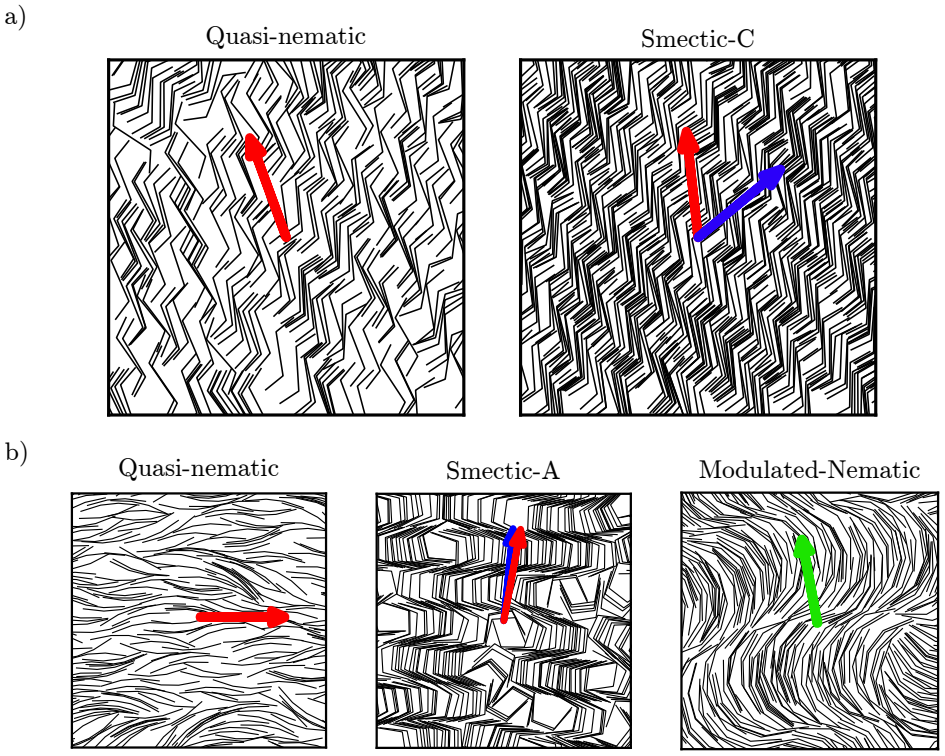


FIGURE 5.1: Snapshots of the main mesophases identified in Monte Carlo simulations: (a) zig-zag molecules with $a = 0.25$, $\alpha = \pi/3$ in both the quasi-nematic ($\rho = 14$) and the smectic ($\rho = 30$) phases, and (b) bow-shaped molecules with $a = 0.35$, $\alpha = \pi/16$, $\rho = 20$ in the quasi-nematic, with $a = 0.35$, $\alpha = \pi/3$, $\rho = 30$ in the smectic, and with $a = 0.35$, $\alpha = \pi/6$, $\rho = 26$ in the modulated-nematic phases. The nematic director, the smectic surface normal and the modulated-nematic layers normal are indicated as red, blue, and green arrows, respectively. Note that in order to clearly illustrate the mesophase morphology, only a portion of the simulation box is displayed.

the excluded area, and thus pushes down the isotropic–mesophase transition densities, making them computationally less costly to study.

## 5.2 Details of the Monte Carlo simulation

In order to study the phase behavior of the zig-zag and bow-shaped models, we perform Monte Carlo simulations mostly in the constant-$NVT$ but also in the constant-$NPT$ ensemble. The Monte Carlo simulation scheme in the constant volume and constant pressure ensemble has been introduced in Sec. 4.1. In this section we detail our implementation for the bent hard-needle model. Most simulations have $N = 2000$ in a square box of area $V$ under periodic boundary conditions.

Constant-$NVT$ simulations are performed at fixed reduced density $\rho = N/V$ and consist of up to $3.0 \times 10^7$ sweeps, where a Monte Carlo sweep comprises $N$ independent trial displacements. The basic Monte Carlo move in the $NVT$ ensemble consists of either translating or rotating (randomly chosen with equal probability) a randomly chosen molecule. The maximum attempted displacement is preliminarily adjusted in such a way that an acceptance rate of approximately 50% is achieved, but during the production runs the maximum step sizes are fixed – dynamical adjustments would violate detailed balance

[249]. The hard-core nature of the pair interaction simplifies the Metropolis acceptance rule in Eq. (4.8): the displacement of a molecule is accepted if it does not generate an overlap, and is rejected otherwise. In order to check that the sampled configurations correspond to equilibrium (and not metastable) states, different initial configurations – including isotropic, perfect polar and anti-polar nematic, as well as perfect smectic states – are used. Note that reaching equilibrium and properly sampling states sometimes require up to several million Monte Carlo sweeps, leading to computational times of up to four weeks on a single-thread of an Intel Xeon X5550 machine with a 2.66 GHz CPU. The minimum simulation time was about one week.

Constant-$NPT$ simulations also include changes in $V$ in order to keep the system pressure $P$ constant (see Sec. 4.1.2). A Monte Carlo sweep then comprises an average of $N$ independent single-molecule trial displacements and one trial volume change. In a trial volume change, $V$ is modified by an amount $\Delta \ln V$ and all the molecule positions are rescaled accordingly. Since we perform the random walk in $\ln V$ rather than in $V$ (the former is known to be computationally more efficient [229]), the acceptance probability of a trial volume change given by Eq. 4.15 must be slightly modified. If no overlap occurs in the resulting configuration, the move is accepted with probability

$$p(V \to V + \Delta V) = \exp[-P\Delta V + (N+1)\ln(1 + \Delta V/V)], \tag{5.1}$$

and is rejected otherwise (note the $(N+1)$ prefactor of the ln term).

For the bow-shaped molecules with intermediate $\alpha$, constant-$NVT$ simulations either result in ferromorphic or in anti-ferromorphic states, depending on the initial configuration. In order to identify the equilibrium ground state, we thus also performed a slow pressure annealing. This process was achieved through a sequence of constant-$NPT$ simulations starting from the isotropic regime and increasing $P$ in steps of 10-20%. At each step $\rho$ was equilibrated for at least $2.0 \times 10^6$ sweeps. The reverse procedure was used to check for hysteresis. This study revealed that the anti-ferromorphic phase is the equilibrium state, as we discuss in Sec. 5.5.

The optimization techniques described in Sec. 4.2 are employed to save computational time. In particular, we use both the anisotropic neighbor list and the cluster algorithm introduced in Sec. 4.2.2 in constant-$NVT$ simulations. In constant-$NPT$ simulations we only use a linked list because each volume change forces the anisotropic neighbor list to be updated, which is a computationally expensive procedure.

## 5.3 Isotropic–quasi-nematic transition

Upon increasing density, both zig-zag and bow-shaped molecules form a quasi-nematic phase with quasi-long-range orientational order. As per the discussion in Sec. 2.3, the quasi-nematic phase and the isotropic–quasi-nematic phase transition via disclination unbinding are evidenced by the transition from an exponential decay of $g_2(r)$ at low $\rho$ to a power-law decay, $g_2(r) \propto r^{-\eta}$, as $\rho$ increases (see Fig. 5.2). From Eq. (2.46) follows that the quasi-nematic phase is expected to be stable against spontaneous disclination unbinding when $\pi K/(8k_BT) > 1$. We obtain the Frank elastic constants from the relation $\eta = 2k_{\mathrm{B}}T/\pi K$, where the power-law decay of $g_2(r)$ is obtained from a linear fit of $\ln g_2(r)$ versus $\ln r$ over the range $0.5 \leq r \leq 4.0$. Note that the lower threshold is necessary because $g_2(r)$ deviates from the power law at small $r$, while the higher threshold is chosen so as to exclude correlations resulting from the use of periodic boundary conditions. Note

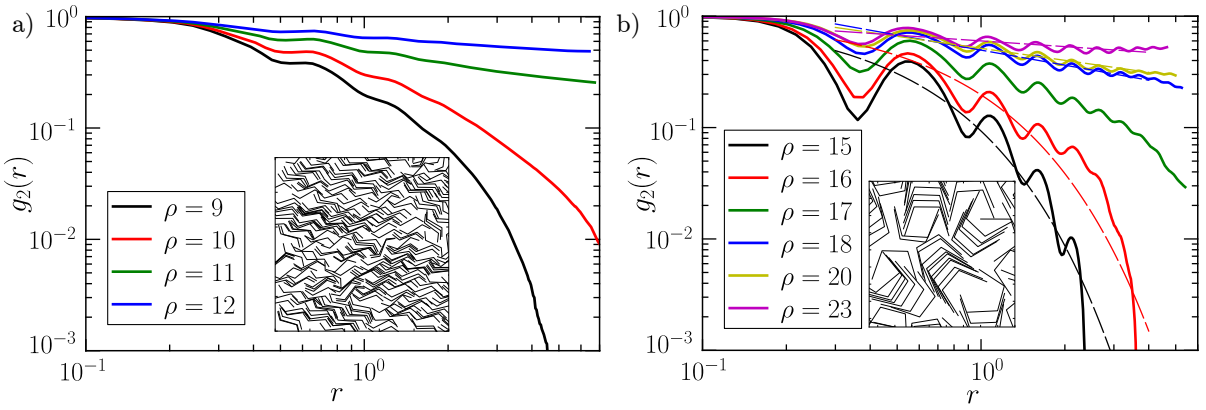


FIGURE 5.2: (a) Radial dependence of the orientational correlation function for several densities for (a) zig-zag molecules with $\alpha = \pi/3$ and $a = 0.25$, and (b) bow-shaped molecules with $\alpha = 2\pi/5$ and $a = 0.35$. Dashed lines in (b) show the fits to an exponential function for $\rho = 15$ and 16 and to $g_2(r) \propto r^{-\eta}$ for $\rho = 18$, 20, and 23. Fit exponents are given in Fig. 5.3. The inset in (a) shows a portion of the simulation box at $\rho = 11$, close to the isotropic–quasi-nematic transition. The inset in (b) details the local packing of molecules, which results in oscillations of $g_2(r)$.

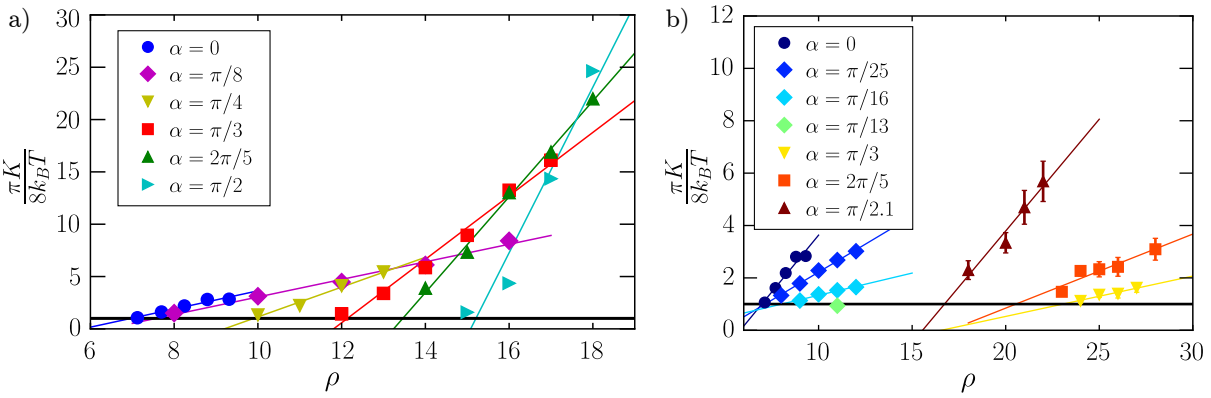


FIGURE 5.3: Density evolution of the reduced Frank elastic constant $K$ obtained from the power-law decay of $g_2(r)$ for (a) zig-zag molecules with $a = 0.25$ and (b) bow-shaped molecules with $a = 0.35$. The isotropic–quasi-nematic transition densities, $\rho_{\mathrm{IN}}$ are obtained from the intersections of the linear fits to the numerical results with the line $\pi K/8k_{\mathrm{B}}T = 1$. For each point, error bars are obtained by propagating the standard errors of the power-law exponents $\eta$ obtained from the least squares fits of $g_2(r)$. Where not shown, error bars are smaller than the symbols.

also that bow-shaped molecules display correlation functions with fairly large oscillations as a result of the local packing structures, which do not exist for straight needles [see inset in Fig. 5.2(b)].

The results for the reduced Frank elastic constant $\pi K/(8k_BT)$ are plotted in Fig. 5.3 for both molecule types. Since the results scale nearly linearly with $\rho$, we identify the isotropic–quasi-nematic transition densities $\rho_{\mathrm{IN}}$ as the intersection between linear fits to data the points and $\pi K_c/(8k_BT) = 1$, as explained in Sec. 2.3.2.

For zig-zag molecules, the quasi-nematic phase is systematically destabilized by bending the terminal segments [Fig. 5.3(a)]. As the central-to-tail angle $\alpha$ increases,

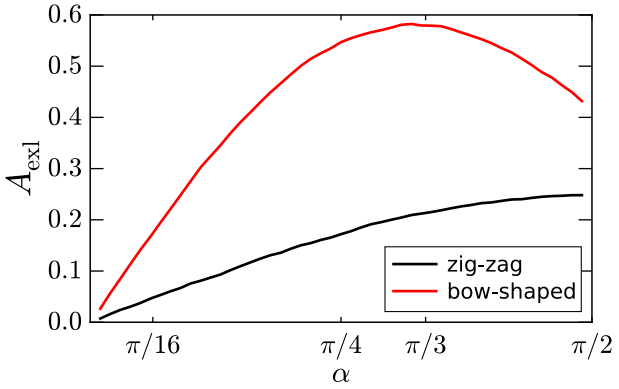


FIGURE 5.4: Excluded area versus central-to-tail angle $\alpha$ for parallel zig-zag (black line) and bow-shaped (red line) molecules.

the transition is thus pushed to higher densities. Bow-shaped molecules, however, show a non-monotonic trend of the transition density $\rho_{\rm IN}$ with $\alpha$ [Fig. 5.3(b)]. For small $\alpha$ the transition density increases with $\alpha$, while for $\alpha \geq \pi/3$ the trend is inverted. In the range $\pi/13 \lesssim \alpha \lesssim \pi/3$ the quasi-nematic phase is unstable with respect to the modulated-nematic phase, and the power-law scaling analysis is then inapplicable (see Secs. 5.5 and 5.6).

We try to understand the difference in the two molecular geometries by examining the size $A_{\rm excl}$ of the excluded area for perfectly parallel molecules (see Fig. 5.4). Like $\rho_{\rm IN}$, it monotonically increases with $\alpha$ for zig-zag molecules, but reaches a maximum at $\alpha \approx \pi/3$ and then decreases for bow-shaped molecules. Large values of $A_{\rm excl}$ suggest that parallel molecules have to pack locally to come close to one another, as evidenced by the undulations of $g_2(r)$ in Fig. 5.2(b). This packing constraints translational freedom, and thus reduces the translational contribution to the entropy. Because the translational contribution normally compensates for the loss of orientational freedom in the nematic phase, higher $\rho$ than usual are needed for this effect to be significant, and as a result $\rho_{\rm IN}$ increases.

## 5.4 Quasi-nematic–smectic transition

Smectic order consists of a periodic arrangement of particle positions along one direction, which leads to a well-defined density wave along the corresponding wave vector. Within smectic layers, however, translational order is absent. In Sec. 2.4.2 we discussed how long-range translational order is not expected in the thermodynamic limit of two-dimensional systems. Nevertheless, smectic order is obervable on sufficiently small length scales. For now, we consider the smectic order parameter defined in Eq. (2.81) as a function of density for both the zig-zag and bow-shaped molecules in Fig. 5.5. The Monte Carlo simulation data are fitted with

$$f(\rho) = 1/2 + \arctan[h(\rho - \rho_{\rm NS})]/\pi, \tag{5.2}$$

where $\rho_{\rm NS}$ and $h$ are fit parameters. Hence, the quasi-nematic–smectic transition density $\rho_{\rm NS}$ is defined as the point of maximum slope of $f(\rho)$. The smectic order parameter for bow-shaped molecules does not assume large values even at the highest densities

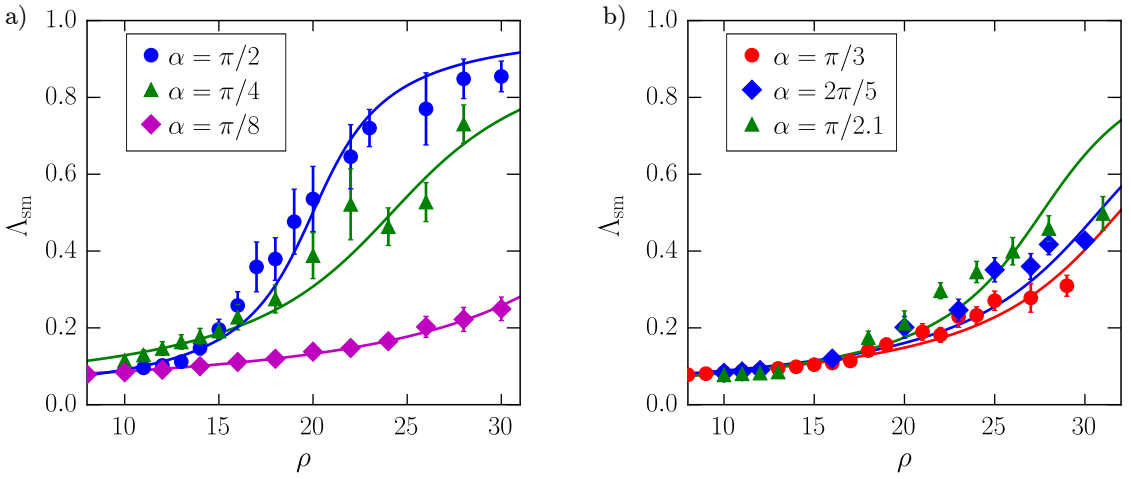


FIGURE 5.5: Smectic order parameter $\Lambda_{\rm sm}$ plotted versus density $\rho$ at several central-to-tail angles $\alpha$ for (a) zig-zag molecules with $a = 0.25$ and (b) bow-shaped molecules with $a = 0.35$. Data points are obtained from Monte Carlo simulations. Error bars indicate the standard deviations of $\Lambda_{\rm sm}$ over equilibrated samples. Lines are a fit of Eq. (5.2) to the data using the transition density $\rho_{\rm NS}$ and $h$ as fitting parameters (see phase diagrams of Fig. 5.9 for results on $\rho_{\rm NS}$).

simulated, which is likely the result of out-of-layer fluctuations and of the instability of two-dimensional smectic order described. Fits to the simulation results nonetheless provide an estimate for $\rho_{\rm NS}$. Note that the values of the transition densities identified in this way are close to the highest values of the densities explored in our simulation.

As could be seen in Figs. 2.8(b) and 5.1(a) and as was previously noted in Ref. [51], zig-zag molecules form a smectic-C phase, wherein the nematic director is tilted with respect to the layer normal. Bow-shaped molecules instead arrange in an anti-ferromorphic smectic-A structure [see Figs. 2.9 and 5.1(b)], wherein the polar vector $\hat{\boldsymbol{v}}$ adopts an opposite orientation in adjacent layers. This unusual ordering can be rationalized by extending a packing argument developed for the anti-ferroelectric ordering of V-shaped molecules [53, 250], i.e., for $b = 0$ [251]. Because the excluded area of two molecules is smaller in the anti-parallel ($\hat{\boldsymbol{v}}^{(i)} = -\hat{\boldsymbol{v}}^{(j)}$) than in the parallel ($\hat{\boldsymbol{v}}^{(i)} = \hat{\boldsymbol{v}}^{(j)}$) arrangement, the former is entropically favored. Molecules can also more easily penetrate into neighboring layers in the anti-ferromorphic smectic phase than in the ferromorphic smectic phase. This effect enhances out-of-layer fluctuations and thus entropically favors anti-ferromorphic smectic ordering as well. This behavior is similar to that of three-dimensional bent-core molecules [156].

No significant smectic ordering is found for values of $\alpha$ smaller than those given in Figs. 5.5(a) and (b). For zig-zag molecules at even smaller $\alpha$, we extrapolate the quasi-nematic–smectic transition to take place at $\rho_{\rm NS}$ that are inaccessible within a reasonable computational time; for bow-shaped molecules, however, the existence of a smectic phase at $\alpha < \pi/3$, even for large $\rho$, is unclear.

As already discussed in Sec. 2.4.2, two-dimensional long-range smectic order should not be thermodynamically stable. One expects instead the scenario illustrated in Fig. 2.8(a). At a given $\rho$, dislocations destroy translational order on length scales larger than the mean distance between thermally induced dislocations, but correlations in the layer orientations persist and exhibit a long-range algebraic decay. Although this

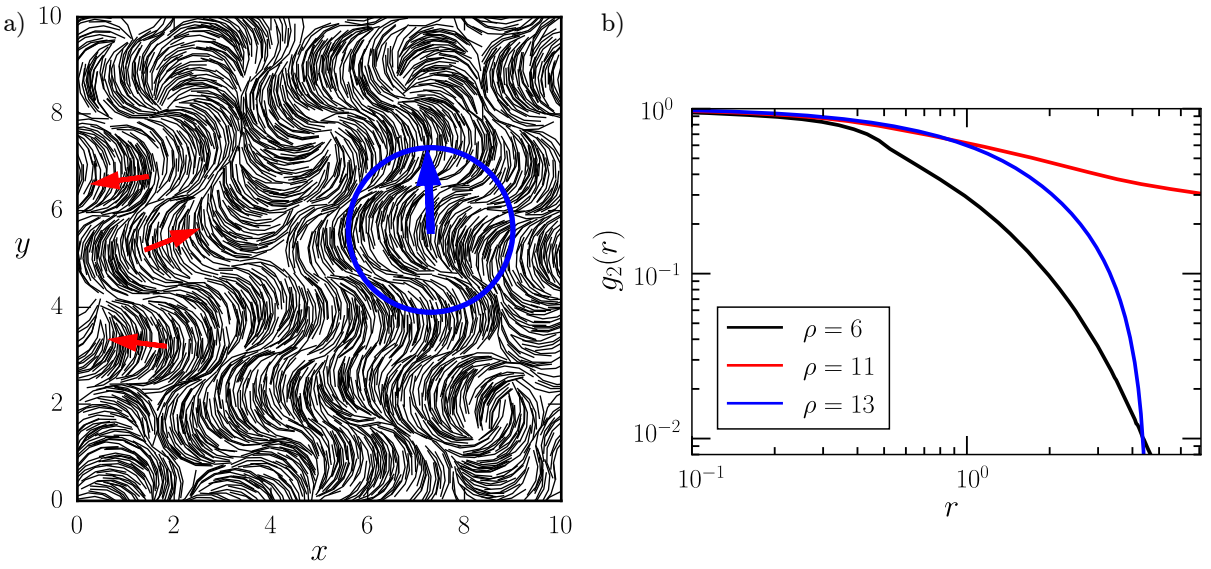


FIGURE 5.6: (a) Snapshot of bow-shaped molecules in the modulated-nematic phase for $\alpha = \pi/8$, $a = 0.35$, and $\rho = 20$. The complete simulation box with $N = 2000$ molecules is shown. The red arrows indicate the polar vector $\hat{\boldsymbol{v}}$ perpendicular to the molecular orientation in the center of the layers. The blue arrow indicates the direction of the optimal wave vector $\boldsymbol{h}_m$. The radius of the blue circle is half the optimal wavelength $\lambda_m$ as defined in Eq. (2.83) and obtained from the maximization procedure illustrated in Fig. 2.12(b). For this configuration $\Psi_{\mathrm{m}} \approx 0.25$. (b) The orientational correlation function $g_2(r)$ for bow-shaped molecules with $\alpha = \pi/13$ decays exponentially at $\rho = 6$, algebraically at $\rho = 11$, and exponentially again at $\rho = 13$ due to the appearance of the modulated-nematic phase.

scenario is physically reasonable and may explain the weak smectic ordering of bow-shaped molecules, we were unable to test it against our simulation data because of the limited range of computationally accessible $N$. Instead, we find smectic order to be fully stabilized in our simulations.

## 5.5 Modulated-nematic phase

Although at small $\alpha$ and for $\alpha \gtrsim \pi/3$ bow-shaped molecules form a quasi-nematic phase [Fig. 2.6(d)], for intermediate $\alpha$, they also equilibrate in a *modulated-nematic* phase, which we introduced in Sec. 2.5. In this phase no overall orientational or positional order exists [Fig. 5.6(a)]. Instead, it shows a different kind of supramolecular arrangement, wherein the orientation of a series of molecules varies gradually along arches that form approximate half-circles, and these arches themselves form layers. Periodic order exists along the layer normal but the mean polar vector $\langle\hat{\boldsymbol{v}}\rangle$ in one layer is antiparallel to that of a neighboring layer (see Fig. 1.1(b) for the definition of $\boldsymbol{v}$). This arrangement destabilizes the quasi-nematic phase and its algebraic orientational order. As shown in Fig. 5.6(b), the occurrence of the modulated-nematic phase can even result in a reentrant exponential decay of $g_2(r)$ with increasing $\rho$. For $\pi/13 \lesssim \alpha \lesssim \pi/3$, however, we found no evidence for a power-law decay of $g_2(r)$ in the whole range of explored densities. A direct transition from the isotropic to modulated-nematic phase occurs instead.

In Fig. 5.7(a) the modulated-nematic order parameter $\Psi_{\mathrm{m}}$ defined in Eq. (2.83) is shown as a function of density for several values of $\alpha$. In analogy with the treatment

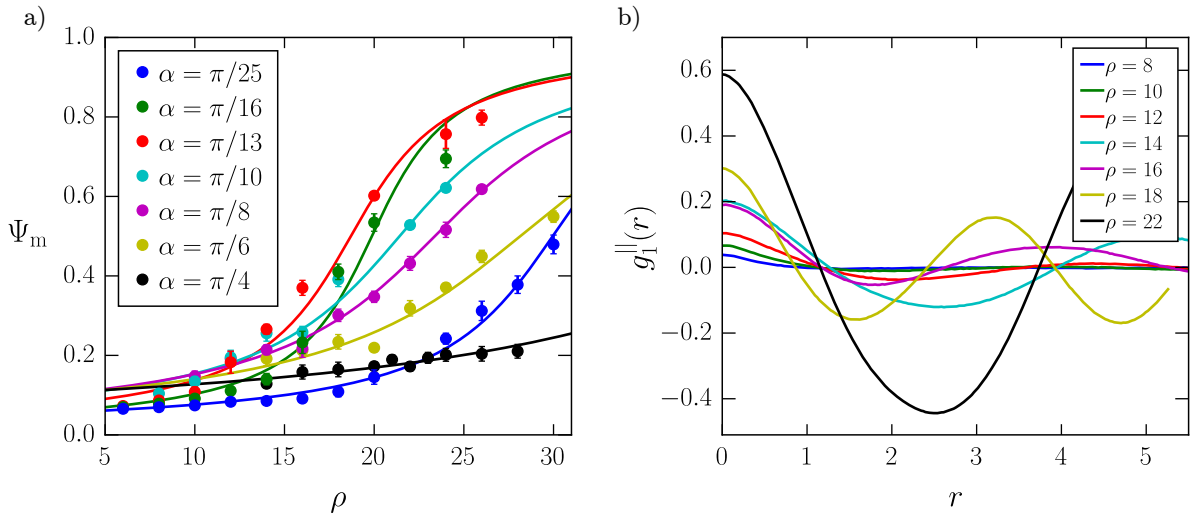


FIGURE 5.7: (a) Modulated-nematic order parameter $\Psi_m$ plotted versus $\rho$ for bow-shaped molecules at several values of $\alpha$. The Monte Carlo simulation results are fitted with Eq. (5.3). Error bars give the standard deviation of $\Psi_m$ over equilibrated samples. From the fit we obtain $\rho_m = 29.95$, 19.97, 18.71, 21.42, 23.38, and 45.57 for $\alpha = \pi/25$, $\pi/16$, $\pi/13$, $\pi/10$, $\pi/8$, $\pi/6$, and $\pi/4$, respectively. (b) Polar correlation function $g_1^{||}(r)$ for $\alpha = \pi/10$ and several values of $\rho$. As density increases, the amplitude of the modulation of $g_1^{||}(r)$ increases, which we take to be a signature of the modulated-nematic phase.

for the identification of smectic order in Sec. 5.4, we fit $\Psi_m$ (as obtained from the Monte Carlo simulation data) with a trial function similar to Eq. (5.2),

$$f(\rho) = 1/2 + \arctan[l(\rho - \rho_m)]/\pi \tag{5.3}$$

where $l$ and $\rho_m$ are fit parameters. In order to clarify the structural properties of the modulated-nematic phase, we consider the polar correlation function $g_1^{||}(r)$ as defined in Eq. (2.84). Because of the periodic modulation in the molecular polar vector $\hat{\boldsymbol{v}}$ along the layer normal, $g_1^{||}(r)$ becomes a periodic function when the layered structure is well established. In particular, since molecules in adjacent layers have opposite polarization, $g_1^{||}(r)$ shows a minimum at a distance corresponding to the layer thickness followed by a maximum, which results from correlations with the next-nearest-neighbor layer. In Fig. 5.7(b) we show $g_1^{||}(r)$ for $\alpha = \pi/10$ and several values of $\rho$. As expected, the periodic modulation of $g_1^{||}(r)$ becomes stronger with increasing density, indicating the progressive development of layers. This behavior is also observed for all other values of $\alpha$.

Our Monte Carlo data show that modulations in $g_1^{||}(r)$ are already present at relatively small $\rho$, whereas the order parameter $\Psi_m$ has not yet increased much. For instance, for $\alpha = \pi/10$ it can be seen in Fig. 5.7(b) that $g_1^{||}(r)$ is already weakly modulated at $\rho = 14$, while the corresponding order parameter is only $\Psi_m \approx 0.2$. Similarly, we find $\Psi_m \approx 0.25$ for the configuration shown in Fig. 5.6(a), even though a remarkable degree of layering is already clearly established. In other words, the layered structure of the modulated-nematic phase is established continuously, which makes it difficult to clearly define a transition density. For this reason, we approximate the transition density $\bar{\rho}_m$ into the modulated-nematic phase by using a threshold, $\Psi_m = 0.2$, on the order parameter. The

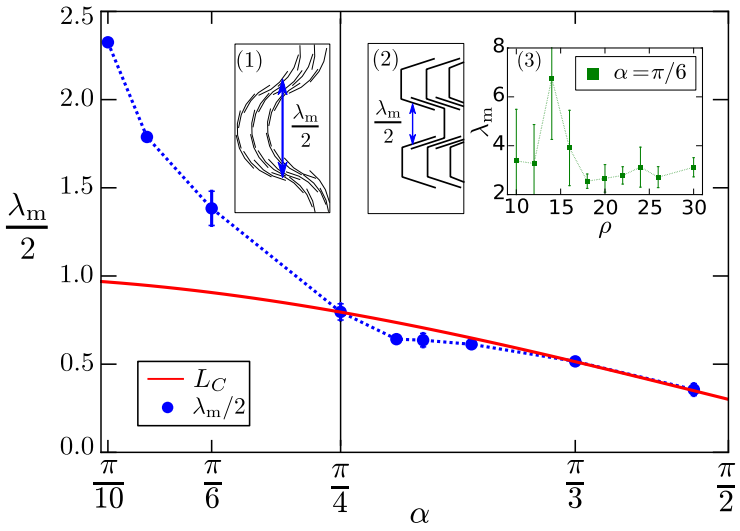


FIGURE 5.8: Distance between two adjacent layers, $\lambda_m/2$, plotted versus $\alpha$ (points). The results for $\lambda_m$ are obtained at $\rho > \bar{\rho}_m$, but are observed to be fairly insensitive to changes in $\rho$ [inset (3)]. Error bars give the standard deviation. The continuous red line is the projected length of the molecule onto a direction along the central molecular segment. The vertical line at $\alpha = \pi/4$ approximately divides the plot in two regions. The first region with $\alpha < \pi/4$ has $\lambda/2 > L_C$ and molecules are arranged in the supra-molecular structure of the modulated-nematic phase illustrated in inset (1). The second region with $\alpha > \pi/4$ has $\lambda/2 \lesssim L_C$, where molecules locally arrange with anti-ferromorphic order with adjacent layers slightly inter-penetrated, as illustrated in inset (2). The dotted line is a guide to the eyes.

same threshold is used for all $\alpha$. This value is such that $\bar{\rho}_m$ matches reasonably well the density at which we observe the reentrant exponential decay of $g_2(r)$ at $\alpha \lesssim \pi/13$, and is then used for all other $\alpha$.

The maximization procedure illustrated in Fig. 2.12(b) for determining the order parameter $\Psi_m$ also provides the typical distance between two layers in the modulated-nematic phase, *i.e.*, $\lambda_m/2$ defined in Eq. (2.83). In Fig. 5.8 we show how this distance evolves with $\alpha$ and compare it with the projected length of the molecule along the direction parallel to the central molecular segment, $L_C = b + 2a\cos(\alpha)$. At small $\alpha$, $\lambda_m > L_C$, which captures the supra-molecular structure of the modulated nematic phase. As $\alpha$ increases, however, $\lambda_m$ decreases and becomes comparable to $L_C$ at $\alpha \approx \pi/4$. Now, molecules locally arrange in anti-ferromorphic order [see inset (2) of Fig. 5.8] which is favored over the supra-molecular ordering of the modulated-nematic phase. For $\alpha > \pi/4$ the layering distance becomes smaller than $L_C$, indicating that adjacent anti-ferromorphic layers inter-penetrate slightly on average, as discussed in Sec. 5.4.

As discussed in Sec. 2.5, the occurrence of a three-dimensional, spontaneously formed, modulated-nematic phase for banana-shaped mesogens and of the two-dimensional modulated-nematic phase for bow-shaped molecules, likely results from "pathological elasticity" [57], which has been predicted to be a consequence of the molecular curvature radius. Our results thus indicate that there is an upper limit for the molecular curvature, corresponding in our model to $\alpha \approx \pi/4$, beyond which the supra-molecular structure of the modulated-nematic phase becomes unstable with respect to the anti-ferromorphic order. The modulated-nematic phase identified here differs from the bent nematic phase formed by V-shaped molecules [53, 250] because the latter does not present a fully

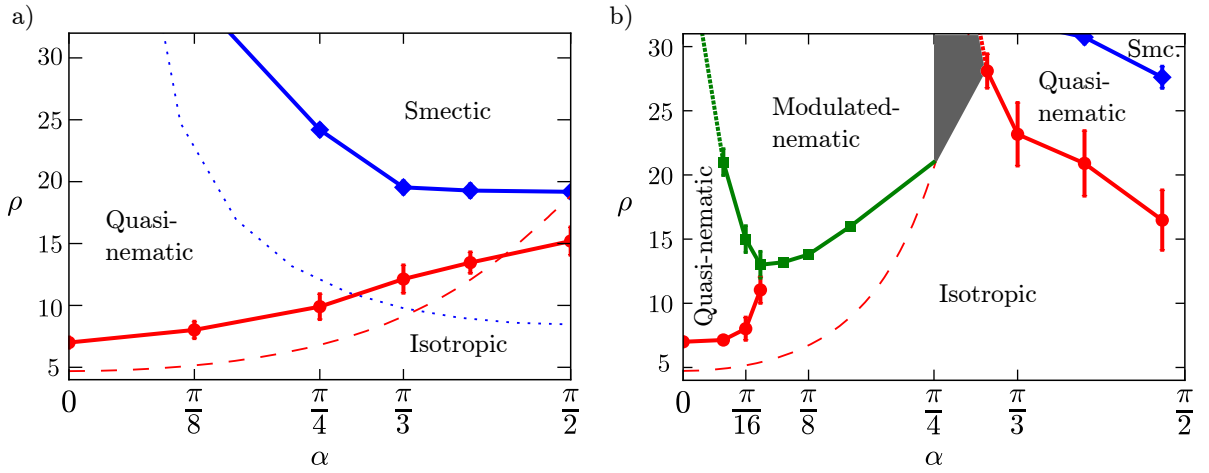


FIGURE 5.9: Phase diagram for (a) zig-zag molecules with $a = 0.25$ and (b) bow-shaped molecules with $a = 0.35$. Points represent the isotropic–quasi-nematic transition densities (circles), quasi-nematic–smectic transition densities (diamonds) and the quasi-nematic– or isotropic–modulated-nematic transition (squares) as identified from the procedures described in Secs. 5.3, 5.4, and 5.5, respectively. For the diamond and square symbols, error bars are estimated by propagating the standard errors of the fit parameters in Eqs. (5.2) and (5.3), respectively. For the circular symbols, error bars are determined by propagating the standard errors of the linear fit functions shown in Fig. 5.3. The gray area in (b) marks the transition between modulated-nematic and quasi-nematic phases in a region where none of the identified mesophases is found to be stabilized. Continuous lines are guides to the eyes. Where not shown, error bars are smaller than the marker size. Dashed and dotted lines represent, respectively, the isotropic–nematic and the nematic–smectic transition lines predicted by Onsager theory (Sec. 2.6).

developed periodicity. Most likely, this difference is geometrical in origin, and may be due to the missing central molecular segment in the V-shaped molecules.

We already discussed in Sect. 2.4.2 that long-range order in two-dimensional smectics is unstable. In Fig. 5.6(a) in the center a dislocation in the layering of the supramolecular arches is visible. This might be an indication that, in analogy to two-dimensional smectics, the layered structure is destabilized by the proliferation of dislocations in sufficiently large systems.

## 5.6 Phase diagram

In Fig. 5.9 we show the simulated phase diagrams for both the zig-zag and the bow-shaped molecules obtained using the approaches described in Secs. 5.3, 5.4, and 5.5. The dashed red and dotted blue lines show the predictions from Onsager theory for the transition densities $\rho_{\mathrm{IN}}$ and $\rho_{\mathrm{NS}}$, respectively. These lines are obtained following the procedure discussed in Sec. 2.6.

According to the phase diagram in Fig. 5.9(a), terminal segments of zig-zag particles destabilize the quasi-nematic phase but stabilize the smectic phase. This qualitative trend is captured by Onsager theory. Our simulation results are in rough agreement with previous studies[51, 63] but also exhibit some significant discrepancies. In particular, in our phase diagram both the isotropic–quasi-nematic and the quasi-nematic–smectic transitions appear at higher $\rho$ (Fig. 5.9(a)). In addition, for $\alpha \approx \pi/2$, the isotropic and

smectic phases are well separated by the quasi-nematic phase, while the latter was not observed at all in previous studies. Most likely, the lower transition densities reported in Refs. [51, 63] follow from using the nematic order parameter for detecting the isotropic–quasi-nematic transition and from considering relatively small system sizes. As already mentioned, the nematic order parameter in a quasi-nematic phase decreases with system size [61].

Bow-shaped molecules exhibit a remarkably rich behavior.
**(1)** For small $\alpha$, the low-density behavior is similar to that of zig-zag molecules. The transition density $\rho_{\mathrm{IN}}$ (red circles) increases with increasing $\alpha$ and is underestimated by Onsager theory. Quasi-nematic order in this small-$\alpha$ region is also destabilized by further increasing the packing density. Instead of the emergence of a smectic phase, however, a modulated-nematic phase takes precedence. We did not specifically explore the phase behavior of bow-shaped molecules with $\alpha < \pi/25$, but we expect the modulated-nematic phase to appear at ever higher densities as $\alpha$ decreases, as indicated by the dotted green line. For symmetry reasons the bent-nematic phase cannot exist for $\alpha = 0$.
**(2)** For $\pi/13 \lesssim \alpha \lesssim \pi/4$, both the quasi-nematic and the smectic orders are destabilized by the modulated-nematic phase at all $\rho$ explored. The direct isotropic–modulated-nematic transition appears at increasing densities with $\alpha$. This phase is simply not captured by Onsager theory as formulated in Sect. 2.6.
**(3)** For $\pi/4 \lesssim \alpha \lesssim \pi/3$, which is indicated in the phase diagram as a gray area, we find no clear evidence for any of the mesophases known to be formed by bow-shaped molecules. In this region the distance between two adjacent layers approaches the projection of the total molecular length along the molecular central segment, resulting in a strong competition between the formation of supra-molecular layers and anti-ferromorphic domains. The investigation of configurations at densities much higher than the ones we could reach would be necessary to clarify what mesophase, if any, is stable in that system.
**(4)** For $\pi/3 \lesssim \alpha < \pi/2$, the molecular curvature is too large to induce a spontaneous bending of the nematic director and the corresponding layer formation. Quasi-nematic order then becomes stable again, but this time the transition densities decrease with increasing $\alpha$. The isotropic–quasi-nematic transition is highly overestimated by Onsager theory. The theory strongly relies on the excluded area, as discussed in Sec. 2.6, but the excluded area of bow-shaped molecules is minimal in the anti-parallel configuration. In our simulations we instead observe clusters of molecules packed in parallel. Because this arrangement involves structural correlations between more than two molecules, it is not surprising that Onsager theory, which only takes into account two-particle correlations dramatically fails. Since many-particles correlation are also present in the modulated-nematic phase, we did not include the splay-bend deformation [53, 250] in our Onsager theory calculation.

Note that we did not study molecules with $\alpha = \pi/2$. With this central-to-tail angle parallel molecules cannot anymore be shifted into each other to form closely packed clusters. A different phase is thus expected. Indeed, tetradic order has been observed in related models [53].

## 5.7 Summary

Chiral zig-zag molecules assume quasi-nematic and smectic phases, depending on density and the central-to-tail angle $\alpha$. We use the orientational correlation function $g_2(r)$ in Eq. (2.80), which decays exponentially in the isotropic phase and algebraically in the

orientationally ordered phase, to identify the isotropic–quasi-nematic transition. In two-dimensional systems with short-ranged interactions, one expects the transition to take place via disclination unbinding [118]. Indeed, apart from packing effects, the correlation functions described in Sec. 5.3 behave similarly to the ones already reported in other two-dimensional anisotropic models with hard-core interactions [42, 60–62].

For zig-zag molecules the isotropic–nematic transition density $\rho_{\mathrm{IN}}$ increases with increasing central-to-tail angle $\alpha$, while the nematic–smectic transition, $\rho_{\mathrm{NS}}$, exhibits the opposite trend. Such behavior is qualitatively captured by Onsager theory although both $\rho_{\mathrm{IN}}$ and $\rho_{\mathrm{NS}}$ are underestimated by the theory, as discussed in Sec. 2.6. Furthermore, we observe a smectic C phase, where the central segment of the zig-zag molecule is tilted against the layer normal. The clear formation of smectic layers, however, indicates that our systems are too small to observe the dislocation unbinding scenario predicted in Ref. [149].

Achiral bow-shaped molecules have a much richer phase behavior. It can be divided into three regions, depending on the value of $\alpha$. For small $\alpha$ molecules form isotropic, quasi-nematic, and modulated-nematic phases, as density increases. The isotropic–quasi-nematic transition is defect driven, which makes the orientational correlation function switch from an exponential to power-law decay with increasing density. No polar order is found in the quasi-nematic phase. Further increasing density destabilizes the orientational order of the quasi-nematic phase.

A modulated-nematic phase then takes over, wherein bow-shaped molecules form layers of supramolecular arches. The orientational correlation function $g_2(r)$ shows a reentrant exponential decay that corresponds to the development of the supramolecular arches. At intermediate $\alpha$, a direct transition from the isotropic to the modulated-nematic phase takes place. The modulated-nematic structure becomes less pronounced with increasing $\alpha$, *i.e.*, the layer thickness decreases towards the molecule length, up to the point where the formation of supramolecular arches becomes unfavored and anti-ferromorphic domains develop instead. For $\alpha \gtrsim \pi/3$, the curvature radius of the molecules becomes too small to induce spontaneous bending of the nematic director and quasi-nematic order reenters. Anti-ferromorphic smectic order is then found at even higher density.

# Chapter 6

# Birefringence Relaxation of Photo-Switchable Molecules on a Surface

In this Chapter we discuss a molecular model, which we developed to capture the essential physics behind a series of experiments involving photo-switchable molecules. The experiments are described in Ref. [1] and have been discussed extensively in Sec. 3.4. They can be summarized as follows. Photo-switchable molecules are tethered to a monolayer at high in-plane density. Orientational order is induced in the monolayer via illumination with linearly polarized light (writing process). Linearly polarized light generates *trans*-to-*cis* and *cis*-to-*trans* isomerizations, therefore both isomers are found at the end of the writing process, when the anisotropic *trans* molecules are aligned perpendicularly to the light polarization and the monolayer shows some birefringence. Subsequently, orientational order is erased either by leaving the monolayer in the dark (thermal erasure) or by illuminating it with circularly polarized light (CP erasure), which induces *trans*-*cis* isomerization cycles. During these processes, the birefringence decays toward zero following a power law (typical for glasslike systems), but during CP erasure the relaxation is remarkably faster than during thermal erasure. A schematic illustration of the essential experimental results is given in Fig. 3.5.

The Chapter is structured as follows. In Sec. 6.1 we introduce the molecular model. In Sec. 6.2 we discuss how the model dynamics is generated using a kinetic Monte Carlo algorithm. In Sec. 6.3 we explain how the monolayer birefringence is obtained during the numerical simulation and how we discriminate between different functional forms for its relaxation dynamics. In Sec. 6.4 we discuss a simplified version of the model, in which only *trans* molecules are present. In this way we can demonstrate that the power-law relaxation of the birefringence can be traced to the formation of dynamic heterogeneity. In Sec. 6.5 we introduce *trans* and *cis* isomers and we model the thermal and CP erasure processes, inspired by the formalism presented in Sec. 3.4.1. The presence of both the isomeric species allows us to study the influence of the isomerization process on the development of dynamic heterogeneity and, thus, on the dynamics of the relaxation.

This Chapter is essentially based on the material in Ref. [B].

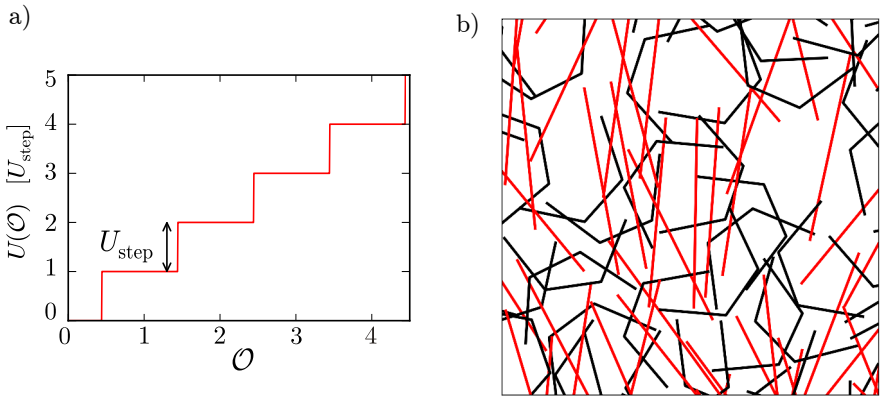


FIGURE 6.1: (a) The step-potential $U(\mathcal{O})$ gives the energy of a molecular configuration as a function of the number of overlaps $\mathcal{O}$ that a molecule forms with its neighbors. All the steps have a fixed height $U_{\rm step}$. (b) A small fraction of a typical initial configuration of the kinetic Monte Carlo simulation showing *cis* (black) and *trans* (red) model molecules attached to a two-dimensional surface.

## 6.1 Molecular model

As explained in Sec. 3.4, when the monolayer of tethered molecules studied in Ref. [1] is illuminated by light, molecules cycle between an anisotropic, rod-like *trans* configuration and a nearly isotropic, bent-like *cis* configuration [see Fig. 1.1(a)]. We model the *trans* isomer as an infinitely thin, straight needle of unit length $L = 1$ and the *cis* isomer as a bent, infinitely thin needle also of total length $L$ [see Fig. 1.1(b)]. In the *cis* configuration we fix the angle between the central and the tail segments to $\alpha = \pi/3$, while each tail segment has a length of $a = 0.35L$ (both $\alpha$ and $a$ are defined as for the bow-shaped needle in Fig. 1.1(c)). The total number of *trans* ($N_t$) and *cis* ($N_c$) molecules is fixed, i.e., $N_{\rm t} + N_{\rm c} = N$. Since the transition moment of the dMR molecules, to which the light polarization couples, is nearly parallel to the monolayer surface, we consider the system to be purely two-dimensional. To mimic the effect of the covalent tethering, molecules are allowed to rotate within the plane but cannot translate.

In our model, the complicated isomerization process of the azobenzene (described in Sec. 3.2) is drastically simplified: it consists of a simple switch from the straight to the bent needle and vice-versa. Also, we assume that the conformational change happens instantaneously, a reasonable assumption given the relative time scales involved. The relaxation of the birefringence happens at least on the second scale (see Fig. 3.5), while the isomerization occurs on the picosecond scale even in relatively dense organic solvents [191].

In order to incorporate isomerization as described in Sec. 3.4 in the kinetic Monte Carlo simulation, we define the following set of rules:
**1) thermal erasure**: only the *cis* $\rightarrow$ *trans* spontaneous transition is allowed and isomerization occurs with probability $P_{\rm th}(c \rightarrow t)$.
**2) CP erasure**: illumination with circularly polarized light induces *trans*-*cis* isomerization cycles. As explained in Sec. 3.3, the isomerization rate is proportional to the light intensity, the quantum yield of the transition process, and the absorption cross sections of the isomers [197, 252]. To limit the number of free parameters, we incorporate all these factors in the two isomerization probabilities $P_{\rm CP}(t \rightarrow c)$ and $P_{\rm CP}(c \rightarrow t)$ for

*trans*-to-*cis* and *cis*-to-*trans* isomerization, respectively. When birefrigence has relaxed towards zero, a steady state is reached, where the numbers of *cis* and *trans* isomers fulfill $N_c P_{\mathrm{CP}}(c \to t) = N_t P_{\mathrm{CP}}(t \to c)$. Hence, the ratio

$$R = \frac{P_{\mathrm{CP}}(t \to c)}{P_{\mathrm{CP}}(c \to t)} = \frac{N_c}{N_t}\,. \tag{6.1}$$

is an essential parameter of our model. Previous measurements show that the absorbance of the two isomers is very similar at 514 nm, therefore $R$ should be in the order of unity [204]. Because light-induced isomerization cycles occur at a much faster rate than the spontaneous *cis-trans* relaxation, the latter is neglected during CP erasure. Importantly, we assume that after an isomerization event, the orientation of the molecule is chosen at random [202, 253].

As anticipated in Sec. 3.4, because of the high in-plane packing density of the SAM, molecules must overlap during the relaxation process in order to become randomly oriented. Following again a minimal approach, and because we restricted molecular motion to a plane, we allow the molecules to overlap by introducing a simple interaction potential $U(\mathcal{O}) = U_{\mathrm{step}}\mathcal{O}$, which is proportional to the number of overlaps $\mathcal{O}$ and the energetic cost $U_{\mathrm{step}}$ of each overlap, which sets the unit of energy. We clarify below how $U(\mathcal{O})$ affects the rotational dynamics of our model molecules.

## 6.2 Details of kinetic Monte Carlo simulations

In Sec. 3.4.1 we showed how the rotational dynamics of the dMR molecules tethered to the monolayer can be explained in terms of the temporal evolution of the orientational distribution functions for *cis* and *trans* isomers through Eqs. (3.7) and (3.8), a set of Fokker-Plank equations with source terms. We discussed how this approach gives an exponential relaxation of the monolayer birefringence unless the results from several sets of equations are averaged together, a procedure that suggests a multi-domain structure of the monolayer. Our approach is radically different because we generate the rotational dynamics for each single molecule in the system (taking into account molecular interactions and the molecular conformational change upon isomerization) using a kinetic Monte Carlo algorithm [64].

The kinetic Monte Carlo simulation method has been introduced in Sec. 4.3, were we discussed how the random walk in the space of configurations, performed in a standard Monte Carlo simulation, can give rise to a reliable dynamics when only local moves are considered and upon introducing an unique Monte Carlo time scale. In the following, we detail the kinetic Monte Carlo simulation for the model introduced in Sec. 6.1. Rotational dynamics is implemented by picking a molecule at random and rotating it by an angle $\delta\theta$ chosen with equal probability from the interval $[-\Theta, \Theta]$. The maximum rotational step size $\Theta$ is connected to the molecular self-diffusion constant $D_\theta$ via a Monte Carlo time step $dt$ [237]

$$\Theta = \sqrt{2 D_\theta\, dt}\,. \tag{6.2}$$

The Monte Carlo time step $dt$ is set such that a single Monte Carlo trial move is accepted with a rate close to one, which avoids non-local moves and guarantees a reliable dynamics [64, 237, 254]. In Sec. 6.4 we fix $dt = 10^{-4}$ while in Sec. 6.5 we fix $dt = 10^{-5}$ to increase the time resolution. Both values ensure an acceptance probability close to one. For the self-diffusion constant of our simple molecular model, we rely on the result for a very long

cylinder [48, 255]

$$D_\theta = \frac{3D_0}{\pi L^2}\big(\ln\sigma - 0.622 + 0.917/\sigma - 0.050/\sigma^2\big)\,, \tag{6.3}$$

where $L$ is the cylinder length, $\sigma$ the cylinder aspect ratio and $D_0 = k_\mathrm{B}T/(\eta_S L)$ with $k_B$ the Boltzmann constant, $T$ the temperature, and $\eta_S$ the shear viscosity of the fluid. Since our needles are infinitely thin, we choose $\sigma = 1000$ and for simplicity, the rotational diffusion constants of *trans* and *cis* molecule is assumed to be the same.

Both rotational motion and isomerization take place under the influence of the interaction potential $U(\mathcal{O})$. At each Monte Carlo step a molecule is picked at random and rotated and isomerized using the set of rules defined in the previous section. For example, during thermal erasure the *cis*-to-*trans* isomerization rate is fixed by the probability $P_\mathrm{th}(c \to t)$. Thus, when the randomly selected molecule is in the *cis* isomeric state, a random number $rand \in (0, 1)$ is extracted from an uniform distribution and the molecule is isomerized if $rand \leq P_\mathrm{th}(c \to t)$. After a trial move of a single molecule, the number of overlaps and the energy $U(\mathcal{O}_\mathrm{new})$ of the new configuration are evaluated and compared to the old configuration with $U(\mathcal{O}_\mathrm{old})$. Following the standard Metropolis scheme, the move is accepted with probability

$$p = \min 1, \exp(-1/(k_\mathrm{B}T)[U(\mathcal{O}_\mathrm{new}) - U(\mathcal{O}_\mathrm{old})])\,. \tag{6.4}$$

In the following we express $k_\mathrm{B}T$ in units of $U_\mathrm{step}$.

A complete sweep consists of $N$ trial moves and the running Monte Carlo time is measured in units of $dt$. Thus, $t_{MC} = N_s$, where $N_s$ is the number of Monte Carlo sweeps. The number density of the model molecules is defined as $\rho = N/l^2$, where $l$, in units of $L$, is the side length of the square simulation box. For all the results presented in this Chapter, we use a total of $N = 10000$ molecules under periodic boundary conditions.

As initial condition, we use a configuration, in which both isomers are equally present. The *trans* molecules exhibit orientational order while *cis* molecules are randomly oriented. Starting from this configuration, we then follow the relaxation of the birefringence towards equilibrium.

## 6.3 Birefringence relaxation

The degree of alignment within the system is evaluated by the nematic order parameter $S(t)$. Since *trans* isomers have much higher shape anisotropy than *cis* isomers [32, 200], we evaluate the nematic order parameter only for the *trans* isomers. We calculate the nematic order parameter as the positive eigenvalue of the tensor order parameter

$$T_{\alpha\beta}(t) = \langle N_t^{-1}(t) \sum_{\substack{i=1 \\ i\in\{trans\}}}^{N_t(t)} (2u_\alpha^i(t)u_\beta^i(t) - \delta_{\alpha\beta})\rangle\,, \tag{6.5}$$

where $u_\alpha^i(t)$ is the $\alpha$-th Cartesian coordinate of the unit vector pointing along the central segment of the $i$-th molecule in the *trans* configuration at time $t$ and $\langle\ldots\rangle$ denotes non-equilibrium averaging, for which we used at least 10 different runs. As demonstrated in Sec. 2.2.3, the monolayer birefringence $\Delta n(t)$ is proportional to the degree of molecular alignment in a single-component system. In a mixture of isotropic and anisotropic

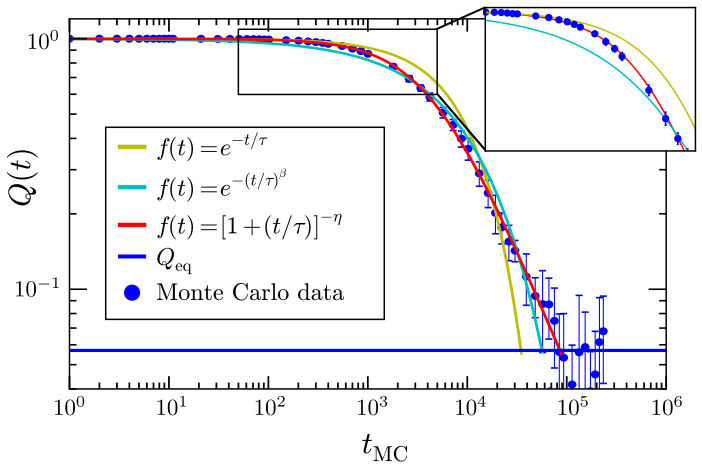


FIGURE 6.2: Time evolution of $Q(t)$ as defined in Eq. (6.6). Blue points are the kinetic Monte Carlo data. Fitting functions are shown as continuous lines. The horizontal blue line gives the equilibrium value $Q_{\rm eq}$ of $Q(t)$. The inset zooms in on the squared area with log scale on the horizontal axis and linear scale on the vertical axis. The simulation data correspond to a thermal erasure process with $k_{\rm B}T = 4.5$, $\rho = 20$, $S(0) = 0.633$, $N_{\rm t}(0) = N$ and $dt = 10^{-4}$.

molecules, the birefringence is also proportional to the number of rod-like molecules [104]. Therefore, to monitor birefringence relaxation, we keep track of

$$Q(t) = \frac{\Delta n(t)}{\Delta n(0)} = \frac{S(t)N_t(t)}{S(0)N_t(0)}\,. \tag{6.6}$$

The data points in Fig. 6.2 give a typical temporal relaxation of $Q(t)$ from our kinetic Monte Carlo scheme.

We now illustrate how we discriminate between three possible functional forms of the relaxation dynamics of $Q(t)$. Recall that simple relaxation processes are expected to show an exponential form $\phi(t) = e^{-t/\tau}$ (a Maxwell-Debye relaxation), which is characterized by a well-defined time $\tau$ that fully determines the kinetics of the system. In some systems, however [205], the relaxation significantly deviates from an exponential form and is described either by a stretched exponential decay $\phi(t) = e^{-(t/\tau)^\beta}$ with $0 < \beta < 1$ or by an asymptotic power law as in Eq. (3.5).

The following procedure is used to discriminate between an exponential, a stretched-exponential, and an asymptotic power-law relaxation of $Q(t)$. For each choice of model parameters, we run kinetic Monte Carlo simulations until $Q(t)$ has reached a clear steady-state value $Q_{\rm eq}$ (illustrated as an horizontal line in Fig. 6.2). The equilibration time $t_{\rm eq}$ is the first time for which $Q(t_{\rm eq}) = Q_{\rm eq}$. $Q(t)$ is then fitted by least-square minimization over the range $t \in [0, t_{\rm eq}]$ with the three functional forms given in Fig. 6.2.

For each fit curve a goodness-of-fit test is performed [256]. We evaluate the reduced chi-squared statistics using

$$\chi^2_{\rm red} = \frac{\chi^2}{\nu} = \frac{1}{\nu}\sum_{i=1}^{n}\frac{(E_i - O_i)^2}{\sigma_i^2}\,, \tag{6.7}$$

where $n$ is the number of Monte Carlo points in the fitting interval (blue points before equilibration in Fig. 6.2), $O_i$ is the observed value of the $i$-th point, $E_i$ is the corresponding

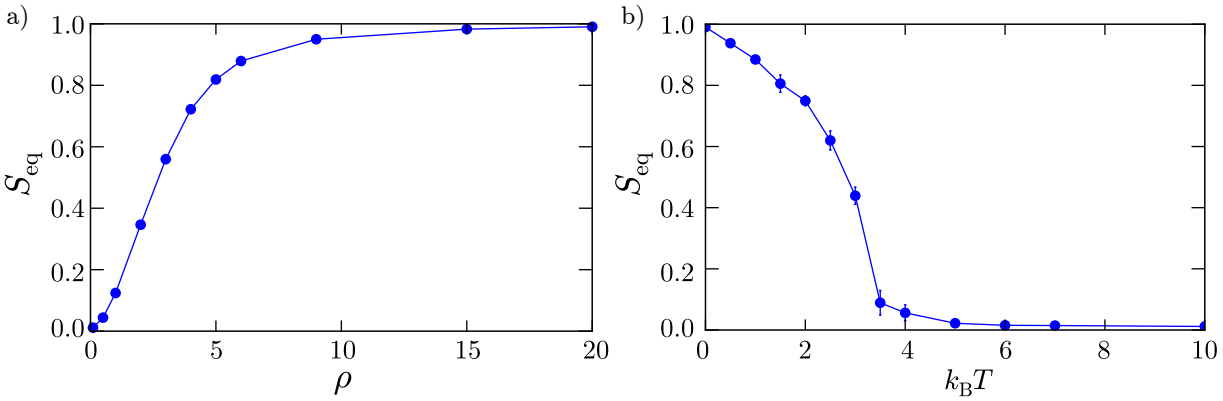


FIGURE 6.3: Equilibrium value of the nematic order parameter $S_{eq}$ in a system of *trans* molecules with finite size. (a) $S_{eq}$ versus $\rho$ for hard needles that are not allowed to overlap. (b) $S_{eq}$ versus $k_BT$ for fixed $\rho = 20$. Lines are guides for the eye.

value as obtained from the least-square minimization, $\sigma_i$ is the standard deviation of the $i$-th observed value (error bars in Fig. 6.2), and $\nu = n - k - 1$ is the number of degrees of freedom with $k$ number of fitting parameters. In general, $\chi^2_{red} \gg 1$ indicates that the data are poorly fitted by the model. Instead, when $\chi^2_{red} \ll 1$ the data are over-fitted by the model (for example there are too many fitting parameters). Thus, the most reliable fit function is chosen as the one with the value of the reduced $\chi^2_{red}$ closest to 1 [256]. In the example given in Fig. 6.2, we obtain $\chi^2_{red} = 9.65$ for the exponential function, $\chi^2_{red} = 2.32$ for the stretched-exponential, and $\chi^2_{red} = 0.54$ for the asymptotic power law. The power law thus clearly provides the best fit of the simulation data. The results of the fitting procedure in different regions of parameter space and under different initial conditions will be discussed in the following two sections.

## 6.4 Relaxation dynamics in a pure *trans* system

In this section we present the results of the kinetic Monte Carlo simulations for a system that only contains *trans* molecules.

First, we characterize the equilibrium properties of the system with temperature $T$ and density $\rho$. Figure 6.3 shows the equilibrium value of the nematic order parameter, $S_{eq}$, determined after equilibration. Fig. 6.3(a) refers to molecules with hard-core interactions that cannot overlap at all. The steady-state value of the nematic order parameter shows a steep increase with $\rho$. Fig. 6.3(b) instead plots $S_{eq}$ versus $k_BT$ at $\rho = 20$. If the temperature is sufficiently high, molecules can pass over their neighbors by creating overlaps and thereby drastically reduce $S_{eq}$. So, allowing the molecules to overlap, results in an isotropic state at sufficiently high temperatures even at high in-plane packing density.

We now characterize the relaxation dynamics of the birefringence at different temperatures. We fix the initial degree of the nematic order to $S(0) = 0.6$ (the same qualitative results are obtained using values from $S(0) \approx 0.5$ to $S(0) \approx 1.0$) and follow the temporal evolution of $S(t)$ while it relaxes back to its equilibrium value $S_{eq}$. First, we analyze the rotational diffusion of the molecules, which results in the decay of $Q(t)$,

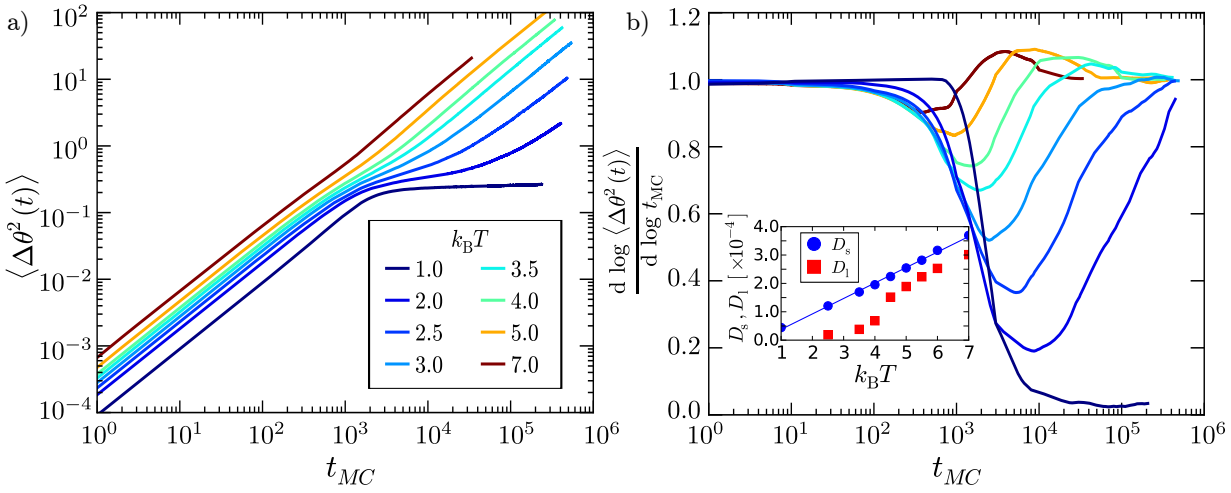


FIGURE 6.4: Rotational dynamics in a system of *trans* molecules for different $k_BT$, at density $\rho = 20$, and with initial nematic order $S(0) = 0.6$. The legend in (a) applies to both graphs. (a) Rotational mean square displacement $\langle \Delta\theta^2(t) \rangle$ versus time. (b) The logarithmic derivative of $\langle \Delta\theta^2(t) \rangle$ to extract the local exponent $\nu$ in $\langle \Delta\theta^2(t) \rangle \propto t^\nu$. The extent of the subdiffusive regime ($\nu < 1$) increases with decreasing temperature. The inset shows the short- (blue circles) and long-time (red squares) diffusion constants as a function of $k_BT$.

by looking at the rotational mean square displacement

$$\langle \Delta\theta^2(t) \rangle = \Big\langle \frac{1}{N} \sum_{i=1}^{N} (\theta_i(t) - \theta_i(0))^2 \Big\rangle , \tag{6.8}$$

where $\theta_i(t)$ is the orientation angle of the $i$-th molecule at time $t$. In Fig. 6.4(a), we plot $\langle \Delta\theta^2(t) \rangle$ versus $t_{MC}$ for different temperatures in a system with fixed density $\rho = 20$. In addition, Fig. 6.4(b) shows the logarithmic derivative of the rotational mean square displacement, which gives the local exponent $\nu$ in $\langle \Delta\theta^2(t) \rangle \propto t^\nu$. Anomalous diffusion has $\nu \neq 1$. Initially, the molecules diffuse with a diffusion constant $D_s$ that increases linearly with temperature, as expected from the Einstein relation [see inset of Fig. 6.4(b)]. When the needles start to overlap, a subdiffusive regime emerges and its extent increases with decreasing temperature [see Fig. 6.4(b)]. Ultimately, normal diffusion is recovered even in systems where nematic order is well developed (for instance at $k_BT = 2.5$ one finds $S_{eq} \approx 0.6$ in Fig. 6.3). In order to diffuse, molecules have to pass each other by creating overlaps. At low temperatures, crossing energy barriers makes rotational diffusion an activated process. Hence, the long-time diffusion constant $D_l$ is no longer linear in temperature [see inset of Fig. 6.4(b)]. We remind the reader that both a transient subdiffusive regime and a breakdown of the Einstein relation are common signatures of glasslike dynamics, as pointed out in Sec. 3.4.2.

Rotational diffusion causes initial nematic order to fully decay for $k_BT \geq 4$. Figure 6.5(a) shows the relaxation of $Q(t) = S(t)/S(0)$ at fixed $\rho = 20$ and different $k_BT$, while in Figure 6.5(b) we keep temperature at $k_BT = 4.5$ and vary density $\rho$. In a high-temperature or low-density regime the relaxation is very well fitted by an exponential function [$k_BT \geq 7.0$ in Fig. 6.5(a) and $\rho \leq 14.0$ in Fig. 6.5(b)], while in a high-density, low-temperature regime [$k_BT \leq 5.0$ in Fig. 6.5(a) and $\rho \geq 18.0$ in Fig. 6.5(b)] the power-law decay defined in Eq. (3.5) provides an excellent fit of the simulation data. In this

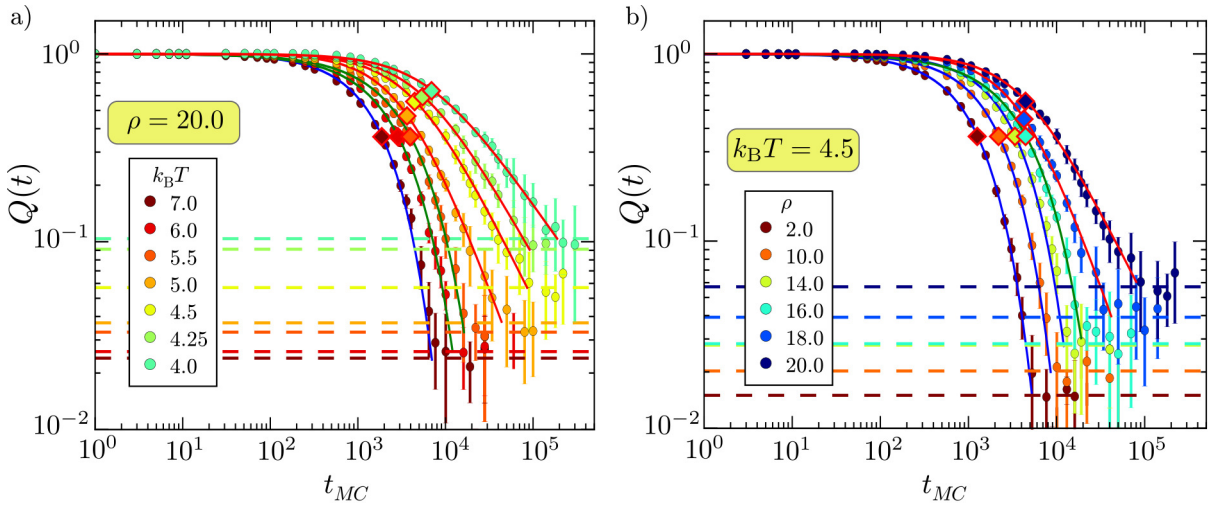


FIGURE 6.5: Relaxation of the birefringence $Q(t)$ in a system of *trans* molecules with initial nematic order $S(0) = 0.6$: (a) for different $k_BT$ at density $\rho = 20$, and (b) at different $\rho$ for $k_BT = 4.5$. Circles show the numerical results and the continuous lines the best-fitting functions with blue for exponential, green for stretched-exponential, and red for power-law decay. The characteristic times of the relaxation curves are indicated as diamonds. Horizontal dashed lines show the equilibrium value of $Q(t)$ with matching colors.

regime both the exponential and stretched-exponential functions give significant residual errors. Our Monte Carlo results are best fitted by a stretched exponential function with $\beta \approx 0.8$ in an intermediate regime [$k_BT = 5.5, 6$ in Fig. 6.5(a) and $\rho = 16.0$ in Fig. 6.5(b)]. To summarize, the interaction with neighboring molecules, which is more relevant at low temperatures and high densities, causes a transition from an exponential decay of $Q(t)$ to a power-law relaxation.

As anticipated in Sec. 3.4.2, non-exponential relaxation originates from the presence of a wide distribution of relaxation times in the system. In the concept of dynamic heterogeneity [65, 66], this distribution is traced back to spatial and temporal variations in the local structure of the system, which then determines its dynamic evolution. Molecules diffusing slower or faster than the average become spatially correlated, giving rise to regions with slow and fast dynamics. Hence, averaging the dynamics over this heterogeneous environment leads to an overall non-exponential relaxation. A typical quantity to monitor this dynamic heterogeneity is a four-point correlation function, which we introduce here for the angular displacement following Ref. [65]. We define the mobility $c_i(t)$, in order to quantify how mobile the molecule $i$ is,

$$c_i(t) = \exp[-\Delta\theta_i(t)^2] - \frac{1}{N}\sum_{j=1}^{N} \exp[-\Delta\theta_j(t)^2]\,, \tag{6.9}$$

where $\Delta\theta_i(t)^2$ is defined as in Eq. (6.8). The variable $c_i(t)$ has zero mean and is positive (negative) if the $i$-th molecule moves less (more) than the average. The four-point correlation function is then

$$G_4(r,t) = \frac{\sum_{i,j} c_i(t)c_j(t)\delta(r - |\vec{r}_{ij}|)}{\sum_{i,j} \delta(r - |\vec{r}_{ij}|)}\,, \tag{6.10}$$

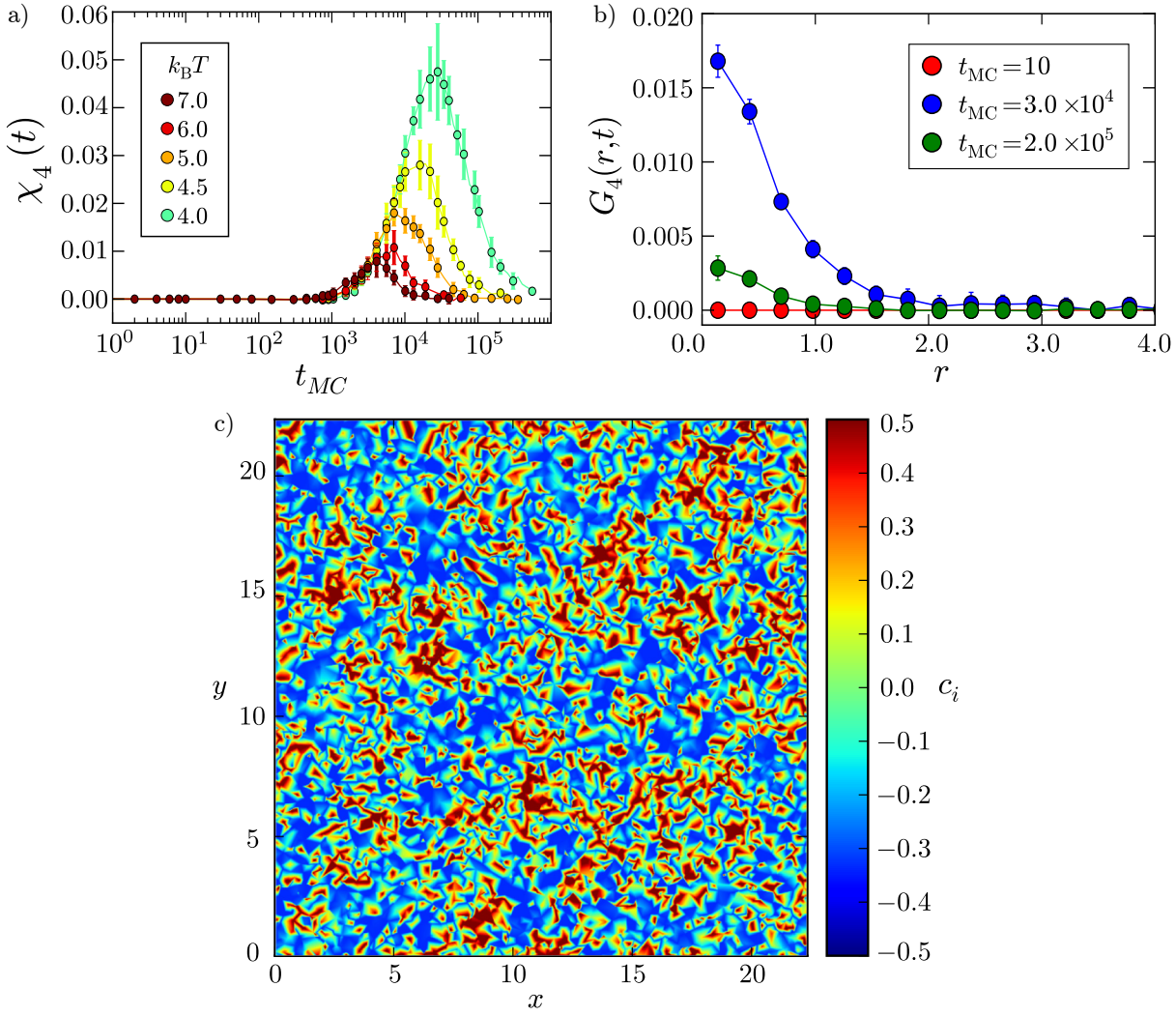


FIGURE 6.6: (a) Temporal evolution of the dynamical susceptibility $\chi_4(t)$ for different $k_BT$ at $\rho = 20$ and with $S(0) = 0.6$. (b) Four-point correlation function $G_4(r,t)$ plotted versus $r$ at different times for $k_BT = 4.0$ and $\rho = 20.0$. The peak in $\chi_4(t)$ indicates extended domains of correlated rotational motion. (c) The mobility $c_i(t)$ defined in Eq. (6.9) color-coded in the whole simulation box for $k_BT = 4.0$, $\rho = 20.0$, and at time $t_{MC} = 3.0 \times 10^4$, right at the maximum of $\chi_4(t)$.

where $|\vec{r}_{ij}|$ is the distance between molecule $i$ and $j$ and $\delta$ is the Dirac delta function. The correlation function $G_4(r,t)$ measures the spatiotemporal correlations in the dynamics of the molecules over a distance $r$ at time $t$. We remark the difference between Eq. (6.10) and Eq. (3.13): a four-point correlation function as in Eq. (3.13) is typically used to characterize systems at equilibrium (for instance a supercooled liquid). Since we are interested in a relaxation process, the correlation function in Eq. (6.10) does not imply any ensemble average. The presence of correlated domains in space and the degree of dynamic heterogeneity is monitored by the dynamical four-point susceptibility for the angular displacement [66, 257],

$$\chi_4(t) = \int \mathrm{d}r\, G_4(r,t)\,. \tag{6.11}$$

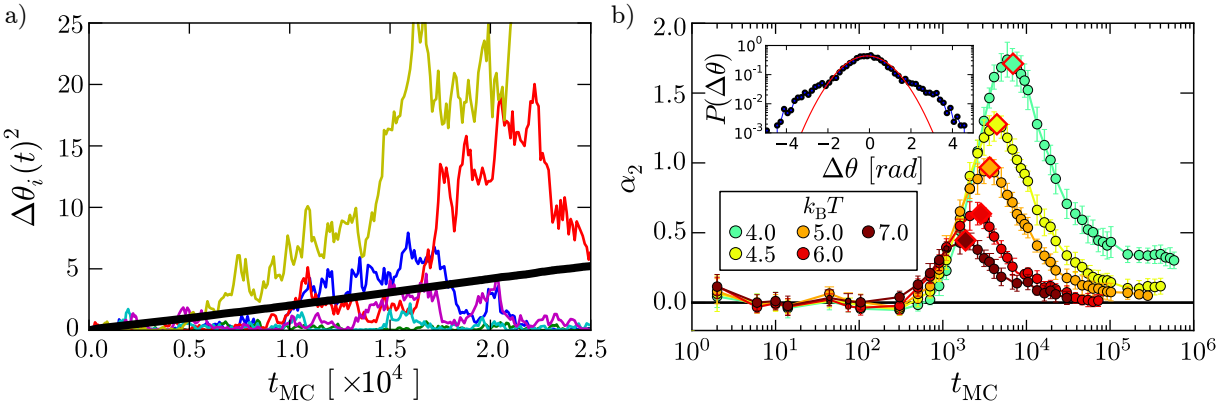


FIGURE 6.7: (a) Square displacement of selected individual molecules plotted versus time for $k_{\rm B}T = 4.0$ and $\rho = 20.0$. The thick black line is the mean value over all molecules. (b) Temporal evolution of the non-Gaussian parameter $\alpha_2$ of the probability distribution $P(\Delta\theta(t))$ for different $k_{\rm B}T$ at $\rho = 20$ and with $S(0) = 0.6$. Values of $\alpha_2 \neq 0$ indicate non-Gaussian tails in the distribution $P(\Delta\theta(t))$ of rotational steps, i.e., an excessive number of molecules significantly faster or slower than the average. Inset: Example of $P(\Delta\theta(t))$ at $t_{MC} = 7.0 \times 10^3$ and for $k_{\rm B}T = 4.0$. The red line shows a Gaussian distribution.

It increases with increasing size of correlated domains.

Figure 6.6(c) illustrates the heterogeneity in the rotational mobility of the molecules by plotting the color-coded $c_i(t)$ in the whole simulation box for $k_{\rm B}T = 4.0$, $\rho = 20$, and at $t_{MC} = 3.0 \times 10^4$. Extended domains of correlated molecular rotations are clearly visible. Figure 6.6(b) shows the corresponding four-point correlation function $G_4(r, t)$ for $k_{\rm B}T = 4.0$ in blue, where the correlations in time and space are largest compared to other times (green and red circles). In order to monitor the complete temporal evolution of the dynamical heterogeneities, we present the susceptibility $\chi_4(t)$ in Fig. 6.6(a) for different temperatures and at density $\rho = 20$. The dynamical susceptibility shows a clear peak, which coincides with the time window, during which the power-law relaxation of $Q(t)$ is observed in Fig. 6.5(a). The color plot of Fig. 6.6(c) is obtained at the maximum of $\chi_4(t)$ at $k_{\rm B}T = 4$. The maximum increases with decreasing temperature and therefore demonstrates that regions of correlated motion become more relevant at low temperatures.

Spatio-temporal variations in the local environment of the pinned molecules are also responsible for the anomalous diffusion, which we demonstrate in Fig. 6.4. In Fig. 6.7(a) we show individual molecular trajectories for $k_{\rm B}T = 4.0$ and $\rho = 20$. One already senses that some molecules rotate significantly faster than the average (shown as a thick black line), while all trajectories indicate that rotational diffusion proceeds by sudden jumps. This feature, together with the spatio-temporal correlations discussed before, are also common signatures of a glass-like dynamics [227, 258–261] . As pointed out already in Sec. 3.4.2, a non-Gaussian distribution of molecular displacements is another universal feature of finite-dimensional glass-like dynamics [220]. To investigate this point, we evaluated the non-Gaussian parameter $\alpha_2$ of the distribution of molecular displacement $P(\Delta\theta)$. In two dimensions it is calculated using the second and fourth moment of $P(\Delta\theta)$,

$$\alpha_2(t) = \frac{\langle \Delta\theta^4(t) \rangle}{\langle \Delta\theta^2(t) \rangle^2} - 3\,, \tag{6.12}$$

where for a Gaussian distribution one has $\alpha_2 = 0$. In Fig. 6.7(b), we show $\alpha_2$ for different

temperatures $k_BT$ and at density $\rho = 20$. The distribution $P(\Delta\theta)$ becomes highly non-Gaussian as also demonstrated in the inset, which shows $P(\Delta\theta)$ for $k_BT = 4.0$ and at the time, when $\alpha_2(t)$ maximal. Fast rotating molecules are responsible for the non-Gaussian tails of the distribution. The peak in $\alpha_2$ increases and shifts to later times upon cooling, which again coincides with the developing non-exponential relaxation of the birefringence. Interestingly, the characteristic times in the relaxation laws for $Q(t)$, shown as diamond markers in Fig. 6.7(a), agree nicely with the locations of the maxima in $\alpha_2(t)$.

## 6.5 Relaxation dynamics during isomerization

In this section we explore the relaxation of birefringence $Q(t)$ in a system, in which both *trans* and *cis* molecules are present. In particular, we investigate how the nearly isotropic *cis* molecules influence the relaxational dynamics of $Q(t)$ under two different isomerization scenarios: thermal erasure and CP erasure.

The model has a rather rich parameter space and its full exploration is beyond our scope. In the following, we fix the initial conditions to be close to the experimental values and explore the relaxational dynamics of $Q(t)$ for different isomerization rates. We prepare the initial state with an equal number of *trans* and *cis* molecules, $N_t(0) = N_c(0)$, and order parameter $S(0) = 0.6$; both values are close to the estimates carried out in Ref. [1]. The *cis* molecules are randomly oriented at $t = 0$ and do not contribute to $S(t)$. In this section we choose the time step $dt = 10^{-5}$ to increase the temporal resolution, which results in an equilibration time of up to 9 weeks on an Intel Xeon X5550 machine with a 2.66 GHz CPU. In order to compare the results of this section directly with the results of Sec. 6.4, we still give the Monte-Carlo time $t_{\mathrm{MC}}$ in units of $dt = 10^{-4}$.

### 6.5.1 Thermal erasure

Here, we discuss the relaxation of the birefringence, when the monolayer is not illuminated. Since the *trans* isomer is the ground-state of the dMR, all the molecules in the *cis* configuration will isomerize back to the *trans* state after some characteristic time. As discussed in detail in Sec. 6.1, the *cis* to *trans* isomerization rate of isolated molecules is the isomerization probability $P_{\mathrm{th}}(c \to t)$.

In view of the results discussed in Sec. 6.4, we expect the relaxation dynamics to be exponential in the high-temperature and low-density regime, regardless of the isomerization probability. Therefore, we fix both temperature and density to $k_BT = 4.0$ and $\rho = 20.0$, respectively, where the pure *trans* system shows a clear power-law decay of the birefringence, and monitor how this decay is influenced by the isomerization rate.

Figure 6.8(b) shows the temporal evolution of the number of *trans* isomers for different $P_{\mathrm{th}}(c \to t)$. We expect an exponential relaxation and, indeed, the Monte Carlo data (circles) are well fitted with

$$\frac{N_{\mathrm{t}}(t)}{N} = 1 - \frac{N_{\mathrm{c}}(0)}{N} e^{-t/\tau_{\mathrm{c}}}\,, \tag{6.13}$$

where the fit parameter, the relaxation time $\tau_{\mathrm{c}}$, is proportional to the inverse isomerization probability, $\tau_{\mathrm{c}} = 1.54\, P_{\mathrm{th}}^{-1}(c \to t)$ [see inset of Fig. 6.8(b)]. We find $\tau_{\mathrm{c}} > P_{\mathrm{th}}^{-1}(c \to t)$ because in a crowded environment some of the attempted isomerization events are rejected as they generate more overlaps between the molecules.

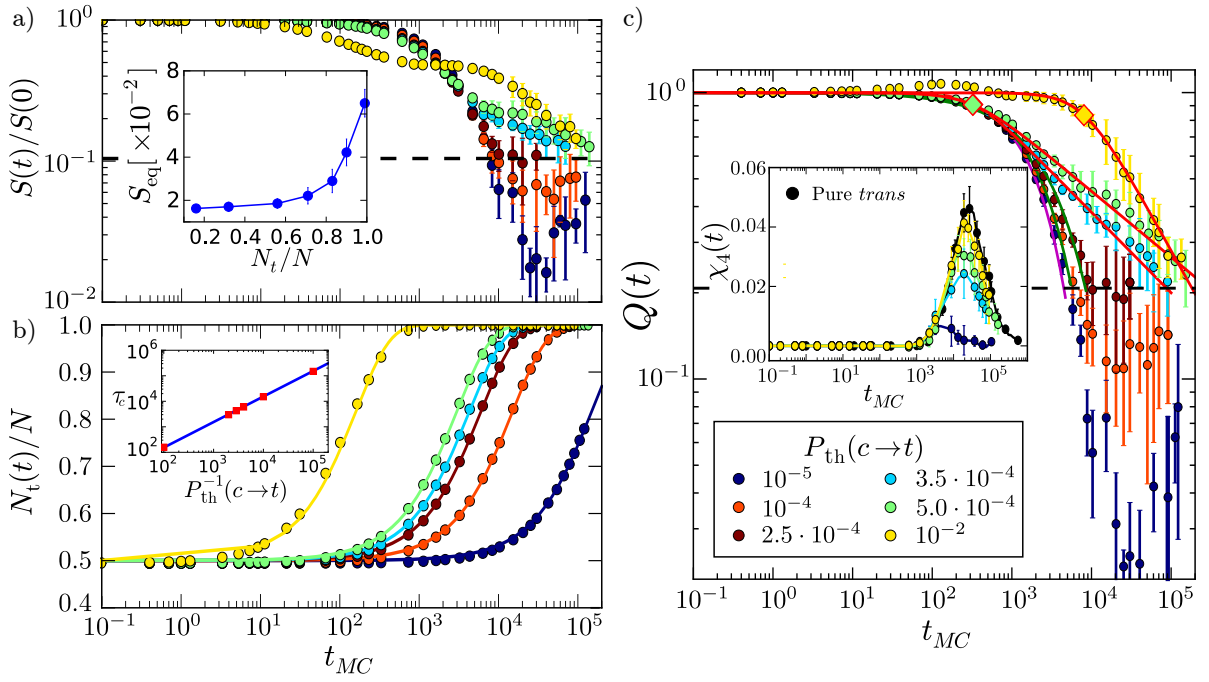


FIGURE 6.8: Relaxation towards equilibrium during thermal erasure in a system with $\rho = 20.0$ and $k_BT = 4.0$. The legend in (c) applies to all graphs. (a) Temporal evolution of the nematic order parameter $S(t)/S(0)$. The horizontal dashed line marks the equilibrium value to which all the curves have to converge. The inset shows the equilibrium value $S_{eq}$ as a function of the relative number of *trans* isomers, $N_t/N$. (b) Relative number of *trans* isomers, $N_t/N$, during thermal erasure. Fits of the simulation data with Eq. (6.13) are shown as solid lines with matching colors. The inset plots the isomerization time $\tau_c$ versus $P_{th}^{-1}(c \to t)$ (red squares). The fitted blue line is $\tau_c = 1.54\,P_{th}^{-1}(c \to t)$. (c) Temporal relaxation of the birefringence $Q(t)$. The horizontal dashed line marks the equilibrium value of $Q(t)$. The full lines are the best fits to an exponential (magenta), a stretched exponential (green), or a power law (red). Diamonds indicate the characteristic times of the power law relaxation. The inset shows the dynamical susceptibility $\chi_4(t)$ for *trans* molecules already present at $t = 0$. As a reference the black circles give $\chi_4(t)$ for the pure *trans* system at the same $\rho$ and $k_BT$.

In Figs. 6.8(a) and (c) we show the respective temporal evolutions of the nematic order parameter $S(t)/S(0)$ and the birefringence $Q(t) \propto N_t(t)S(t)$, which originate from the alignment of the *trans* isomers. We also evaluate the dynamical susceptibility $\chi_4(t)$ defined in Eq. (6.11), but only on the subset of molecules that are in the *trans* configuration at the beginning of the simulation at $t_{MC} = 0$. The results are plotted in the inset of Fig. 6.8(c), where we also include the dynamical susceptibility for the pure *trans* system at $\rho = 20$ at $k_BT = 4.0$ (black circles) as a reference. This will allow us to to quantify how the presence of the *cis* isomers influences the development of dynamic heterogeneities. The temporal relaxation of both $S(t)$ and $Q(t)$ strongly depends on the isomerization rate. Analyzing Figs. 6.9(a), (b) and (c), we identify four different regimes:

**1)** For sufficiently small relaxation rate [$P_{th}(c \to t) = 10^{-5}$ in Fig. 6.8], the birefringence $Q(t)$ relaxes exponentially. On the time scale of the declining $S$, the number of *cis* molecules stays constant [compare plots (a) and (b)]. They thus create a more uniform environment, as indicated by the nearly vanishing dynamical susceptibility $\chi_4$, in which $S(t)$ and $Q(t)$ relax exponentially and much faster than the pure *trans* system for the same temperature and density in Sec. 6.4. Note that at late times $Q(t)$ first

falls below its equilibrium value (dashed horizontal line) and then increases again. The reason is that the equilibrium value of $S$ depends on the number of *trans* molecules [inset of Fig. 6.8(a)] because the presence of the nearly isotropic *cis* molecules decreases $S_{\mathrm{eq}}$. Since $N_{\mathrm{t}}$ increases for $t_{MC} > 10^4$, $Q(t)$ also increases.

**2)** For $P_{\mathrm{th}}(c \to t) = 10^{-4}$ and $2.5 \cdot 10^{-4}$ the best fitting function for the temporal evolution of $Q(t)$ is provided by a stretched exponential with $\beta \approx 0.8$ indicating the transition to the power-law decay.

**3)** At intermediate isomerization rates $P_{\mathrm{th}}(c \to t) = 3.5 \cdot 10^{-4}$ and $5.0 \cdot 10^{-4}$ the power-law relaxation provides the best fit of the simulation data. Here, the isomerization of the randomly oriented *cis* molecules into the *trans* state happens on the same time scale as the relaxation of the nematic order parameter. Thus, $Q(t)$ does not decay in the static disordered distribution of *cis* molecules but in a dynamic and heterogeneous environment, as demonstrated by the clear peak in $\chi_4(t)$. As a result, the relaxation of $Q(t)$ follows a power law. Its characteristic time $\tau_t$ does not change significantly, but the isomerization probability seems to control the power-law exponent. We find $\eta = 0.281$ at $P_{\mathrm{th}}(c \to t) = 3.5 \cdot 10^{-4}$ and $\eta = 0.225$ at $P_{\mathrm{th}}(c \to t) = 5.0 \cdot 10^{-4}$.

**4)** The situation changes again if the isomerization rate is very large [$P_{\mathrm{th}}(c \to t) = 10^{-2}$ in Fig. 6.8]. All the *cis* isomers rapidly isomerize into *trans* molecules with random orientation and $S(t)$ drops to $S(0)/2$. This is compensated by the resulting increase in $N_t(t)$, which ultimately generates a bump in $Q(t)$ at $t_{\mathrm{MC}} \approx 10^2$. Once isomerization is completed at $t_{\mathrm{MC}} \approx 10^3$, the system is composed of only *trans* molecules the aligment of which relaxes via rotational motion. This is the same situation as discussed in Sec. 6.4. The environment is heterogeneous as indicated by the peak in the dynamical susceptibility, which is nearly as large as in the pure *trans* system of Sec. 6.4. Without the initial bump, $Q(t)$ is fitted well by a power-law with a larger characteristic time and a larger power-law exponent $\eta \approx 0.5$ as compared to case **3)** but similar to the pure *trans* system.

Summarizing the results in Fig. 6.8, we find that *cis* isomers pinned at random positions not only accelerate the birefringence relaxation compared to the pure *trans* system but also prevent the development of the dynamical heterogeneity that is responsible for a non-exponential decay. We attribute this behavior to the nearly isotropic shape of *cis* isomers, which, regardless of their orientations, create a similar environment for the exisiting *trans* isomers. In contrast, newly formed *trans* isomers can adjust their orientations to their neighbors and thereby allow for the formation of dynamical heterogeneities. In the experiments of Ref. [204] the lifetime of *cis* isomers during thermal erasure is estimated as 0.7s, while the characteristic time of the power-law decay is measured as $\tau_{\mathrm{th}} \approx 2$s. These values are achievable by isomerization rates between our cases **3)** and **4)**.

### 6.5.2 CP erasure

Illumination of the SAM with CP light induces *trans*-*cis* isomerization cycles at a rate much faster than the spontaneous relaxation due to thermal erasure. Therefore, we neglect the thermally induced *cis*-to-*trans* transition when modeling the CP erasure process. As discussed in Sec. 6.1, in order to take into account the different light absorption of the two isomers, we introduce the two respective probabilities, $P_{\mathrm{CP}}(t \to c)$ and $P_{\mathrm{CP}}(c \to t)$, for *trans*-to-*cis* and *cis*-to-*trans* isomerization. Since light is circularly polarized, the isomerization probabilities do not depend on the molecular orientation.

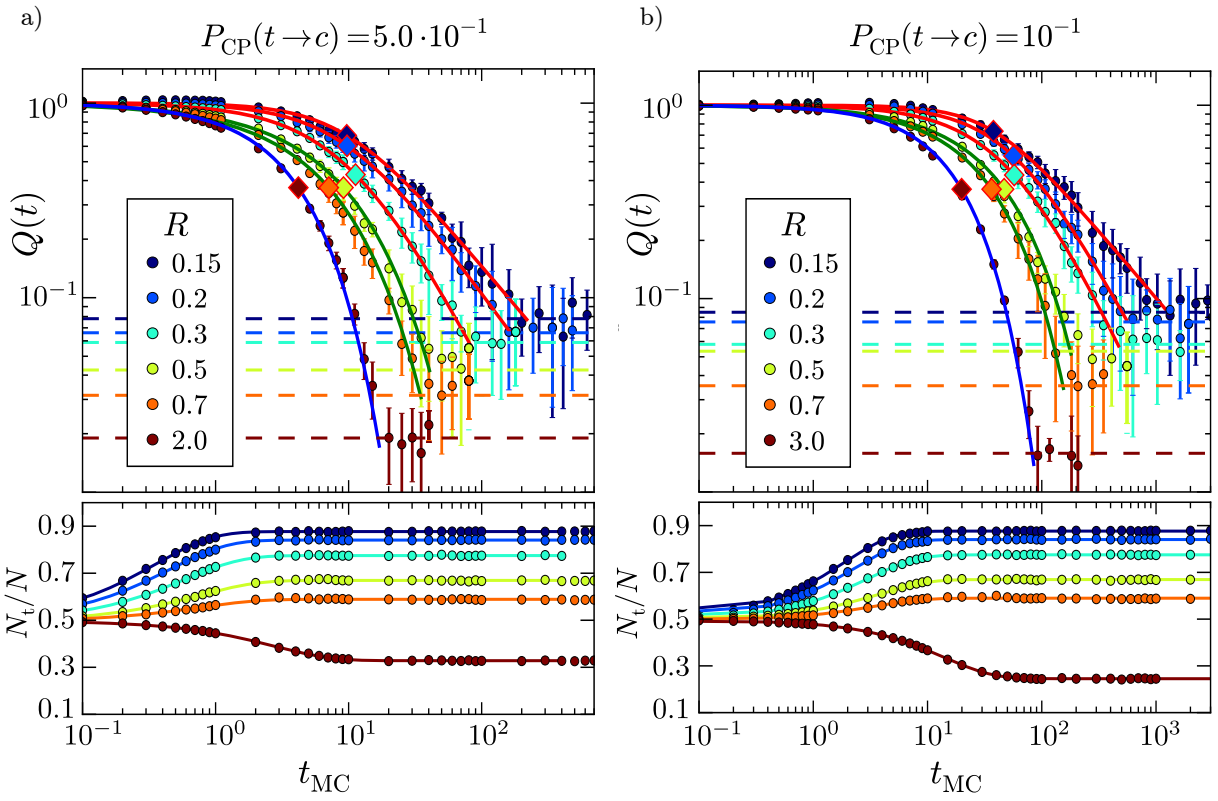


FIGURE 6.9: Relaxation of the birefringence $Q(t)$ and of the relative number of *trans* isomers, $N_t(t)/N$, during CP erasure for different ratio $R$ at fixed $\rho = 20$ and $k_BT = 4$. The *trans*-to-*cis* isomerization rate is $P_{CP}(t \to c) = 5.0 \cdot 10^{-1}$ in (a) and $P_{CP}(t \to c) = 10^{-1}$ in (b). The *cis*-to-*trans* isomerization rates are $P_{CP}(c \to t) = P_{CP}(t \to c)/R$. The best-fitting function for the relaxation of $Q(t)$ are shown as solid lines, blue for the exponential, green for the stretched-exponential, and red for the power-law relaxation of Eq. (3.5). The diamond markers with matching colors indicate the characteristic times $\tau_t$. The fitted exponents are given in Table 6.1. The horizontal dashed lines mark the the steady-state value of $Q(t)$ for different $R$ with matching colors. The numerical results for $N_t(t)/N$ are fitted with Eq. 6.15 (solid lines).

In order to limit the computational cost, we do not explore the full range of isomerization probabilities. Instead, we choose their values such that the characteristic times of birefringence relaxation for thermal and CP erasure matches the experimental observations, where they differ by approximately two decades in time (see the diamond markers in Fig. 3.5). Because illumination of the monolayer produces a very negligible amount of heat [1], we fix both density and temperature at $\rho = 20$ and $k_BT = 4$, exactly as during thermal erasure discussed in Sec. 6.5.1.

In Fig. 6.9 we show the relaxation of $Q(t)$ and $N_t(t)$ towards their steady-state values starting with $N_t = 0.5$ at $t = 0$. In Fig. 6.9(a) we set $P_{CP}(t \to c) = 5.0 \cdot 10^{-1}$ while in Fig. 6.9(b) $P_{CP}(t \to c) = 10^{-1}$. The backward isomerization rates, $P_{CP}(c \to t)$, are chosen by the ratio $R = P_{CP}(t \to c)/P_{CP}(c \to t)$, which also determines the number of isomers in steady state: $R = N_c(t \to \infty)/N_t(t \to \infty)$, as discussed in Sec. 6.1.

The implementation of our kinetic Monte-Carlo simulations suggests that the number of *trans* isomers evolves according to the following kinetic equation,

$$\frac{d\,N_t(t)}{d\,t} = -\frac{1}{\tau_{tc}} N_t(t) + \frac{1}{\tau_{ct}} N_c(t)\,, \tag{6.14}$$

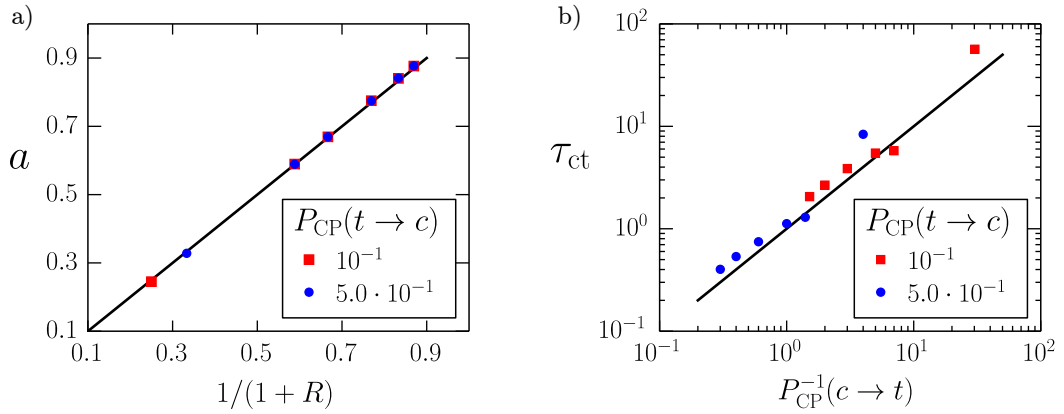


FIGURE 6.10: (a) The fit parameter $a$ in Eq. (6.15), which gives the relative number of *trans* isomers in steady state, plotted versus $1/(1+R)$. (b) The *cis*-to-*trans* relaxation time $\tau_{ct}$ plotted versus the inverse isomerization probability $P_{\rm CP}^{-1}(c \to t)$. In both figures red squares are from simulations with $P_{\rm CP}(t \to c) = 10^{-1}$ and blue circles for $P_{\rm CP}(t \to c) = 5.0 \cdot 10^{-1}$. The straight black lines have zero $y$-intercept and unit slope.

| $P_{\rm CP}(t \to c)$ | $R$ | $\beta$ |
|---|---|---|
| $5.0 \cdot 10^{-1}$ | 0.7 | 0.78 |
| $5.0 \cdot 10^{-1}$ | 0.5 | 0.77 |
| $10^{-1}$ | 0.7 | 0.84 |
| $10^{-1}$ | 0.5 | 0.81 |

| $P_{\rm CP}(t \to c)$ | $R$ | $\eta$ |
|---|---|---|
| $5.0 \cdot 10^{-1}$ | 0.3 | 1.37 |
| $5.0 \cdot 10^{-1}$ | 0.2 | 0.95 |
| $5.0 \cdot 10^{-1}$ | 0.15 | 0.82 |
| $10^{-1}$ | 0.3 | 1.31 |
| $10^{-1}$ | 0.2 | 1.10 |
| $10^{-1}$ | 0.15 | 0.71 |

TABLE 6.1: Fit parameters for the solid lines in Fig. 6.9. Table on the left gives the exponent for the stretched-exponential fit (green lines) and table on the right gives the exponent for the power-law fit (red lines).

where $\tau_{ct}$ and $\tau_{tc}$ are characteristic relaxation times and $N_c(t) = N - N_t(t)$. It is solved by

$$N_t(t)/N = a + b\exp(-t/\tau)\,, \tag{6.15}$$

with

$$a = \frac{1}{1+\tau_{ct}/\tau_{tc}}\,,\quad a+b = \frac{N_t(0)}{N}\,,\ \text{and}\ \frac{1}{\tau} = \frac{1}{\tau_{tc}} + \frac{1}{\tau_{ct}} \tag{6.16}$$

Since $a$ is the steady-state value at $t \to \infty$, we also have $a = 1/(1+R)$, which is confirmed in Fig. 6.10(a). Thus, the ratio of isomerization probabilities also determines the ratio of the two relaxation times, $R = \tau_{ct}/\tau_{tc}$. The fits of the simulated $N_t(t)/N$ in Figs. 6.9(a) and (b) excellently confirm the kinetic model. However, as in the case of thermal erasure, we find $\tau_{ct} > P_{\rm CP}^{-1}(c \to t)$ [see Fig. 6.10(b)], because in a crowded environment some of the attempted isomerization events are rejected.

In Fig. 6.9 we show the best fitting functions for $Q(t)$ as continuous lines. In both Figs. 6.9(a) and (b) the relaxation of the birefringence is exponential for $R < 0.7$, stretched-exponential for $0.7 \le R < 0.3$, and follows a power-law for $R \le 0.3$. The characteristic times of the relaxation are shown as diamond markers and the exponents are given in

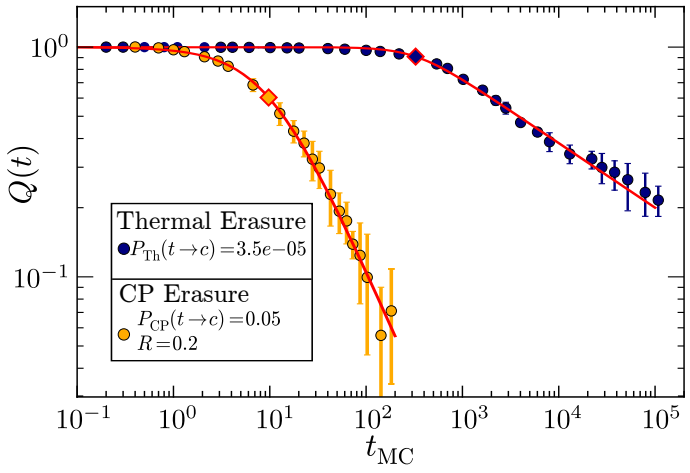


FIGURE 6.11: Comparison of the birefringence relaxation during both CP and thermal erasure as obtained by kinetic Monte Carlo simulations. Solid red lines are fits to the power-law decay of Eq. (3.5). The characteristic times of the power-law relaxation are shown as diamond markers. For both curves $k_{\mathrm{B}}T = 4$ and $\rho = 20$. The isomerization probabilities are given in the legend. Compare with Fig. 3.5.

Table 6.1.

As expected, a larger isomerization rate $P_{\mathrm{CP}}(t \to c)$ shifts the birefringence relaxation to smaller times [compare Figs. 6.9 (a) and (b)] because aligned *trans* molecules are faster transformed to the *cis* state. Unlike the case of thermal erasure, the steady value of $N_t(t)/N$ is reached well before stretched-exponential or power-law relaxation sets in. The relevant characteristic times $\tau_t$ are indicated by diamond markers in Fig. 6.9. Interestingly, for constant $P_{\mathrm{CP}}(t \to c)$ the ratio of isomerization rates $R$ controls the functional form of the relaxation. In the power-law regime, the characteristic times $\tau_t$ do not change significantly, while the power-law exponent $\eta$ heavily depends on $R$ (see Table 6.1).

At a first glance, the behavior in Fig. 6.9 seems surprising. For increasing $R$ the isomerization rate $P_{\mathrm{CP}}(c \to t) = P_{\mathrm{CP}}(t \to c)/R$ decreases and consequently the molecular orientations after isomerization become randomized less frequently. So, we expect the birefringence relaxation to become slower in contrast to the results presented in Fig. 6.9. However, we know already from thermal erasure that *cis* isomers create a uniform environment, where the orientation of *trans* molecules relaxes faster and exponentially. This is the case for $R > 1$, where the *cis* isomers are in the majority in steady state. Decreasing $R$ increases the number of rod-like *trans* molecules, $N_t$. As discussed already for thermal erasure, they hinder the orientational relaxation of their neighbors more efficiently than *cis* molecules. But they also create a more heterogeneous environment, where the birefringence relaxation first follows a stretched exponential and then for further decreasing $R$ becomes a power law. However, we were not able to quantify the dynamic heterogeneity using the dynamical susceptibility of Eq. (6.11) for a subset of molecules as in Sec. 6.5.1 since they continuously cycle between their two configurations.

### 6.5.3 Comparison between thermal and CP erasure

In Fig. 6.11 we show the power-law relaxation of $Q(t)$ for both thermal and CP erasure using typical parameters. Comparing it with Fig. 3.5 gives an idea of the degree of agreement between our model and the experimental results. Birefringence relaxation

is efficiently accelerated by the isomerization cycles induced by illumination with CP light. A similar speedup was demonstrated in Refs. [261–263], where isomerization of an azo-dye embedded in a molecular matrix significantly increased translational diffusion of surrounding molecules. By tuning the isomerization probabilities for CP erasure, we achieved a difference between the characteristic times $\tau_t$ in the power-law decay of approximately two orders of magnitude, in good agreement with the experimental results.

The larger isomerization rates during CP erasure and the presence of *cis* isomers in steady state give a faster power-law relaxation with a larger exponent $\eta$, again in qualitative agreement with the experimental results. Our model also accounts for the smaller steady-state value of $Q(t)$ after illumination with CP light as reported in Ref. [1]. This is due to the presence of the nearly isotropic *cis* molecules that destabilize orientational order.

## 6.6 Summary

First, we studied a system of pure *trans* molecules. Here, the non-exponential, glass-like relaxation of the orientational order inscribed in the monolayer emerges naturally at high densities and low temperatures due to the presence of dynamic heterogeneity. Rotational motion develops a transient sub-diffusive regime upon cooling. At the same time, molecules with dynamics faster and slower than the average become spatially correlated. The spatial average over these regions with different orientational mobilities results in the power-law decay of birefringence.

In a second step we included the possibility that the molecules can assume two different isomeric forms. During thermal erasure, the nearly isotropic *cis* isomers create a uniform environment because they do not align locally with their neighboring molecules. Hence, the orientation of *trans* molecules relaxes exponentially. The experimental power-law relaxation of birefringence is only recovered if a sufficient number of *trans* isomers is present. They slow down orientational relaxation but also initiate the formation of dynamic heterogeneities as in the pure *trans* system.

During CP erasure, light adsorption induces a fast isomerization cycle between *cis* and *trans* isomers and thereby the overall orientational relaxation becomes faster in agreement with experimental results. The functional form of the birefringence relaxation is controlled by the ratio of the two isomerization probabilities, which determine the number of *trans* and *cis* molecules in steady state. As in thermal erasure, a larger number of *cis* isomers speeds up the exponential birefringence relaxation, whereas *trans* isomers in the majority hinder relaxation and ultimately give rise to a power-law decay. Finally, the presence of the nearly isotropic *cis* isomers also explains the smaller steady-state value, which birefringence reaches during CP erasure.

# Chapter 7

# Conclusion

In this Thesis we investigated how liquid-crystal order in two dimensions can be controlled both by molecular geometry and by the interaction of photo-switchable mesogens with light. We used two approaches: first, we studied how molecular geometry influences the formation of self-organized liquid-crystal structures at equilibrium. This study resulted in the complete phase diagram of the bent hard-needle model. Second, we considered an out-of-equilibrium process during which molecules can assume different isomeric configurations. This enabled us to trace the effect of the isomerization process on the system dynamics. In both cases we employed model molecules, whose shape is inspired by that of the azobenzene, an important photo-switchable compound.

We started the Thesis by reviewing some fundamental concepts for the liquid-crystal state of matter in Chapter 2. We discussed several theories of liquid-crystal ordering using free-energy, symmetry and topology arguments. We focused on the mesophases identified in the bent hard-needle model, for which we defined proper order parameters and correlation functions.

In Chapter 3 we discussed photo-switchable molecules and some of their interesting applications. We explained the photo-chemical properties of the azobenzene compound, which is widely used in applications where photo-switchable molecules control liquid-crystal order in thin films. We discussed how illumination with light can influence the molecular ordering in a nematic liquid crystals, in particular when photo-switchable molecules act as mesogens. We explained in detail a series of experiments performed by Fang *et al.* [1], where light is used to significantly speed up the glasslike relaxation of orientational order in a self-assembled monolayer. These experiments motivated the molecular model presented in Chapter 6.

In Chapter 4 we described the numerical methods used in this work. These include Monte Carlo simulations in the canonical and in the isothermal-isobaric ensemble and kinetic Monte Carlo simulations. We also discussed some specialized optimization techniques used to save computational time.

The results for the equilibrium phase behavior of the bent hard-needle model are presented in Chapter 5. We demonstrated that, despite its semplicity, the bent hard-needle model shows a variety of liquid-crystal phases. The stability of these phases is strongly dependent on the molecular shape. For both molecular configurations, we demonstrated the isotropic–quasi-nematic transition to be consistent with a Kosterlitz-Thouless theory of a disclination unbinding scenario. Here, the transition from a isotropic to a quasi-nematic phase makes the orientational correlation function switch from exponential to power-law decay with increasing density. Even if smectic order is expected to be destabilized by thermal fluctuations in two dimensions, we find evidence for

fully stabilized smectic phases in the bent hard-needle model. Further studies, using larger system sizes, are needed to clarify the long-range stability of these layered phases. In particular, the scenario described in Sec. 2.4.2, with the appearance of quasi-nematic order in the layer orientations due to the presence of dislocations, remains to be demonstrated. In this regard, understanding the role of topological defects in the formation of two-dimensional structures is crucial for significant technological advancements [264].

A very appealing result of our investigation is the identification of the modulated-nematic phase made from supramolecular layers. Our simulations are the first to clearly demonstrate such a layered structure in two dimensions and to relate it to molecular geometry. We find the optimal value of the curvature radius to be around $\alpha \approx \pi/10$, when the modulated-nematic phase occurs at the lowest packing density. This finding might particularly be useful in developing novel functional optical materials based on organic bent-core liquid crystals [265, 266], where the formation of polar domains can be used to tune the nonlinear optical properties of the material.

In analogy with the smectic phase, the long-range stability of the modulated-nematic phase also needs to be further investigated. Some dislocations in the supra-molecular layered structure of the modulated-nematic phase already appear in our simulations. It would be interesting to study how to increase the stability of this phase, for example by placing the molecules on a properly textured substrate [267]. This question can be addressed in future numerical studies.

The results for our out-of-equilibrium study are given in Chapter 6. We discussed in detail a molecular model for experiments performed with a self-assembled monolayer of tethered light-switchable dye molecules [1], which can be found in a stable *trans* and a light-induced *cis* state. The monolayer shows power-law relaxation of initial birefringence during thermal erasure and CP erasure. In the latter case, the relaxation is considerably faster. Despite its simplicity, the molecular model discussed in Chapter 6 is able to reproduce the experimental results.

We provided a direct measure for the extension of spatio-temporal correlated domains by defining a out-of-equilibrium dynamical susceptibility, the spatial integral of a four-point correlation function. At high density and low temperature, the spontaneous formation of extended domains of fast- and slowly-rotating molecules (dynamic heterogeneity), is responsible for the power-law decay of the initial birefringence. We found that the presence of the *cis* isomers, which do not align with their neighboring molecules, prevents the formation of dynamic heterogeneity, and causes the relaxation to be exponential. Nevertheless, the experimental power-law relaxation can be reproduced by properly tuning isomerization probabilities.

We attribute the different effect of the two isomers on the system dynamics mainly to their different geometric shapes. The anisotropic *trans* isomers create locally aligned domains, while the nearly isotropic *cis* isomers create a uniform environment. This result suggests the possibility to engineer photo-switchable molecules, and control the difference in the shape anisotropy of the two isomers, in order to ease or obstruct both the formation and the relaxation of orientational order under illumination.

To reproduce the power-law decay of birefringence in our model, we had to fine-tune the parameters within a range of values that are experimentally reasonable. It remains to be demonstrated if the need for this fine tuning is due to our simplified model or a general feature of light-switchable molecules. Future work should address this question by exploring the effect of more complex molecular geometries with more realistic molecular

interactions. These additional improvements could be implemented in our model within the kinetic Monte Carlo simulation scheme.

Another interesting direction for future research would be the investigation of how a transition from different liquid-crystal phases, identified in the bent-needle model, takes place under a conformational switch of the mesogens. For example, one can imagine a quasi-nematic to modulate-nematic transition induced by a sudden increase in the central-to-tail angle of the molecules at fixed temperature and density. This could be achieved experimentally by employing light-switchable mesogens. Indeed, recent experiments demonstrated the possibility to control liquid-crystal order with light [27], but the kinetics of the underlying process is still far from being understood. Computer simulation can clarify the dynamics of the light-induced transition at the molecular level, and our results indicate that kinetic Monte Carlo simulations are a reliable and powerful tool for these investigations.

Our study further illustrates the richness of structures, including supra-molecular organization, formed by self-assembling particles of different shapes in two dimensions. Additionally, as azobenzene-based material are attracting growing interest as light-tunable systems, our findings strongly suggest the possibility to change the monolayer dynamics by controlling the light-absorption properties of the molecules and their geometrical shapes. Being able to control molecular geometry thus offers the possibility of designing novel materials, in particular in two dimensions, and of tuning their properties accordingly.

# Appendix A

# Power-law birefringence relaxation

In this appendix we detail the calculation of the relaxation of the birefringence discussed in Sec. 3.4.2. In Ref. [1] the relaxation is interpreted as a process which happens against a distribution $f(U)$ of energy barriers. The birefringence $Q(t)$ is defined as

$$Q(t) = \int dU \exp[-t/\tau(U)] f(U)\,. \tag{A.1}$$

In the following we evaluate Eq. (A.1) under the assumption that the energetic barriers are distributed accordingly to a generalized Gumbel distribution

$$f(U) = \frac{\gamma}{U_m \Gamma(1/\gamma)} \exp\Big[ - U/U_m - \exp(-\gamma(U/U_m))\Big]\,, \tag{A.2}$$

where $U_m$ and $\gamma$ are distribution parameters and $\Gamma$ is the Euler gamma function. The characteristic time of a single $\tau$ environment is governed by the Arrhenius law

$$\tau(U) = \tau_t \exp(U/k_\mathrm{B}T)\,, \tag{A.3}$$

and $\tau_t$ is a characteristic time scale for molecular fluctuations.

The evaluation of Eq. (A.1) proceeds by changing variable in the time domain

$$Q(t) = \int dU \exp[-t/\tau(U)] f(U) = \int_0^\infty \exp[-t/\tau] H(\tau)\,\mathrm{d}\tau\,, \tag{A.4}$$

where $H(\tau) = f(U(\tau))|\mathrm{d}U/\mathrm{d}\tau|$. Using Eq. (A.3) one gets

$$f(U(\tau)) = \frac{\gamma}{U_m \Gamma(1/\gamma)} \big(\frac{\tau}{\tau_t}\big)^{-\eta} \exp[-\big(\frac{\tau}{\tau_t}\big)^{-\eta\gamma}]\,, \tag{A.5}$$

where we defined $U_m = k_\mathrm{B}T_m$ and $\eta = T/T_m$. Again from Eq. (A.3) we have $\mathrm{d}U/\mathrm{d}\tau = k_\mathrm{B}T/\tau$, thus

$$H(\tau) = \frac{\gamma\eta}{\Gamma(1/\gamma)} \frac{1}{\tau_t} \big(\frac{\tau_t}{t}\big)^{\eta+1} \exp[-\big(\tau_t/\tau\big)^{\eta\gamma}]\,. \tag{A.6}$$

Substituting Eq. (A.6) in Eq. (A.4) results in

$$Q(t) = \int_0^\infty \exp[-t/\tau] H(\tau)\,\mathrm{d}\tau = \frac{\gamma\eta}{\Gamma(1/\gamma)}\frac{1}{\tau_t}\underbrace{\int_0^\infty \exp[-t/\tau]\big(\frac{\tau_t}{t}\big)^{\eta+1}\exp[-\big(\tau_t/\tau\big)^{\eta\gamma}]}_{A} \quad \text{(A.7)}$$

It is convenient to expand the exponential $\exp[-t/\tau]$ in the integral $A$ as a power series

$$A = \int_0^\infty \exp[-t/\tau]\big(\frac{\tau_t}{t}\big)^{\eta+1}\exp[-\big(\tau_t/\tau\big)^{\eta\gamma}] = \sum_{n=0}^{\infty}\frac{1}{n!}\int_0^\infty (-t/\tau)^n\big(\frac{\tau_t}{t}\big)^{\eta+1}\exp[-\big(\tau_t/\tau\big)^{\eta\gamma}]\,. \quad \text{(A.8)}$$

Eq. (A.8) can be rewritten as

$$A = \sum_{n=0}^{\infty}\frac{1}{n!}(-\frac{t}{\tau_t})^n\underbrace{\int_0^\infty(-\frac{\tau_t}{\tau})^{n+\eta+1}\exp[-\big(\tau_t/\tau\big)^{\eta\gamma}]}_{B}\,. \quad \text{(A.9)}$$

where we multiplied everything by $(\tau_t/\tau_t)^n = 1$. We can now evaluate the integral $B$:

$$B = \int_0^\infty(-\frac{\tau_t}{\tau})^{n+\eta+1}\exp[-\big(\tau_t/\tau\big)^{\eta\gamma}]\,. \quad \text{(A.10)}$$

By introducing $y = (\tau_t/\tau)^{\eta\gamma}$ and changing variable, Eq. (A.10) becomes

$$B = \frac{\tau_t}{\eta\gamma}\int_0^\infty y^{\frac{1}{\eta\beta}(n+\eta)-1}e^{-y}\mathrm{d}y = \frac{\tau_t}{\eta\gamma}\Gamma\bigg(\frac{1}{\eta\gamma}(n+\eta)\bigg)\,. \quad \text{(A.11)}$$

Substituting Eq. (A.11) in Eq. (A.9), integral $A$ becomes

$$A = \sum_{n=0}^{\infty}\frac{1}{n!}(-\frac{t}{\tau_t})^n\frac{\tau_t}{\eta\gamma}\Gamma\bigg(\frac{1}{\eta\gamma}(n+\eta)\bigg)\,. \quad \text{(A.12)}$$

We can now go back to Eq. A.7 and substitute Eq. A.12, which gives

$$Q(t) = \sum_{n=0}^{\infty}\frac{1}{n!}(-\frac{t}{\tau_t})^n\frac{\Gamma\Big(\frac{1}{\eta\gamma}(n+\eta)\Big)}{\Gamma(1/\gamma)}\,. \quad \text{(A.13)}$$

Under the assumption $\eta = 1/\gamma$ and using the properties of the gamma functions, Eq. (A.13) can be rewritten as

$$Q(t) = \sum_{n=0}^{\infty}\frac{1}{n!}(-\frac{t}{\tau_t})^n\frac{\Gamma(n+\eta)}{\Gamma(\eta)} = \sum_{n=0}^{\infty}\frac{1}{n!}(-\frac{t}{\tau_t})^n\prod_{j=0}^{n-1}\bigg(\eta+j\bigg) \quad \text{(A.14)}$$

and it is easy to verify that Eq. (A.14) is the Taylor expansion of:

$$Q(t) = \frac{1}{(1+(\frac{t}{\tau_t}))^\eta} \quad \text{(A.15)}$$

which is exactly the expression for the birefringence relaxation used in Eq. (3.5) and in Ref. [1].

# List of Publications

A. Tavarone, R., Charbonneau, P. & Stark, H. Phase ordering of zig-zag and bow-shaped hard needles in two dimensions. *J. Chem. Phys.* **143,** 114505 (2015).

B. Tavarone, R., Charbonneau, P. & Stark, H. Kinetic Monte Carlo simulations for birefringence relaxation of photo-switchable molecules on a surface. *J. Chem. Phys.* **144,** 104703 (2016).

# Bibliography


1. Fang, G. *et al.* Athermal photofluidization of glasses. *Nat. Commun.* **4,** 1521 (2013).
2. Grier, D. G. A revolution in optical manipulation. *Nature* **424,** 810–816 (2003).
3. Hänggi, P. & Marchesoni, F. Artificial Brownian motors: Controlling transport on the nanoscale. *Rev. Mod. Phys.* **81,** 387 (2009).
4. Yan, R., Gargas, D. & Yang, P. Nanowire photonics. *Nat. Photonics* **3,** 569–576 (2009).
5. Craighead, H. Future lab-on-a-chip technologies for interrogating individual molecules. *Nature* **442,** 387–393 (2006).
6. Ritort, F. Single-molecule experiments in biological physics: methods and applications. *J. Phys. Condens. Mat.* **18,** R531 (2006).
7. Caruthers, S. D., Wickline, S. A. & Lanza, G. M. Nanotechnological applications in medicine. *Curr. Opin. Biotech.* **18,** 26–30 (2007).
8. Cao, H. *et al.* Fabrication of 10 nm enclosed nanofluidic channels. *Appl. Phys. Lett.* **81,** 174–176 (2002).
9. Ulman, A. *An Introduction to Ultrathin Organic Films: From Langmuir–Blodgett to Self–Assembly* (Academic press, 2013).
10. Schreiber, F. Self-assembled monolayers: from'simple'model systems to biofunctionalized interfaces. *J. Phys. - Condens. Mat.* **16,** R881 (2004).
11. Böker, A., He, J., Emrick, T. & Russell, T. P. Self-assembly of nanoparticles at interfaces. *Soft Matter* **3,** 1231–1248 (2007).
12. Barth, J. V., Costantini, G. & Kern, K. Engineering atomic and molecular nanostructures at surfaces. *Nature* **437,** 671–679 (2005).
13. Aswal, D., Lenfant, S, Guerin, D, Yakhmi, J. & Vuillaume, D. Self assembled monolayers on silicon for molecular electronics. *Anal. Chim. Acta* **568,** 84–108 (2006).
14. Hicks, J. & Petralli-Mallow, T. Nonlinear optics of chiral surface systems. *Appl. Phys. B* **68,** 589–593 (1999).
15. Mendes, P. M. Stimuli-responsive surfaces for bio-applications. *Chem. Soc. Rev.* **37,** 2512–2529 (2008).
16. Mulero, A. *Theory and simulation of hard-sphere fluids and related systems* (Springer Science & Business Media, 2008).
17. Haji-Akbari, A. *et al.* Disordered, quasicrystalline and crystalline phases of densely packed tetrahedra. *Nature* **462,** 773–777 (2009).

18. Shao, D. & Chen, S. Surface-plasmon-assisted nanoscale photolithography by polarized light. *Appl. Phys. Lett.* **86,** 253107 (2005).

19. Delaire, J. A. & Nakatani, K. Linear and nonlinear optical properties of photochromic molecules and materials. *Chem. Rev.* **100,** 1817–1846 (2000).

20. Xia, F., Zhu, Y., Feng, L. & Jiang, L. Smart responsive surfaces switching reversibly between super-hydrophobicity and super-hydrophilicity. *Soft Matter* **5,** 275–281 (2009).

21. Lee, S., Kang, H. S. & Park, J.-K. Directional photofluidization lithography: micro/nanostructural evolution by photofluidic motions of azobenzene materials. *Adv. Mater.* **24,** 2069–2103 (2012).

22. Riskin, M., Gutkin, V., Felner, I. & Willner, I. Photochemical and electrochemical encoding of erasable magnetic patterns. *Angew. Chem. Int. Edit.* **47,** 4416–4420 (2008).

23. Katz, E., Willner, B. & Willner, I. Light-controlled electron transfer reactions at photoisomerizable monolayer electrodes by means of electrostatic interactions: active interfaces for the amperometric transduction of recorded optical signals. *Biosens. Bioelectron.* **12,** 703–719 (1997).

24. Hore, M. J. & Composto, R. J. Nanorod self-assembly for tuning optical absorption. *ACS nano* **4,** 6941–6949 (2010).

25. Mclean, R. S., Huang, X., Khripin, C., Jagota, A. & Zheng, M. Controlled two-dimensional pattern of spontaneously aligned carbon nanotubes. *Nano Lett.* **6,** 55–60 (2006).

26. Slyusarenko, K., Constantin, D. & Davidson, P. A two-dimensional nematic phase of magnetic nanorods. *J. Chem. Phys.* **140,** 104904 (2014).

27. Kosa, T. *et al.* Light-induced liquid crystallinity. *Nature* **485,** 347–349 (2012).

28. Karageorgiev, P. *et al.* From anisotropic photo-fluidity towards nanomanipulation in the optical near-field. *Nat. Mater.* **4,** 699–703 (2005).

29. Fang, G. *et al.* Effect of Concentration on the Photo-Orientation and Relaxation Dynamics of Self-Assembled Monolayers of Mixtures of an Azobenzene-Based Triethoxysilane with Octyltriethoxysilane. *Langmuir* **27,** 3336–3342 (2011).

30. Fang, G. *et al.* Photo-reversible liquid crystal alignment using azobenzene-based self-assembled monolayers: comparison of the bare monolayer and liquid crystal reorientation dynamics. *Langmuir* **26,** 17482–17488 (2010).

31. Yaroshchuk, O. & Reznikov, Y. Photoalignment of liquid crystals: basics and current trends. *J. Mater. Chem.* **22,** 286–300 (2012).

32. Zhao, Y. & Ikeda, T. *Smart light-responsive materials: azobenzene-containing polymers and liquid crystals* (John Wiley & Sons, 2009).

33. Fournée, V. *et al.* Self-Organized Molecular Films with Long-Range Quasiperiodic Order. *ACS nano* **8,** 3646–3653 (2014).

34. Mikhael, J. *et al.* Proliferation of anomalous symmetries in colloidal monolayers subjected to quasiperiodic light fields. *Proc. Natl. Acad. Sci. U.S.A.* **107,** 7214–7218 (2010).

35. Schmiedeberg, M. & Stark, H. Colloidal ordering on a 2D quasicrystalline substrate. *Phys. Rev. Lett.* **101,** 218302 (2008).

36. Schmiedeberg, M. *et al.* Archimedean-like colloidal tilings on substrates with decagonal and tetradecagonal symmetry. *Eur. Phys. J. E* **32,** 25–34 (2010).

37. He, Y., Chen, Y., Liu, H., Ribbe, A. E. & Mao, C. Self-assembly of hexagonal DNA two-dimensional (2D) arrays. *J. Am. Chem. Soc.* **127,** 12202–12203 (2005).

38. Winfree, E., Liu, F., Wenzler, L. A. & Seeman, N. C. Design and self-assembly of two-dimensional DNA crystals. *Nature* **394,** 539–544 (1998).

39. Bai, Y. & Abbott, N. L. Recent advances in colloidal and interfacial phenomena involving liquid crystals. *Langmuir* **27,** 5719–5738 (2010).

40. De Jeu, W. H., Ostrovskii, B. I. & Shalaginov, A. N. Structure and fluctuations of smectic membranes. *Rev. Mod. Phys.* **75,** 181 (2003).

41. Muševič, I., Škarabot, M., Tkalec, U., Ravnik, M. & Žumer, S. Two-dimensional nematic colloidal crystals self-assembled by topological defects. *Science* **313,** 954–958 (2006).

42. Bates, M. & Frenkel, D. Phase behavior of two-dimensional hard rod fluids. *J. Chem. Phys.* **112,** 10034 (2000).

43. Ghosh, A. & Dhar, D. On the orientational ordering of long rods on a lattice. *Europhys. Lett.* **78,** 20003 (2007).

44. Kählitz, P. & Stark, H. Phase ordering of hard needles on a quasicrystalline substrate. *J. Chem. Phys.* **136,** 174705 (2012).

45. Donev, A., Burton, J., Stillinger, F. H. & Torquato, S. Tetratic order in the phase behavior of a hard-rectangle system. *Phys. Rev. B* **73,** 054109 (2006).

46. Martínez-Ratón, Y., Velasco, E. & Mederos, L. Effect of particle geometry on phase transitions in two-dimensional liquid crystals. *J. Chem. Phys.* **122,** 064903 (Feb. 2005).

47. Lagomarsino, M. C., Dogterom, M. & Dijkstra, M. Isotropic–nematic transition of long, thin, hard spherocylinders confined in a quasi-two-dimensional planar geometry. *J. Chem. Phys.* **119,** 3535–3540 (2003).

48. Kählitz, P., Schoen, M. & Stark, H. Clustering and mobility of hard rods in a quasicrystalline substrate potential. *J. Chem. Phys.* **137,** 224705 (2012).

49. Xu, W.-S., Li, Y.-W., Sun, Z.-Y. & An, L.-J. Hard ellipses: equation of state, structure, and self-diffusion. *J. Chem. Phys.* **139,** 024501 (2013).

50. Moradi, M, Hashemi, S & Taghizadeh, F. Monte Carlo simulation of a confined hard ellipse fluid. *Physica A* **389,** 4510–4519 (2010).

51. Peón, J. *et al.* Two-dimensional chiral model for liquid crystals, bent hard needles: a Monte Carlo simulation. *J. Chem. Phys.* **125,** 104908. ISSN: 0021-9606 (Sept. 2006).

52. Maiti, P. K., Lansac, Y., Glaser, M. A. & Clark, N. A. Entropy-stabilized smectic C phase in a system of zigzag-shaped molecules. *Phys. Rev. Lett.* **92,** 025501 (2004).

53. Martínez-González, J., Armas-Pérez, J. C. & Quintana-H, J. Phase Behavior of Bow-Shaped Hard Particles in Two Dimensions. *J. Stat. Phys.* **150,** 559–571 (Oct. 2012).

54. Mermin, N. D. Crystalline Order in Two Dimensions. *Phys. Rev.* **176,** 250–254 (1 1968).
55. Strandburg, K. J. Two-dimensional melting. *Rev. Mod. Phys.* **60,** 161 (1988).
56. Bernard, E. P. & Krauth, W. Two-step melting in two dimensions: First-order liquid-hexatic transition. *Phys. Rev. Lett.* **107,** 155704 (2011).
57. Dozov, I. On the spontaneous symmetry breaking in the mesophases of achiral banana-shaped molecules. *Europhys. Lett.* **56,** 247 (2001).
58. Borshch, V. *et al.* Nematic twist-bend phase with nanoscale modulation of molecular orientation. *Nat. Commun.* **4** (2013).
59. Memmer, R. Liquid crystal phases of achiral banana-shaped molecules: a computer simulation study. *Liq. Cryst.* **29,** 483–496 (2002).
60. Frenkel, D & Eppenga, R. Evidence for algebraic orientational order in a two-dimensional hard-core nematic. *Phys. Rev. A* (1985).
61. Vink, R. L. The isotropic-to-nematic transition in a two-dimensional fluid of hard needles: a finite-size scaling study. *Eur. Phys. J. B* **72,** 225–231 (Oct. 2009).
62. Armas-Pérez, J. C. & Quintana-H., J. Numerical evidence for nematic and smectic behavior of two-dimensional hard models. *Phys. Rev. E* **83,** 051709 (May 2011).
63. Varga, S., Gurin, P., Armas-Pérez, J. C. & Quintana-H, J. Nematic and smectic ordering in a system of two-dimensional hard zigzag particles. *J. Chem. Phys.* **131,** 184901 (Nov. 2009).
64. Battaile, C. C. The kinetic Monte Carlo method: Foundation, implementation, and application. *Comput. Method Appl. M* **197,** 3386–3398 (2008).
65. Berthier, L. Dynamic heterogeneity in amorphous materials. *Physics* **4,** 42 (2011).
66. Berthier, L. & Biroli, G. Theoretical perspective on the glass transition and amorphous materials. *Rev. Mod. Phys.* **83,** 587 (2011).
67. Prost, J & De Gennes, P. *The physics of liquid crystals* (Oxford university press, 1993).
68. Collings, P. J. & Patel, J. *Handbook of liquid crystal research* (Oxford University Press, 1997).
69. Friedel, G. *The mesomorphic states of matter* in *Ann. Phys. Paris* **18** (1922), 273.
70. Reinitzer, F. Beiträge zur kenntniss des cholesterins. *Monatsh. Chem.* **9,** 421–441 (1888).
71. Vertogen, G. & Jeu, W. H. *Thermotropic liquid crystals, fundamentals* (Springer, 1988).
72. Ciferri, A. *Polymer liquid crystals* (Elsevier, 2012).
73. Chandrasekhar, S. Discotic liquid crystals. A brief review. *Liq. Cryst.* **14,** 3–14 (1993).
74. Pershan, P. *Structure of Liquid Crystal Phases* (World Scientific, 1988).
75. Kitzerow, H. & Bahr, C. *Chirality in liquid crystals* (Springer Science & Business Media, 2001).

76. Lubensky, T., Harris, A., Kamien, R. D. & Yan, G. Chirality in liquid crystals: From microscopic origins to macroscopic structure. *Ferroelectrics* **212,** 1–20 (1998).

77. Wright, D. C. & Mermin, N. D. Crystalline liquids: the blue phases. *Rev. Mod. Phys.* **61,** 385 (1989).

78. Goodby, J. W. Twist grain boundary and frustrated liquid crystal phases. *Curr. Opin. Colloid In.* **7,** 326–332 (2002).

79. Dierking, I. A review of textures of the TGBA* phase under different anchoring geometries. *Liq. Cryst.* **26,** 83–95 (1999).

80. Pelzl, G., Diele, S. & Weissflog, W. Banana-Shaped Compounds—A New Field of Liquid Crystals. *Adv. Mater.* **11,** 707–724 (1999).

81. Ros, M. B., Serrano, J. L., de La Fuente, M. R. & Folcia, C. L. Banana-shaped liquid crystals: a new field to explore. *J. Mater. Chem.* **15,** 5093–5098 (2005).

82. Matsuzaki, H. & Matsunaga, Y. New mesogenic compounds with unconventional molecular structures 1, 2-phenylene and 2, 3-naphthylene bis [4-(4-alkoxyphenyliminomethyl) benzoates] and related compounds. *Liq. Cryst.* **14,** 105–120 (1993).

83. Cladis, P. & Brand, H. R. Electrooptic response of smectic O and smectic O. *Liq. Cryst.* **14,** 1327–1349 (1993).

84. Niori, T., Sekine, T, Watanabe, J, Furukawa, T & Takezoe, H. Distinct ferroelectric smectic liquid crystals consisting of banana shaped achiral molecules. *J. Mater. Chem.* **6,** 1231–1233 (1996).

85. Araoka, F. *et al.* Twist-Grain-Boundary Structure in the B 4 Phase of a Bent-Core Molecular System Identified by Second Harmonic Generation Circular Dichroism Measurement. *Phys. Rev. Lett.* **94,** 137801 (2005).

86. Chen, D. *et al.* Chiral heliconical ground state of nanoscale pitch in a nematic liquid crystal of achiral molecular dimers. *P. Natl. Acad. Sci. USA* **110,** 15931–15936 (2013).

87. Das, S. & Davis, R. Photoresponsive Liquid Crystals. *P. Indian Acad. Sci. A* **69,** 109–122 (2003).

88. Ikeda, T. Photomodulation of liquid crystal orientations for photonic applications. *J. Mater. Chem.* **13,** 2037–2057 (2003).

89. Majumdar, A., Cristina, M. M. & Virga, E. G. Perspectives in active liquid crystals. *Philos. T. Roy. Soc. A* **372,** 20130373 (2014).

90. Giomi, L., Bowick, M. J., Mishra, P., Sknepnek, R. & Marchetti, M. C. Defect dynamics in active nematics. *Philos. T. Roy. Soc. A* **372,** 20130365 (2014).

91. Marenduzzo, D, Orlandini, E & Yeomans, J. Hydrodynamics and rheology of active liquid crystals: A numerical investigation. *Phys. Rev. Lett.* **98,** 118102 (2007).

92. Onsager, L. The effects of shape on the interaction of colloidal particles. *Ann. NY Acad. Sci.* **51,** 627–659 (1949).

93. Hansen, J.-P. & McDonald, I. R. *Theory of simple liquids* (Elsevier, 1990).

94. Maier, W. & Saupe, A. Eine einfache molekulare Theorie des nematischen kristallinflüssigen Zustandes. *Z. Naturforsch. A* **13,** 564–566 (1958).

95. Vertogen, G. & de Jeu, W. H. *Thermotropic liquid crystals, fundamentals* (Springer Science & Business Media, 2012).
96. Frank, F. C. I. Liquid crystals. On the theory of liquid crystals. *Discuss. Faraday Soc.* **25,** 19–28 (1958).
97. Oseen, C. The theory of liquid crystals. *T. Faraday Soc.* **29,** 883–899 (1933).
98. Zocher, H. The effect of a magnetic field on the nematic state. *T. Faraday Soc.* **29,** 945–957 (1933).
99. Stark, H. Physics of colloidal dispersions in nematic liquid crystals. *Phys. Rep.* **351,** 387–474 (2001).
100. Srivastava, A. & Singh, S. Elastic constants of nematic liquid crystals of uniaxial symmetry. *J. Phys. Condens. Mat.* **16,** 7169 (2004).
101. Allen, M. P. & Frenkel, D. Calculation of liquid-crystal Frank constants by computer simulation. *Phys. Rev. A* **37,** 1813 (1988).
102. Cleaver, D. J. & Allen, M. P. Computer simulations of the elastic properties of liquid crystals. *Phys. Rev. A* **43,** 1918 (1991).
103. Allen, M. P., Warren, M. A., Wilson, M. R., Sauron, A. & Smith, W. Molecular dynamics calculation of elastic constants in Gay–Berne nematic liquid crystals. *J. Chem. Phys.* **105,** 2850–2858 (1996).
104. Elston, S. & Sambles, R. *The optics of thermotropic liquid crystals* (Taylor & Francis, 1998).
105. Saleh, B. E., Teich, M. C. & Saleh, B. E. *Fundamentals of photonics* (Wiley New York, 1991).
106. Bower, D. I. *An introduction to polymer physics* (Cambridge University Press, 2002).
107. Mukai, H, Fernandes, P., De Oliveira, B. & Dias, G. Defect-antidefect correlations in a lyotropic liquid crystal from a cosmological point of view. *Phys. Rev. E* **75,** 061704 (2007).
108. Nehring, J. & Saupe, A. On the schlieren texture in nematic and smectic liquid crystals. *J. Chem. Soc. Farad. T. 2* **68,** 1–15 (1972).
109. Mermin, N. D. The topological theory of defects in ordered media. *Rev. Mod. Phys.* **51,** 591 (1979).
110. Toulouse, G & Kléman, M. Principles of a classification of defects in ordered media. *J. Phys. Lett. Paris* **37,** 149–151 (1976).
111. Kroner, E & Anthony, K. Dislocations and disclinations in material structures: The basic topological concepts. *Ann. Rev. Mater. Sci.* **5,** 43–72 (1975).
112. Trebin, H.-R. The topology of non-uniform media in condensed matter physics. *Adv. Phys.* **31,** 195–254 (1982).
113. Kleman, M. & Friedel, J. Disclinations, dislocations, and continuous defects: A reappraisal. *Rev. Mod. Phys.* **80,** 61 (2008).
114. Kléman, M. Defects in liquid crystals. *Rep. Prog. Phys.* **52,** 555 (1989).
115. Chandrasekhar, S & Ranganath, G. The structure and energetics of defects in liquid crystals. *Adv. Phys.* **35,** 507–596 (1986).

116. Lavrentovich, O., Pasini, P., Zannoni, C. & Zumer, S. *Defects in liquid crystals: Computer simulations, theory and experiments* (Springer Science & Business Media, 2012).

117. Michel, L. Symmetry defects and broken symmetry. Configurations hidden symmetry. *Rev. Mod. Phys.* **52,** 617 (1980).

118. Kosterlitz, J. M. & Thouless, D. J. Ordering, metastability and phase transitions in two-dimensional systems. *J. Phys. C Solid State* **6,** 1181 (1973).

119. Halperin, B. & Nelson, D. R. Theory of two-dimensional melting. *Phys. Rev. Lett.* **41,** 121 (1978).

120. Abrikosov, A. The magnetic properties of superconducting alloys. *J. Phys. Chem. Solid* **2,** 199–208 (1957).

121. Renn, S. R. & Lubensky, T. C. Abrikosov dislocation lattice in a model of the cholesteric–to–smectic-A transition. *Phys. Rev. A* **38,** 2132 (1988).

122. Owczarek, R. Topological defects in superfluid Helium. *Int. J. Theor. Phys.* **30,** 1605–1612 (1991).

123. Salomaa, M. & Volovik, G. Quantized vortices in superfluid He 3. *Rev. Mod. Phys.* **59,** 533 (1987).

124. Rey, A. D. Liquid crystal models of biological materials and processes. *Soft Matter* **6,** 3402–3429 (2010).

125. Chuang, I., Durrer, R., Turok, N. & Yurke, B. Cosmology in the laboratory: Defect dynamics in liquid crystals. *Science* **251,** 1336–1342 (1991).

126. Trebin, H.-R. Defects in liquid crystals and cosmology. *Liq. Cryst.* **24,** 127–130 (1998).

127. Turok, N. Global texture as the origin of cosmic structure. *Phys. Rev. Lett.* **63,** 2625 (1989).

128. Mermin, N. D. & Wagner, H. Absence of ferromagnetism or antiferromagnetism in one-or two-dimensional isotropic Heisenberg models. *Phys. Rev. Lett.* **17,** 1133 (1966).

129. José, J. V., Kadanoff, L. P., Kirkpatrick, S. & Nelson, D. R. Renormalization, vortices, and symmetry-breaking perturbations in the two-dimensional planar model. *Phys. Rev. B* **16,** 1217 (1977).

130. Chaikin, P. M. & Lubensky, T. C. *Principles of condensed matter physics* (Cambridge Univ Press, 2000).

131. Bruno, P. Absence of spontaneous magnetic order at nonzero temperature in one- and two-dimensional Heisenberg and XY systems with long-range interactions. *Phys. Rev. Lett.* **87,** 137203 (2001).

132. Straley, J. Liquid crystals in two dimensions. *Phys. Rev. A* **4,** 675 (1971).

133. Timling, K. Scaled-particle theory of two-dimensional anisotropic fluids. *Philips. Res. Rep.* **25,** 223 (1970).

134. Kayser Jr, R. F. & Raveché, H. J. Bifurcation in Onsager's model of the isotropic-nematic transition. *Phys. Rev. A* **17,** 2067 (1978).

135. Nelson, D. R. & Pelcovits, R. A. Momentum-shell recursion relations, anisotropic spins, and liquid crystals in 2+ $\varepsilon$ dimensions. *Phys. Rev. B* **16,** 2191–2199 (1977).

136. Resnick, D., Garland, J., Boyd, J., Shoemaker, S & Newrock, R. Kosterlitz-Thouless transition in proximity-coupled superconducting arrays. *Phys. Rev. Lett.* **47,** 1542 (1981).

137. Leemann, C., Lerch, P., Racine, G.-A. & Martinoli, P. Vortex dynamics and phase transitions in a two-dimensional array of Josephson junctions. *Phys. Rev. Lett.* **56,** 1291 (1986).

138. Bishop, D. & Reppy, J. Study of the Superfluid Transition in Two-Dimensional He 4 Films. *Phys. Rev. Lett.* **40,** 1727 (1978).

139. Schweikhard, V, Tung, S & Cornell, E. Vortex proliferation in the Berezinskii-Kosterlitz-Thouless regime on a two-dimensional lattice of Bose-Einstein condensates. *Phys. Rev. Lett.* **99,** 030401 (2007).

140. Hadzibabic, Z., Krüger, P., Cheneau, M., Battelier, B. & Dalibard, J. Berezinskii–Kosterlitz–Thouless crossover in a trapped atomic gas. *Nature* **441,** 1118–1121 (2006).

141. Nelson, D. R. & Halperin, B. Dislocation-mediated melting in two dimensions. *Phys. Rev. B* **19,** 2457 (1979).

142. Cuesta, J. & Frenkel, D. Monte Carlo simulation of two-dimensional hard ellipses. *Phys. Rev. A* **42,** 2126 (1990).

143. Van Enter, A. C. & Shlosman, S. B. First-order transitions for n-vector models in two and more dimensions: Rigorous proof. *Phys. Rev. Lett.* **89,** 285702 (2002).

144. Vink, R. Liquid crystals in two dimensions: First-order phase transitions and nonuniversal critical behavior. *Phys. Rev. Lett.* **98,** 217801 (2007).

145. Vink, R. L. Crossover from a Kosterlitz-Thouless phase transition to a discontinuous phase transition in two-dimensional liquid crystals. *Phys. Rev. E* **90,** 062132 (2014).

146. Helfrich, W. Defect model of the smectic A-nematic phase transition. *J. Phys. Paris* **39,** 1199–1208 (1978).

147. Day, A. R., Lubensky, T. & McKane, A. Dislocations and the nematic—to—smectic-A transition for arbitrary values of K 1. *Phys. Rev. A* **27,** 1461 (1983).

148. Moreau, P *et al.* Dislocation-loop-mediated smectic melting. *Europhys. Lett.* **73,** 49 (2006).

149. Toner, J. & Nelson, D. R. Smectic, cholesteric, and Rayleigh-Benard order in two dimensions. *Phys. Rev. B* **23,** 316 (1981).

150. Lagerwall, J. P. & Giesselmann, F. Current topics in smectic liquid crystal research. *ChemPhysChem* **7,** 20–45 (2006).

151. Kuczyński, W & Stegemeyer, H. Ferroelectric properties of smectic C liquid crystals with induced helical structure. *Chem. Phys. Lett.* **70,** 123–126 (1980).

152. Link, D. R. *et al.* Spontaneous formation of macroscopic chiral domains in a fluid smectic phase of achiral molecules. *Science* **278,** 1924–1927 (1997).

153. Madsen, L. A., Dingemans, T. J., Nakata, M. & Samulski, E. T. Thermotropic biaxial nematic liquid crystals. *Phys. Rev. Lett.* **92,** 145505 (2004).

154. Eremin, A *et al.* Experimental evidence for an achiral orthogonal biaxial smectic phase without in-plane order exhibiting antiferroelectric switching behavior. *Phys. Rev. E* **64,** 051707 (2001).

155. Camp, P. J., Allen, M. P. & Masters, A. J. Theory and computer simulation of bent-core molecules. *J. Chem. Phys.* **111,** 9871–9881 (1999).

156. Lansac, Y., Maiti, P. K., Clark, N. A. & Glaser, M. A. Phase behavior of bent-core molecules. *Phys. Rev. E* **67,** 011703 (2003).

157. Meyer, R. B. Piezoelectric effects in liquid crystals. *Phys. Rev. Lett.* **22,** 918 (1969).

158. Harden, J. *et al.* Giant flexoelectricity of bent-core nematic liquid crystals. *Phys. Rev. Lett.* **97,** 157802 (2006).

159. Landau, L. D. & Lifshitz, E. M. *Course of theoretical physics, Vol. 5* (Elsevier, 2013).

160. Polson, J. & Frenkel, D. First-order nematic-smectic phase transition for hard spherocylinders in the limit of infinite aspect ratio. *Phys. Rev. E* **56,** R6260–R6263. ISSN: 1063-651X (Dec. 1997).

161. Katsonis, N., Lubomska, M., Pollard, M. M., Feringa, B. L. & Rudolf, P. Synthetic light-activated molecular switches and motors on surfaces. *Prog. Surf. Sci.* **82,** 407–434 (2007).

162. Sekkat, Z. & Knoll, W. *Photoreactive organic thin films* (Academic Press, 2002).

163. Balzani, V., Credi, A., Marchioni, F. & Stoddart, J. F. Artificial molecular-level machines. Dethreading–rethreading of a pseudorotaxane powered exclusively by light energy. *Chem. Commun.* 1860–1861 (2001).

164. Tsuchiya, S. Intramolecular electron transfer of diporphyrins comprised of electron-deficient porphyrin and electron-rich porphyrin with photocontrolled isomerization. *J. Chem. Soc.* **121,** 48–53 (1999).

165. Higuchi, M., Minoura, N. & Kinoshita, T. Photocontrol of Micellar Structure of an Azobenzene Containing Amphiphilic Sequential Polypeptide. *Chem. Lett.* **23,** 227–230 (1994).

166. Liu, X.-M., Yang, B., Wang, Y.-L. & Wang, J.-Y. New nanoscale pulsatile drug delivery system. *Chem. Lett.* **17,** 2792–2795 (2005).

167. Willner, I. & Rubin, S. Control of the structure and functions of biomaterials by light. *Angew. Chem. Int. Edit.* **35,** 367–385 (1996).

168. Renner, C. & Moroder, L. Azobenzene as conformational switch in model peptides. *ChemBioChem* **7,** 868–878 (2006).

169. Bartels, E., Wassermann, N. H. & Erlanger, B. F. Photochromic activators of the acetylcholine receptor. *P. Natl. Acad. Sci. USA* **68,** 1820–1823 (1971).

170. Yavlovich, A., Smith, B., Gupta, K., Blumenthal, R. & Puri, A. Light-sensitive lipid-based nanoparticles for drug delivery: design principles and future considerations for biological applications. *Mol. Membr. Biol.* **27,** 364–381 (2010).

171. Karthaus, O., Shimomura, M., Hioki, M., Tahara, R. & Nakamura, H. Reversible photomorphism in surface monolayers. *J. Am. Chem. Soc.* **118,** 9174–9175 (1996).

172. Shin, J. Y. & Abbott, N. L. Using light to control dynamic surface tensions of aqueous solutions of water soluble surfactants. *Langmuir* **15,** 4404–4410 (1999).

173. Ichimura, K., Oh, S.-K. & Nakagawa, M. Light-driven motion of liquids on a photoresponsive surface. *Science* **288,** 1624–1626 (2000).

174. Eastoe, J. & Vesperinas, A. Self-assembly of light-sensitive surfactants. *Soft Matter* **1,** 338–347 (2005).

175. Diguet, A. *et al.* Photomanipulation of a Droplet by the Chromocapillary Effect. *Angew. Chem. Int. Edit.* **121,** 9445–9448 (2009).

176. Schmitt, M. & Stark, H. Marangoni flow at droplet interfaces: Three-dimensional solution and applications. *Phys. Fluids* **28,** 012106 (2016).

177. Rosario, R. *et al.* Photon-modulated wettability changes on spiropyran-coated surfaces. *Langmuir* **18,** 8062–8069 (2002).

178. Van Delden, R. A. *et al.* Unidirectional molecular motor on a gold surface. *Nature* **437,** 1337–1340 (2005).

179. Kronemeijer, A. J. *et al.* Reversible conductance switching in molecular devices. *Adv. Mater.* **20,** 1467–1473 (2008).

180. Kim, D., Tripathy, S., Li, L. & Kumar, J. Laser-induced holographic surface relief gratings on nonlinear optical polymer films. *Appl. Phys. Lett.* **66,** 1166–1168 (1995).

181. Lee, S., Shin, J., Kang, H. S., Lee, Y.-H. & Park, J.-K. Deterministic nanotexturing by directional photofluidization lithography. *Adv. Mater.* **23,** 3244–3250 (2011).

182. Ichimura, K. Photoalignment of liquid-crystal systems. *Chem. Rev.* **100,** 1847–1874 (2000).

183. Norikane, Y., Hirai, Y. & Yoshida, M. Photoinduced isothermal phase transitions of liquid-crystalline macrocyclic azobenzenes. *Chem. Commun.* **47,** 1770–1772 (2011).

184. Marrucci, L & Paparo, D. Photoinduced molecular reorientation of absorbing liquid crystals. *Phys. Rev. E* **56,** 1765 (1997).

185. Mahimwalla, Z. *et al.* Azobenzene photomechanics: prospects and potential applications. *Polym. Bull.* **69,** 967–1006 (2012).

186. Brown, C. J. A refinement of the crystal structure of azobenzene. *Acta Crystallogr.* **21,** 146–152 (1966).

187. Naito, T., Horie, K. & Mita, I. Photochemistry in polymer solids: 12. Effects of main-chain structures and formation of hydrogen bonds on photoisomerization of azobenzene in various polymer films. *Polymer* **34,** 4140–4145 (1993).

188. Cusati, T., Granucci, G. & Persico, M. Photodynamics and time-resolved fluorescence of azobenzene in solution: a mixed quantum-classical simulation. *J. Am. Chem. Soc.* **133,** 5109–5123 (2011).

189. Wang, Y. *et al.* Dynamic studies of degenerate four-wave-mixing in an azobenzene-doped polymer film with an optical pump. *J. Chem. Phys.* **103,** 5357–5361 (1995).

190. Brzozowski, L. & Sargent, E. H. Azobenzenes for photonic network applications: Third-order nonlinear optical properties. *J. Mater. Sci.: Mater. El.* **12,** 483–489 (2001).

191. Tiberio, G., Muccioli, L., Berardi, R. & Zannoni, C. How does the trans–cis photoisomerization of azobenzene take place in organic solvents? *ChemPhysChem* **11,** 1018–1028 (2010).

192. Simoni, F & Francescangeli, O. Effects of light on molecular orientation of liquid crystals. *J. Phys. Condens. Mat.* **11,** R439 (1999).

193. Freedericksz, V. & Zolina, V. Forces causing the orientation of an anisotropic liquid. *Trans. Faraday Soc.* **29,** 919–930 (1933).

194. Janossy, I, Lloyd, A. & Wherrett, B. Anomalous optical Freedericksz transition in an absorbing liquid crystal. *Mol. Cryst. Liq. Cryst.* **179,** 1–12 (1990).

195. Jánossy, I. Molecular interpretation of the absorption-induced optical reorientation of nematic liquid crystals. *Phys. Rev. E* **49,** 2957 (1994).

196. Janossy, I & Szabados, L. Optical reorientation of nematic liquid crystals in the presence of photoisomerization. *Phys. Rev. E* **58,** 4598 (1998).

197. Sekkat, Z., Wood, J. & Knoll, W. Reorientation mechanism of azobenzenes within the trans. fwdarw. cis photoisomerization. *J. Phys. Chem.* **99,** 17226–17234 (1995).

198. Marrucci, L *et al.* Role of guest-host intermolecular forces in photoinduced reorientation of dyed liquid crystals. *J. Chem Phys.* **107,** 9783–9793 (1997).

199. Yager, K. G. & Barrett, C. J. Novel photo-switching using azobenzene functional materials. *J. Photoch. Photobio. A* **182,** 250–261 (2006).

200. Pedersen, T. G., Ramanujam, P., Johansen, P. M. & Hvilsted, S. Quantum theory and experimental studies of absorption spectra and photoisomerization of azobenzene polymers. *JOSA B* **15,** 2721–2730 (1998).

201. Kiselev, A. Kinetics of photoinduced anisotropy in azopolymers: models and mechanisms. *J. Phys. Condens. Matter* **14,** 13417 (2002).

202. Yi, Y., Farrow, M. J., Korblova, E., Walba, D. M. & Furtak, T. E. High-sensitivity aminoazobenzene chemisorbed monolayers for photoalignment of liquid crystals. *Langmuir* **25,** 997–1003 (2008).

203. Chigrinov, V. *et al.* Diffusion model of photoaligning in azo-dye layers. *Phys. Rev. E* **69,** 061713 (2004).

204. Yi, Y. *et al.* Dynamics of cis isomers in highly sensitive amino-azobenzene monolayers: The effect of slow relaxation on photo-induced anisotropy. *J. Appl. Phys* **109,** 103521 (2011).

205. Shlesinger, M. F. Fractal time in condensed matter. *Annu. Rev. Phys. Chem.* **39,** 269–290 (1988).

206. Metzler, R. & Klafter, J. From stretched exponential to inverse power-law: fractional dynamics, Cole–Cole relaxation processes, and beyond. *J. Non-Cryst. Solids* **305,** 81–87 (2002).

207. Vainstein, M. H., Costa, I. V., Morgado, R. & Oliveira, F. A. Non-exponential relaxation for anomalous diffusion. *Europhys. Lett.* **73,** 726 (2006).

208. Böhmer, R., Ngai, K., Angell, C. & Plazek, D. Nonexponential relaxations in strong and fragile glass formers. *J. Chem. Phys.* **99,** 4201–4209 (1993).

209. Phillips, J. Stretched exponential relaxation in molecular and electronic glasses. *Rep. Prog. Phys.* **59,** 1133 (1996).

210. Kohlrausch, R. Ueber das Dellmann'sche elektrometer. *Ann. Phys. Berlin* **148,** 353–405 (1847).

211. Williams, G. & Watts, D. C. Non-symmetrical dielectric relaxation behaviour arising from a simple empirical decay function. *T. Faraday Soc.* **66,** 80–85 (1970).

212. Legrand, D., Olszewski, W. & Bendler, J. Anelastic response of bisphenol-A polycarbonate. *J. Polym. Sci. Pol. Phys.* **25,** 1149–1152 (1987).

213. Rubí, J., Santamaría-Holek, I & Pérez-Madrid, A. Slow dynamics and local quasi-equilibrium—relaxation in supercooled colloidal systems. *J. Phys. Condens. Mat.* **16,** S2047 (2004).

214. Colaiori, F. & Moore, M. Stretched exponential relaxation in the mode-coupling theory for the Kardar-Parisi-Zhang equation. *Phys. Rev. E* **63,** 057103 (2001).

215. Angell, C. A., Ngai, K. L., McKenna, G. B., McMillan, P. F. & Martin, S. W. Relaxation in glassforming liquids and amorphous solids. *J. Appl. Phys.* **88,** 3113–3157 (2000).

216. Kob, W., Donati, C., Plimpton, S. J., Poole, P. H. & Glotzer, S. C. Dynamical heterogeneities in a supercooled Lennard-Jones liquid. *Phys. Rev. Lett.* **79,** 2827 (1997).

217. Coles, S., Bawa, J., Trenner, L. & Dorazio, P. *An introduction to statistical modeling of extreme values* (Springer, 2001).

218. Bertin, E. Global fluctuations and Gumbel statistics. *Phys. Rev. Lett.* **95,** 170601 (2005).

219. Bramwell, S. *et al.* Universal fluctuations in correlated systems. *Phys. Rev. Lett.* **84,** 3744 (2000).

220. Chaudhuri, P., Berthier, L. & Kob, W. Universal nature of particle displacements close to glass and jamming transitions. *Phys. Rev. Lett.* **99,** 060604 (2007).

221. Starr, F. W., Douglas, J. F. & Sastry, S. The relationship of dynamical heterogeneity to the Adam-Gibbs and random first-order transition theories of glass formation. *J. Chem. Phys.* **138,** 12A541 (2013).

222. Cavagna, A. Supercooled liquids for pedestrians. *Phys. Rep.* **476,** 51–124 (2009).

223. Shell, M. S., Debenedetti, P. G. & Stillinger, F. H. Dynamic heterogeneity and non-Gaussian behaviour in a model supercooled liquid. *J. Phys. Condens. Mat.* **17,** S4035 (2005).

224. Xia, X. & Wolynes, P. G. Microscopic theory of heterogeneity and nonexponential relaxations in supercooled liquids. *Phys. Rev. Lett.* **86,** 5526 (2001).

225. Sengupta, S., Karmakar, S., Dasgupta, C. & Sastry, S. Breakdown of the Stokes-Einstein relation in two, three, and four dimensions. *J. Chem. Phys.* **138,** 12A548 (2013).

226. Weeks, E. R., Crocker, J. C., Levitt, A. C., Schofield, A. & Weitz, D. A. Three-dimensional direct imaging of structural relaxation near the colloidal glass transition. *Science* **287,** 627–631 (2000).

227. Zheng, Z. *et al.* Structural signatures of dynamic heterogeneities in monolayers of colloidal ellipsoids. *Nat. Commun.* **5** (2014).

228. Mishra, C. K. & Ganapathy, R. Shape of Dynamical Heterogeneities and Fractional Stokes-Einstein and Stokes-Einstein-Debye Relations in Quasi-Two-Dimensional Suspensions of Colloidal Ellipsoids. *Phys. Rev. Lett.* **114,** 198302 (2015).

229. Frenkel, D. & Smit, B. *Understanding molecular simulation: from algorithms to applications* (Academic press, 2001).

230. Tuckerman, M. *Statistical mechanics: theory and molecular simulation* (Oxford University Press, 2010).

231. Metropolis, N., Rosenbluth, A. W., Rosenbluth, M. N., Teller, A. H. & Teller, E. Equation of state calculations by fast computing machines. *J. Chem. Phys.* **21,** 1087–1092 (1953).

232. Wang, J. & Swendsen, R. Cluster Monte Carlo Algorithms. *Physica A* **167,** 565–579 (1990).

233. Dressts, C. & Krauth, W. Cluster algorithm for hard spheres and related systems. *J. Phys. A-Math. Gen.* **28,** L597–L601 (1995).

234. Whitelam, S. & Geissler, P. L. Avoiding unphysical kinetic traps in Monte Carlo simulations of strongly attractive particles. *J. Chem. Phys.* **127,** 154101 (2007).

235. Wu, D., Chandler, D. & Smit, B. Electrostatic Analogy for Surfactant Assemblies. *J. Phys. Chem.* **96,** 4077–4083 (1992).

236. Fichthorn, K. A. & Weinberg, W. H. Theoretical foundations of dynamical Monte Carlo simulations. *J. Chem. Phys.* **95,** 1090–1096 (1991).

237. Patti, A. & Cuetos, A. Brownian dynamics and dynamic Monte Carlo simulations of isotropic and liquid crystal phases of anisotropic colloidal particles: A comparative study. *Phys. Rev. E* **86,** 011403 (2012).

238. Patti, A., El Masri, D., van Roij, R. & Dijkstra, M. Stringlike clusters and cooperative interlayer permeation in smectic liquid crystals formed by colloidal rods. *Phys. Rev. Lett.* **103,** 248304 (2009).

239. Belli, S., Patti, A., van Roij, R. & Dijkstra, M. Heterogeneous dynamics in columnar liquid crystals of parallel hard rods. *J. Chem. Phys.* **133,** 154514 (2010).

240. Berthier, L. & Kob, W. The Monte Carlo dynamics of a binary Lennard-Jones glass-forming mixture. *J. Phys. Condens. Mat.* **19,** 205130 (2007).

241. Pfleiderer, P., Milinkovic, K. & Schilling, T. Glassy dynamics in monodisperse hard ellipsoids. *Europhys. Lett.* **84,** 16003 (2008).

242. Auer, S. & Frenkel, D. Prediction of absolute crystal-nucleation rate in hard-sphere colloids. *Nature* **409,** 1020–1023 (2001).

243. Chern, S.-S., Cardenas, A. E. & Coalson, R. D. Three-dimensional dynamic Monte Carlo simulations of driven polymer transport through a hole in a wall. *J. Chem. Phys.* **115,** 7772–7782 (2001).

244. Huang, J., Wang, Y. & Qian, C. Simulation study on the formation of vesicle and influence of solvent. *J. Chem. Phys.* **131,** 234902 (2009).

245. Kotrla, M. Numerical simulations in the theory of crystal growth. *Comput. Phys. Commun.* **97,** 82–100 (1996).

246. Gilmer, G., Huang, H. & Roland, C. Thin film deposition: fundamentals and modeling. *Comp. Mater. Sci.* **12,** 354–380 (1998).

247. Battaile, C. in *Handbook of Materials Modeling* 2363–2377 (Springer, 2005).

248. Perusquía, R. A., Peón, J. & Quintana, J. Two-dimensional model for mixtures of enantiomers, bent hard needles: a Monte Carlo simulation. *Physica A* **345,** 130–142 (Jan. 2005).

249. Miller, M., Amon, L. & Reinhardt, W. Should one adjust the maximum step size in a Metropolis Monte Carlo simulation? *Chem. Phys. Lett.* **331,** 278–284 (2000).

250. Martínez-González, J., Varga, S, Gurin, P & Quintana-H, J. Structural properties of hockey stick-shaped particles in two dimensions. *J. Mol. Liq.* **185,** 26–31 (2013).

251. Bisi, F., Rosso, R., Virga, E. & Durand, G. Polar steric interactions for V-shaped molecules. *Phys. Rev. E* **78,** 011705 (July 2008).

252. Statman, D & Janossy, I. Study of photoisomerization of azo dyes in liquid crystals. *J. Chem. Phys.* **118,** 3222–3232 (2003).

253. Kiselev, A. D., Chigrinov, V. G. & Kwok, H.-S. Kinetics of photoinduced ordering in azo-dye films: Two-state and diffusion models. *Phys. Rev. E* **80,** 011706 (2009).

254. Sanz, E & Marenduzzo, D. Dynamic Monte Carlo versus Brownian dynamics: A comparison for self-diffusion and crystallization in colloidal fluids. *J. Chem. Phys.* **132,** 194102 (2010).

255. Löwen, H. Brownian dynamics of hard spherocylinders. *Phys. Rev. E* **50,** 1232 (1994).

256. Bevington, P. R. & Robinson, D. K. *Data Reduction and Error Analysis for the Physical Sciences* (McGraw–Hill, New York, 2003).

257. Franz, S. & Parisi, G. On non-linear susceptibility in supercooled liquids. *J. Phys. Condens. Mat.* **12,** 6335 (2000).

258. Kawasaki, T. & Tanaka, H. Structural signature of slow dynamics and dynamic heterogeneity in two-dimensional colloidal liquids: glassy structural order. *J. Phys. Condens. Matt.* **23,** 194121 (2011).

259. Zheng, Z., Wang, F. & Han, Y. Glass transitions in quasi-two-dimensional suspensions of colloidal ellipsoids. *Phys. Rev. Lett.* **107,** 065702 (2011).

260. Hurley, M. & Harrowell, P. Kinetic structure of a two-dimensional liquid. *Phys. Rev. E* **52,** 1694 (1995).

261. Teboul, V, Accary, J.-B. & Chrysos, M. Isomerization of azobenzene and the enhancement of dynamic heterogeneities in molecular glass formers. *Phys. Rev. E* **87,** 032309 (2013).

262. Teboul, V, Saiddine, M. & Nunzi, J.-M. Isomerization-Induced Dynamic Heterogeneity in a Glass Former below and above Tg. *Phys. Rev. Lett.* **103,** 265701 (2009).

263. Teboul, V, Saiddine, M, Nunzi, J.-M. & Accary, J.-B. An isomerization-induced cage-breaking process in a molecular glass former below Tg. *J. Chem. Phys.* **134,** 114517 (2011).

264. Muševič, I., Škarabot, M., Tkalec, U., Ravnik, M. & Žumer, S. Two-Dimensional Nematic Colloidal Crystals Self-Assembled by Topological Defects. *Science* **313,** 954–958 (2006).

265. Etxebarria, J. & Ros, M. B. Bent-core liquid crystals in the route to functional materials. *J. Mater. Chem.* **18,** 2919–2926 (2008).

266. Pintre, I. C. *et al.* Bent-core liquid crystals in a route to efficient organic nonlinear optical materials. *J. Mater. Chem.* **20,** 2965–2971 (2010).

267. Zhang, B., Lee, F. K., Tsui, O. K. C. & Sheng, P. Liquid Crystal Orientation Transition on Microtextured Substrates. *Phys. Rev. Lett.* **91,** 215501 (21 2003).

# *Acknowledgements*

The work presented in this Thesis would not have been possible without the help of many colleagues and friends.

First, I would like to show my gratitude to my advisor Prof. Holger Stark for his constant and meticulous support. Under his intellectual guidance, I have learned that proper scientific work must be rigorously formulated and clearly explained. His meaningful questions and suggestions have been essential in making this work more solid and relevant.

I am also grateful to Dr. Patrick Charbonneau for the many discussions we had, the important suggestions he gave me, and also for hosting me in his laboratory in Duke University for several months.

I sincerely thank my colleagues from the research group "Statistische Physik weicher Materie und biologischer Systeme" in TU Berlin. In particular, I am grateful to Oliver Pohl, Dr. Tapan Chandra Adhyapak, Dr. Andreas Zöttl and Maria Zeitz for the stimulating conversations and for the nice time we spent together in our offices.

My thanks also go to the international research training group IRTG 1524, who supported this work, with special regard to Prof. Martin Schoen, Dr. Daniela Fliegner, Petra Erdmann, and Beatrix Thiele.

Last but not the least, I would like to thank my family and friends, who gave me unlimited support during the last years.